Title
Structure, Properties and Reactions of Solid-Liquid Interfaces

Author
Zhao, Xiao

Publication Date
2022

Structure, Properties and Reactions of Solid-Liquid Interfaces

By

Xiao Zhao

A dissertation submitted in partial satisfaction of the
requirements for the degree of
Doctor of Philosophy
In
Engineering – Materials Science and Engineering
in the
Graduate Division
of the
University of California, Berkeley

Committee in charge:
Professor Miquel B. Salmeron, Co-Chair
Professor Jie Yao, Co-Chair
Professor Peidong Yang
Professor Alexander Zettl

Fall 2022

Structure, Properties and Reactions of Solid-Liquid Interfaces

Abstract

Structure, Properties and Reactions of Solid-Liquid Interfaces

by

Xiao Zhao

Doctor of Philosophy in Engineering

University of California, Berkeley

Professor Miquel B. Salmeron, Co-Chair

Professor Jie Yao, Co-Chair

“God made the bulk; surfaces were invented by the devil.” - Wolfgang Pauli.

Solid−liquid interfaces are ubiquitous and involved in numerous natural processes and practical applications, such as corrosion, mineralization, self-assembly, electrochemical energy conversion and storage, etc. Determining the composition, structure, and chemical state of interfaces, in particular the structure of liquids/soft materials near solids, is crucial to obtain a molecular/atomic understanding of the interfacial processes needed to further improve their applications. Currently, this is hampered by the shortage of appropriate characterization tools. In this dissertation a new methodology will be introduced, which is based on the combination of many surface-sensitive techniques and liquid cells capped with ultra-thin membranes. Using this platform, the structure, and properties of the electrical double layers, as well as the nanoscale structure of soft materials at interfaces have been explored. The nanoscale chemical information at solid-liquid interfaces reveals unprecedent details and offers new knowledge of many interfacial properties and processes. This platform opens the way for spectroscopic study of solid-liquid interfaces with less radiation damage with applications in biology, plastic processing, and inorganic materials for electrocatalysis, batteries, etc.

To my parents

Table of Contents

List of figures and tables

List of abbreviations used in the dissertation

AFM: Atomic Force Microscopy

EDL: Electrical Double Layer

KPFM: Kelvin Probe Force Microscopy

IHP: Inner Helmholtz Plane

Nano-FTIR: Infrared Nanospectroscopy

OHP: Outer Helmholtz Plane

SEIRA: Surface Enhanced Infrared Absorption

SERS: Surface Enhanced Raman Spectroscopy

SFG: Sum Frequency Generation

SHG: Second Harmonic Generation

SNOM/NSOM: Scanning Near field Optical Microscopy

SP: Surface Portion

TERS: Tip-Enhanced Raman Spectroscopy

XANES: X-ray Absorption Spectroscopy

XPS: X-ray Photoelectron Spectroscopy

Acknowledgements

Firstly, I would like to acknowledge my Ph.D. advisor, Prof. Miquel B. Salmeron. He is not only a good instructor, but also a good friend of mine. He is very knowledgeable and experienced. His help has been instrumental and helped me to develop a critical thinking for academic research. He encouraged and supported me to explore many crazy ideas even some of them still sound unlikely to be successful (yet some of them worked and got published). When I got excited and overconfident, he pointed out the weakness and the necessary additional experiments from the reviewer's view, and when I was down, he always encouraged me and helped me to figure out the reasons. Without his help I don't even know if I would want to pursue academic research in the future.

I would thank many members in the group, Chenghao (Will) Wu, Yi-Hsien Lu, Matthijs van Spronsen, Shanshan Yang, Heath Kersell, Hao Chen, Lorenz Falling, Ka Chon Ng and Antoine Laine. Being the only graduate student in Salmeron group means that I was mentored by all postdocs in the group (although I didn't have mentees). Thanks for teaching and training me so much and I hope everything goes well in your future endeavors.

I would also thank all the friends/collaborators around me. The collaboration between us was always pleasant and the trips to many national and state parks we took in the past refreshed my mind. Many research ideas were brought up during driving, hiking and kayaking.

I was supported by NSF-BSF grant number 1906014.

I also thank the generous help, which including beamtime allocation, instruction, and suggestions from:

Beamline scientists in ALS: Dr. Hans Bechtel, Dr. Michael C. Martin, Dr. Stephanie Corder, Dr. Jinghua Guo, Dr. Oleg Kostko, Dr. Slavomir Nemsak, Dr. Ethan Crumlin, Dr. Cheng Wang, Dr. David Shapiro.

Beamline scientists in NSLS-II: Dr. Iradwikanari (Ira) Waluyo

Staff scientists in the Molecular Foundry: Dr. Paul Ashby, Dr. Virginia Altoe, Dr. Behzad Rad, D. Frank Ogletree, Dr. Ed Barnard, Dr. Adam Schwartzberg, Dr. David Prendergast, Mr. Ed Wong

There are also so many staff and users that helped me in the past, I would like to apologize to you if I forgot to mention here. Somme times even a short chat during experiment or in the hallway inspired me a lot, even if never asked for their name. I would like to thank Dr. Paul Ashby and Dr. Hans Bechtel especially, they not only taught me a lot on the instrumentation but also offered me important guidance on research and future career.

Last and most importantly I would like to thank my family, who supported me from the first moment I came into the world. My mother and dad are the best parents that I can think of. They had tried very hardly to train me on (Chinese) literature but even more clearly, I demonstrated I am not the right person on literature. They left a huge collection of books in the living room when I was a child, which helped me to make up my mind to study science, at least engineering,

not literature. I would like to thank the most important one of me, although I don't have any information about you, but thanks for being so late that I have enough time (especially weekends) to stay in the lab and do experiments during the Ph.D. time.

Research work on solid-liquid interfaces (Chapter 3) was supported by the Office of Basic Energy Sciences (BES), Division of Materials Sciences and Engineering, of the U.S. Department of Energy (DOE) under Contract DE-AC02-05CH11231, through the Structure and Dynamics of Materials Interfaces program (FWP KC31SM).

Research work on photoresists (Chapter4, case I) was funded by Lam Research Corporation.

Research work on protein assembly (Chapter4, case II) was funded by the U.S. Department of Energy, Office of Science, Office of Basic Energy Sciences, Materials Sciences and Engineering Division under Contract No. DE-AC02-05-CH11231 program Unlocking Chemical Circularity in Recycling by Controlling Polymer Reactivity Across Scales CUP-LBL-Helms.

Research works on catalysts (Chapter4, case III) was supported by the Office of Basic Energy Sciences (BES), Chemical Sciences, Geosciences, and Biosciences Division, of the U.S. Department of Energy (DOE) under Contract DE-AC02-05CH11231, FWP CH030201 (Catalysis Research Program).

AFM, KPFM, Raman, SEM, TEM, ATR-FTIR, Cyclic Voltammetry and lab-based XPS were conducted at the Molecular Foundry, a DOE user facility supported by the same contract.

Nano-FTIR was conducted at beamline 2.4 and 5.4 at the Advance Light Source (ALS); Liquid/gas cell XPS was conducted at beamline 11.0.2 at ALS; Near Ambient Pressure XPS (NAP-XPS) was conducted at beamline 11.0.2 and 9.3.2 at ALS, and beamline 23.0.2 at National Synchrotron Light Source II (NSLS-II). Liquid/gas cell XANES was conducted at beamline 8.0.1.4 at ALS and beamline 23.0.2 at National Synchrotron Light Source II (NSLS-II); ex-situ XANES was conducted at beamline 8.0.1.4 and 7.3.1 at ALS; Liquid cell RsoXS was conducted at beamline 11.0.1 at ALS. ALS is also a DOE user facility supported by the same contract.

ALD, E-beam evaporation and Rapid thermal annealing were conducted in the Marvell nanolab in the University of California, Berkeley.

Chapter 1 Solid-liquid interfaces, where magic happens

Abstract

The structure/properties of solid-liquid interfaces are introduced in this chapter. Research on solid-liquid interfaces has attracted increasing interest due to their abundance and complexity, and the ability to characterize them at the atomic/molecular scale is essential in many fields, both academic and industrial. This includes phenomena such as wetting, corrosion, electrochemical energy conversion/storage and bioengineering. The basic organization of the thesis will be shown at the end of this chapter.

1.1. Where are the solid-liquid interfaces

Solid-liquid interfaces are abundant in both natural processes and industrial applications. Structure and properties of solid-liquid interfaces govern chemical and physical processes in numerous fields, including geology, biology, and material science, and increasingly attract researches in these academic disciplines (1-3).

The interfaces between minerals and aqueous solutions (or droplets/moisture atmospheric gases) play an essential role on Earth's surface, as Earth is called "the blue planet" from a global view. At the microscopic level, sediments form by condensation and nucleation of certain ions, such as calcium, magnesium, and carbonate from the aqueous solutions, which react and evolve over time, as shown in Fig 1.1. The corrosion and degradation of many man-made buildings and vessels causes big financial losses every year. The mineral-solution interfaces also affect the uptake, release, transport, and transformation of many environmental-concerning molecules/ions, such as CO_2 in the atmosphere and heavy metal cations in pollutants. Subtle changes of ocean acidity caused by excess CO_2 dissolution induce a tremendous alternation of the microenvironment of mineral-ocean interfaces and threaten the survival of many marine species (4-7).

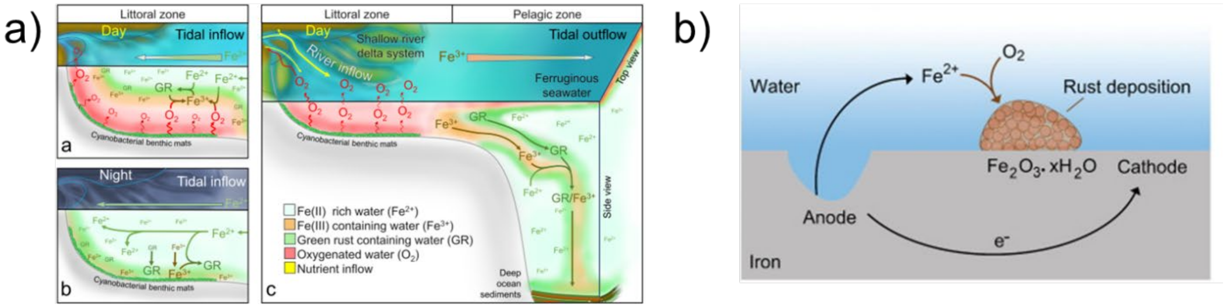

Figure 1.1 Illustration of the solid-liquid interfaces during mineralization process (a) and corrosion process (b). Reprinted with permission from ref (8, 9). Left: Copyright 2020, with permission from Creative Commons. Licensed under CC BY 4.0. Right: Copyright 2022, with permission from Creative Commons. Licensed under CC-BY-NC-ND.

In living organisms, the interfaces between biologic fluids, such as cytoplasm, and lipid membranes, also play a critical role in various biological processes and applications. Most proteins, including enzymes, and membrane proteins, execute their biological functions while supported or intercalated in lipid phosphate membranes. The cell membrane contains enzymes and proteins, such as Bacteriorhodopsin (bR), that transport protons, K^+ and Na^+ across the membrane of cell or organelle, maintaining a kinetic barrier for their diffusion, which is vital for cellular bioenergetics. For biomedicine, the adsorption of protein molecules is the first step of biologic response to their contact with artificial materials, and various protein binding/self-assembly behavior to solid surfaces has been widely utilized for bioengineering applications, such as biosensors and energy conversion(10-13).

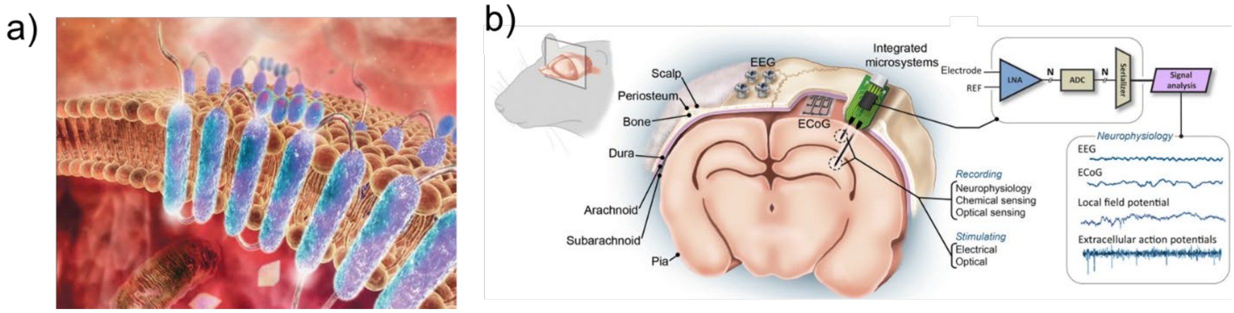

Figure 1.2 Illustration of the lipid double layer and the incorporated G protein (a) and sensors in bioengineering (b). Reprinted with permission from ref (14, 15). Left: Copyright 2020, Elsevier. right: Copyright 2020, with permission from Creative Commons. Licensed under CC BY 4.0.

In industrial applications, numerous materials operate in liquid or moist conditions. Electrochemical catalyst converts reactants at interfaces, such as water or carbon dioxide, into value-added chemicals under reaction voltage. For instance, carbon dioxide molecules adsorbed on the electrode are activated and reduced by the excess electrons on the electrode surfaces, and on the surface of TiO_2, water is split into hydrogen and oxygen under irradiation of light, with a catalytic performance that depends strongly on the surface species. Driven by chemical and electrical potential difference, ions in electrolyte are partially or totally de-solvated, travel across the interfaces and intercalate into electrodes, or the vice versa, to store and convert energy (16). The interfaces between electrodes and electrolytes, called SEI (Solid-Electrolyte Interfaces), passivates the electrode from corrosion while allowing transfer of ions and electrons through them (17). Engineering surface hydrophobicity or hydrophilicity of materials has also been proven to be effective for developing self-cleaning materials and lubrication (18).

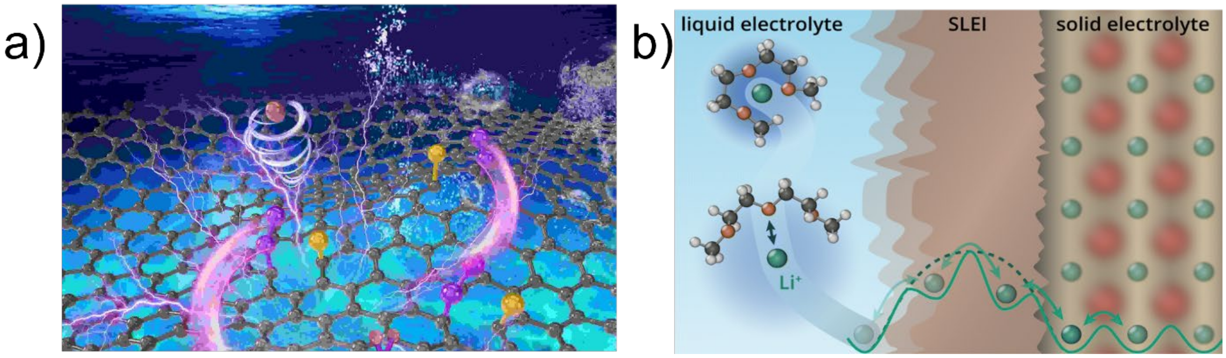

Figure 1.3 Illustration of electrode-electrolyte interfaces in electrochemical catalysis (a) and ion storage (b). Reprinted with permission from ref (19, 20), left: Copyright 2020, John Wiley and Sons, right: Copyright 2020, with permission from Creative Commons. Licensed under CC BY.

Basic properties of solid-liquid interfaces, including the concentration profile, potential profile, and molecular structure of both water and ions, are then critical to elucidate these chemical and physical processes as well as material engineering.

1.2. Basic properties of solid-liquid interfaces

Most solids in contact with aqueous solution interfaces are charged. The charges come from specific adsorption of ions in the aqueous solution (e.g., H^+ and OH^-), leakage of lattice ions into the aqueous solution and bias induced electron transfer between external devices and electrodes, as well as electrodes and electrolytes.

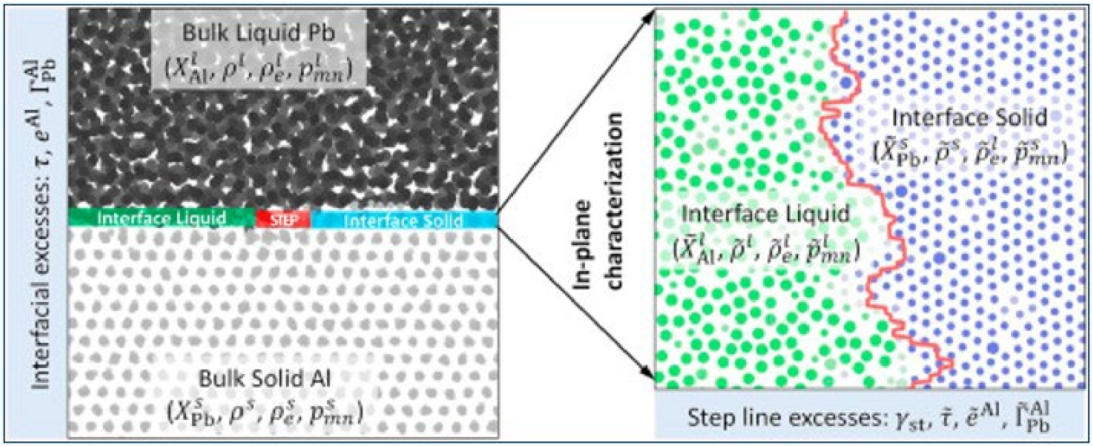

Figure 1.4 Illustration of the solid-liquid interfaces structure. Reprinted with permission from ref (21). Copyright 2020, Elsevier.

The presence of water drastically alters the surface properties of solids, by changing the surface morphology, composition, and electronic structure. In some cases, the presence of water, ions and electrical potential will preferentially stabilize certain facets of the solid and cause surface reconstruction of the solids. Undercoordinated atoms on surfaces can become highly mobile and segregate to form particles under certain conditions, thus inducing morphological evolution. The interplay between the surface energies and chemical potential also induces composition changes on solid surfaces, and preferential enrichment of some certain elements of species on surfaces is often the balance of bulk composition, surface bonding as well as external conditions including electrical field, temperature, and pH. These external conditions also induce changes of electronic structure, and dynamical evolution of surface oxidation states is a key point to decipher chemical reactions at the interfaces (16).

Meanwhile, the interfacial water also shows distinct structure and properties compared to the bulk water molecules. This liquid layer near the electrode is usually referred to as double layer or electrical double layer (22). The solvation state of ions, water orientation and hydrogen network at the interface can be completely different than that in the bulk. One typical example is the formation of an ice-like ordered bilayer water on anatase in contact with liquid water at room temperature, which indicates the strong interaction between them (23-27). On the contrary, it was proposed that no hydrogen bonds form on the surface of magnesium oxide surface, despite of the MgO hydrophilicity (28).

Extensive research efforts have been spent to explore the surface properties of solid in contact with liquid, including the surface morphology, composition evolution and electronic structure, using many spectroscopic and microscopic techniques, with less attention to the structure of liquid layer near the interfaces. First, the structure and properties of the liquid itself is still poorly understood compared to the bulk solid; Second, most of liquids have high vapor pressure at room temperature, which limits the application of many surface-sensitive techniques that requires ultra-high vacuum environment; Third, the presence of liquid phases amplifies radiation-induced side reactions, such as X-ray beam-induced hydrolysis, which also affect the experimental investigations of liquids. The flexible and mobile nature of liquids makes microscopic study extremely challenging, and only few researches have been done for some extreme cases, such as aluminum ions adsorbed on mica surface (29). Most core-level spectra, such as X-ray Photoelectron Spectroscopy, focuses on the composition and oxidation state of species are less sensitive to molecular vibrations.

Nevertheless, liquid layers at the interface play a critical role in many interfacial reactions. For example, the reaction rate and multi-carbon product selectivity in CO_2 electroreduction shows a strong dependence on the presence of alkali cations, which were proposed to affect the EDL field strength and the electron transfer step (30-32). Similarly, anions affect the electrochemical microenvironment and the reactivity of water splitting reaction, including hydrogen evolution and oxygen evolution reaction (33-36).

Fundamental investigation of the liquid layer structure near solids has become increasingly popular, both in simulation and in experiments. In theory, the mean-field theory approach takes both the electrostatic attraction of charged interfaces and the counter ions as well as the diffusion of ions inside the liquid into consideration, and the resulting distribution along the surface normal is highly inhomogeneous. The details and historical development will be discussed in chapter3.

Meanwhile, experimental efforts at the solid-liquid interfaces lagged for a long time. This is mostly due to the lack of appropriate spectroscopic tools that could operate in liquid environments. So far most of studies used spectroscopies, like IR or Raman to probe the molecular species in the bulk, but the application of IR for the surface, or core-level spectroscopies for liquid, have only been developed or improved very recently. The details of these techniques will be discussed in chapter2.

1.3.Organization of thesis

The cases of solid-liquid interfaces are so abundant that only a few of them will be chosen to study in this thesis. Because of the complexity of solid-liquid interfaces, a reductionist approach is adopted here, with some simple model systems, such as the interfaces between graphene and aqueous solution to start, and then increasing the complexity, for example, protein assembly, in the quest to better understand the basic chemical properties and processes happening at solid-liquid interfaces.

In chapter 1 the abundance and basic properties of solid-liquid interfaces has already been discussed. Chapter 2 starts with a brief overview of surface-sensitive spectroscopic techniques. Two approaches-namely probing through the liquid and probing through the solid, which enable the measurements for liquid phase, will be compared. The fabrication procedure of ultra-thin free-standing membranes used for the second approach will be presented afterward.

Chapter 3 focuses on the structure of the electrical double layer, with a brief review of historical development of the electrical double layer model at the beginning, followed by the investigation of the graphene-sulfate interfaces. Next, we move to the anatase-water interfaces. Chapter 3 ends with a short summary of the importance of combining different characterization techniques together for a comprehensive understanding of the electrical double layer.

Chapter 4 focuses on the extended capability of a specific spectroscopic imaging technique, nano-FTIR, for soft material at interfaces. It starts with a simple case: the interfaces between exposed and unexposed area of a photoresist film. The assembly of S-layer protein will be shown in the following sections, in which the assembly dynamics, spatial profile and structural response to external conditions will be explored. After the discussion of protein assembly, the nanoscale properties of nanoparticles under electrochemical conditions will also be discussed. Chapter 4 ends with a short prospective on the opportunities enabled by this platform.

The dissertation finishes with conclusions and perspectives from the last chapter.

Chapter 2 Brief review of surface-sensitive spectroscopic techniques

Abstract

In this chapter the basic spectroscopic characterization method for solid-liquid interfaces will be briefly summarized. For core level spectroscopy, surface sensitivity is generally achieved thanks to the strong attenuation of photoelectron or secondary electrons (e.g.: XPS, EY-XANES). For vibration mode characterization surface sensitivity can be achieved by the near-field plasmonic enhancement (SERS, SNOM), or by selection rules based on symmetry and photon polarization (SFG, SHG). There are also some other techniques used to track interfacial processes (e.g., THz), but the signal to background ratio typically limits its general application. The achievement of surface sensitivity is the focus of this section. Many surfaces sensitive techniques usually operate in UHV or inert gas environment because the probe particles, electrons or X-rays are attenuated by the environment material. Two approaches have been developed that limit the path length traveled by the probe particles. In one probe goes through liquid, and in another if goes through a solid barrier. The fabrication of liquid cells capped with ultra-thin membranes will be shown at the end of this chapter together with a description of all the techniques used in this thesis.

2.1.How to achieve surface sensitivity

In most realistic conditions, most of atoms in both solid and liquid are in the bulk and only a very small portion of them are at or near the interfaces, however these "interfacial atoms" determine critical properties of materials and affect many practical processes and reactions, including electrocatalysis and energy storage.

Firstly, let's consider a piece of 1×1×0.1cm platinum electrode only, if the top two layers are "defined" as the surface of solid, the "surface portion" (SP) of platinum is

$$SP_{Pt} = \frac{2 \times 0.3nm}{0.1cm} \rightarrow 0$$

This means that for this platinum electrode only a negligible portion of atoms are exposed and be affected by the liquid, if no reaction propagates into the bulk electrode. This platinum skin is responsible for many electrochemical processes and reactions.

When there is a liquid layer/phase in contact with the platinum electrode, the water and ions at the electrical double layer have distinct properties compared to the bulk properties. The thickness of the electrical double layer (Debye length) is predicted by the Stern model:

$$\kappa^{-1} = \sqrt{\left(\frac{\varepsilon_0 \varepsilon_r k_B T}{\sum_{j=1}^{N} n_j^0 q_j^2}\right)}$$

Where the $\varepsilon_0,\ \varepsilon_r,\ k_B,\ T$ are the vacuum permittivity, relative permittivity of the liquid (or relative permittivity of interfacial liquid), Boltzmann constant and temperature, respectively. n_j^0 is the bulk concentration of each ion and q_j is the charge each ion carries in the liquid. Although this expression has been challenged recently for highly concentrated electrolytes, it is still a good approximation for dilute solutions. For a typical biological fluid or electrolyte, the Debye length is in the order of 1nm. The portion of liquid molecules in the electrical double layer depends strongly on the liquid thickness. For a typical electrochemical experiment:

$$SP_{EDL}(EC) = \frac{0.6nm}{10cm} \rightarrow 0$$

The different structure or properties of this "electrolyte skin" is typical of our interest. In many *in-situ* or *operando* studies, a thin water film is used to mimic bulk electrolyte; for a typical liquid cell used for transmission study:

$$SP_{EDL}(liquid\ cell) = \frac{0.6nm}{200nm} \sim 10^{-3}$$

For a typical liquid film used in XPS:

$$SP_{EDL}(liquid\ film) = \frac{0.6nm}{20nm} \sim 10^{-2}$$

As the thickness of the liquid decreases, a larger portion of its molecules are in the electrical double layer, but the limited mass transfer in the confined space starts to play a role. The balance of surface proportion and mass transfer could possibly be overcome by using a closed liquid cell, which will be discussed in the following sections.

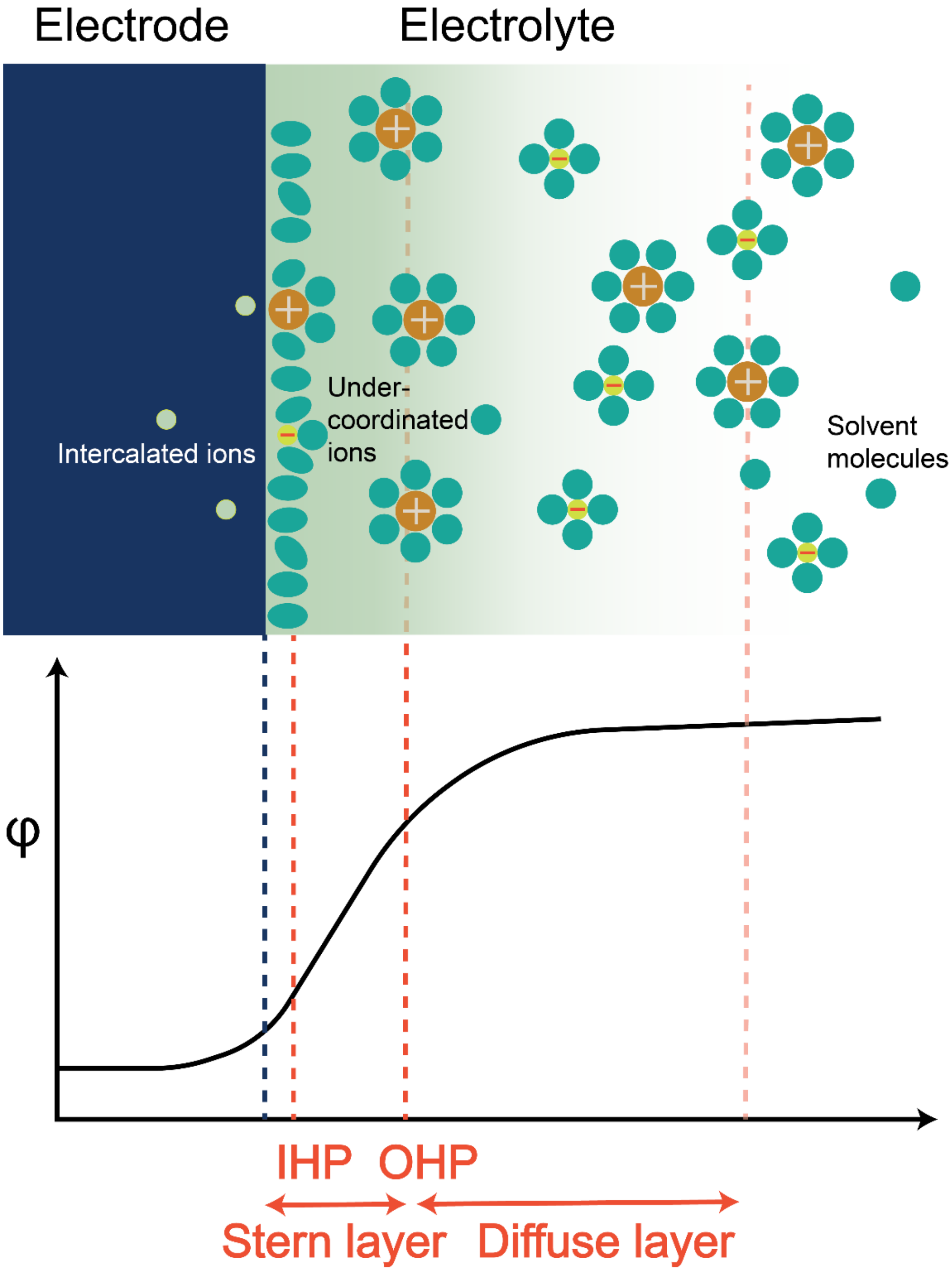

Figure 2.1 Illustration of the solid-liquid interfaces

2.1.1. Attenuation

The effective travel distance of low kinetic energy electrons (photoelectrons or secondary electrons, 10^0-10^2 eV) in condensed material is roughly a few nm, while the travel distance of electrons with high kinetic electrons (>200nm for 10^5 eV electrons used in TEM), and photons (>100nm for X-ray photons and >1µm for low energy photons, such as visible or IR) are much longer. Most surface-sensitive X-ray spectroscopies take advantage of the strong interactions between the low energy electrons with materials, with XPS and EY-XANES being the most popular techniques.

X-ray Photon Electron Spectroscopy (XPS, or PES) is one of the standard methods for interfacial studies over the recent decades (37). It records the ejected photoelectrons originated from the excitation of core-level electrons by the incoming X-rays as the function of their kinetic energy. Atoms in different chemical environments have slightly different core levels, and this could be reflected in different binding/kinetic energy of the photoelectrons. Only the photoelectrons generated near surface experience little scattering by the surrounding atoms and escape from the sample, while photoelectrons originated deep in the bulk will be thermalized and few electrons could be detected. Therefore, XPS is surface sensitive and chemical sensitive, and relatively less destructive than the ion-based techniques (38-40).

The strong interactions between the photoelectrons and the materials also enable depth profile for the solid-vapor or solid-liquid interfaces through variation of kinetic energy or collection angle. For a homogeneous sample, species at depth z will contribute the intensity:

$$I = I_0 e^{-\frac{z}{\lambda cos\theta}}$$

I_0 is the initial intensity without any attenuation, λ is the electron elastic mean free path, and θ is the emission angle respect to the surface normal. At normal collection, the top surface (e.g., 0.3nm) has the contribution:

$$\frac{I_{top}}{I_{total}} = \frac{I_0 \times 0.3nm}{\int_0^{\infty} I_0 e^{-\frac{z}{\lambda}} dz} \sim \frac{0.3nm}{\lambda}$$

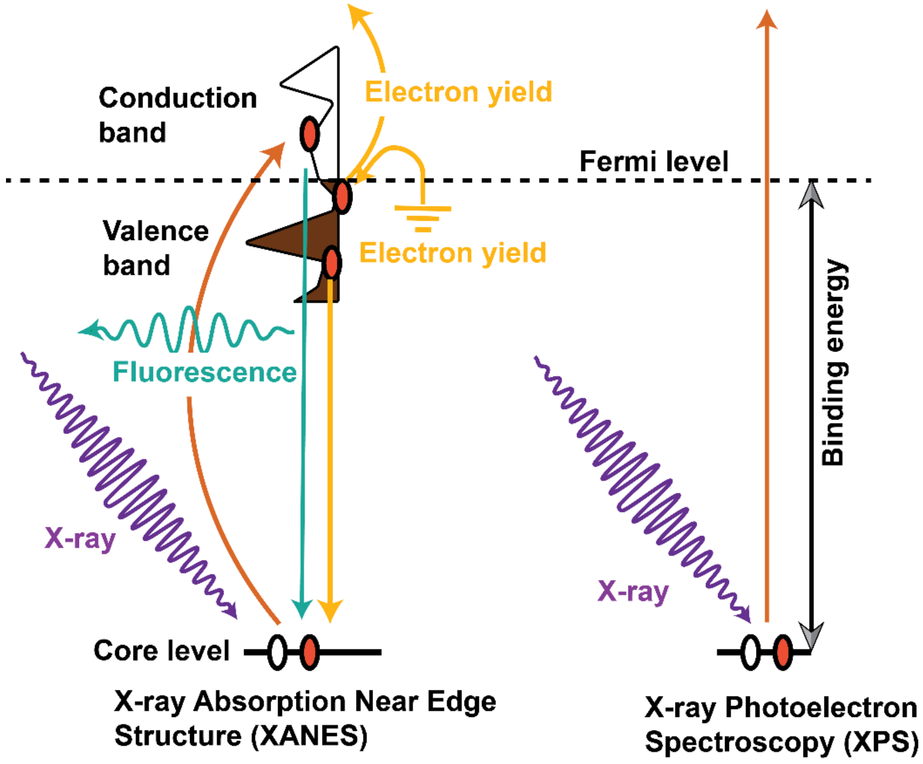

Figure 2.2 Illustration of XPS and XANES (EY and FY mode) process

Typically for photoelectrons with 200eV kinetic energy, the elastic mean free path is usually around 0.6nm and the contribution of the top surface is 50%, while for photoelectrons with 1200eV kinetic energy the mean free path is around 4nm, and the contribution of the top surface is less than 10%. However, in most cases the sample is never homogeneous, the distribution of chemical species in depth requires integrating the concentration at depth z times the exponential function shown above. If the concentration profile is not known one needs to perform the XPS measurement as a function of the X-ray photon energy. This is called "depth profiling".

Application of soft XPS/tender XPS to solid liquid interfaces is critical but also extremely challenging. For tender X-rays the photoelectron usually has high enough kinetic energy (>3000 eV) to travel more than 10nm in the solid of liquid phase, but the contribution from the surface is less than 10%, making it less surface sensitive (41-47). Further, the thin liquid film also limits the mass transfer between the electrode and the bulk solution. For soft X-ray, the use of cells covered by a very thin membrane window is a good choice (48-56). These membranes should ideally be only a few nanometers thin to let the photoelectron pass through them with minimal absorption. The fabrication of such thin membranes is delicate and is the bottle neck of that approach. The fabrication procedure adopted in my studies will be discussed in the following sections of this chapter.

Another interesting technique is Standing Wave XPS (SWXPS), which demonstrated its power in determining the surface composition on depth direction quantitively with Å precision (37, 56-60). Apart from the normal sensitivity from XPS, it is based on the formation of X-ray standing wave on the surface. The sample is usually kept around a certain angle (under Bragg condition) to the incident X-ray so that the incident and scattered X-ray interference to form a stable standing wave pattern along the sample surface normal. This standing wave gets enhanced when the electron density of the substrate has a similar periodic modulation (single crystal, or on multilayer mirror, e.g., stacking of B_4C and W layers), usually for a few nanometers. As the sample rocks a few degrees, the peak of interest would show different modulation based on their distribution (57). SWXPS has been used to reveal many critical interfacial compositions and structure, but its general application on solid-liquid interfaces has so far been limited to thin liquid layer (1-2nm) supported on solid. With SWXPS the position of hydrated cesium and sodium ions at hematite-water vapor interfaces, and corrosion of Ni by KOH solution has been obtained (56, 59).

X-ray absorption spectroscopy (XAS, or usually X-ray absorption near edge spectroscopy XANES) probes the conduction band structure of solid made of unoccupied orbitals of the material atoms or molecules. It can be measured directly by the attenuation of the primary photons during transmission, or indirectly, by measuring decay products such as fluorescent photons or electrons, which are produced by the decay of excited core-hole states of the atoms absorbing the X-ray photons (61-63). XAS is bulk sensitive when measured in transmission or via fluorescence. Conversely, in the electron yield mode, XAS can be highly interface sensitive.

For the solid-vacuum interfaces, only electrons excited near the surface contribute to the measured signal. Soft X-ray absorption leads to the emission of Auger electrons with kinetic energies of hundreds of eV, which generate a cascade of secondary electrons as they propagate through the material. Near the interfaces, they can escape into the vacuum while deeper in the sample, electrons and ions recombine before the electrons can reach the surface. The electrons that escape into the vacuum can be measured directly using an electrode in the vacuum side. Another method is to measure the charge-balancing current flowing from ground to the sample to compensate the emission into the vacuum (64). Because electron-yield XAS in vacuum gives information on the (near) surface, electron-yield XAS within a liquid cell is also expected to be sensitive to the solid-liquid interfaces (65-68). Another method of detection was proposed by measuring the so called "ion yield” (69, 70), but this method has been later shown to be the same as the electron yield method. Both methods are sensitive to the interfaces (23).

There is also some research directly measuring fluorescence as the decay product of X-ray adsorption (FY-XANES), but this method is much less surface process on account of the long mean free path of X-rays compared with that of electrons. FY-XANES coupled with standing wave has been explored in the past, and proven to be sensitive to the buried interfaces (71, 72).

It is worth addressing a common misunderstanding of electron attenuation through condensed material. In XPS only the photoelectrons (and the Auger electrons) without energy loss are measured, so the peak intensity is directly related to their attenuation which is determined by their Elastic Mean Free Path (EMFP). For XANES it becomes more complicated. For Auger Yield XANES, Auger electrons with no energy loss are selected from the large background of secondary electrons, so EMFP still applies. For general Electron Yield XANES measured through electron energy analyzer most of high energy electrons without much energy loss are measured so the Inelastic Mean Free Path (IMFP) better describes the attenuation. When the

Electron Yield channel is measured through the drain current in liquid cell/gas cell (once named "ion yield") the thermalization length, instead of the EMFP or IMFP should be used (73-76).

The surface sensitivity of vibrational spectroscopy is also possible, but due to the long wavelength of visible or IR light, most of the signal still comes from the bulk. One example is the most popular IR techniques: Attenuated Total Reflection FTIR (ATR-FTIR) (77-80). In ATR-FTIR, the incident angle of IR beam is kept above the critical angle, so that most of the light is reflected and no electromagnetic field travels beyond the proximity of the interfaces, except the part of the evanescent wave.

$$E(x,y,z,t) = E(0,0,0,t)e^{i(k_x x+k_y y)}e^{-k\sqrt{n_0^2\sin^2\theta-n_s^2}z}$$

Then the characteristic decay length of the evanescent wave is described by the following formular:

$$d_p = \frac{\lambda}{2\pi\sqrt{n_0^2\sin^2\theta - n_s^2}}$$

Where the λ is the wavelength of light, n_0 is the refractive index of the incident material, n_s is the refractive index of the second material, θ is the angle of incident.

d_p is usually on the order of a few microns, so the proportion of the interfaces species is roughly 0.1%, much lower than that of core-level spectroscopy. Recent experimental prove even increase the penetration depth of such evanescent wave to 60microns, an order larger than theory (81).

ATR-FTIR has been widely used to probe chemical processes at electrochemical interfaces (77, 82-85). The reason is that in a heterogeneous catalysis reaction, many molecular species, including adsorbed reactants, products, and intermediates, are mostly present at the interfaces between the catalyst and the liquid. But the ATR-FTIR technique is not intrinsically a surface-sensitive technique since the decay length of the photon field is of the order of the wavelength, i.e., many micrometers for IR photons. In some other cases, a difference spectrum can be obtained by subtracting the spectrum under one condition (e.g., under bias) form that in another condition (e.g., open circuit), the contribution from the interfaces could then be much higher than normal ATR-FTIR, and this will be discussed in the following section.

2.1.2. Selection rules

Surface sensitivity can be achieved by taking advantage of the selection rules of optical techniques. These rules include polarization dependence in IR which can be changed by the angle of incidence (polar and azimuthal) of the photons, in addition to symmetry rules as in Sum Frequency Generation (SFG) and Second Harmonic Generation (SHG) (86-99).

In a typical SFG experimental setup, visible and IR (in case of SFG), and for SHG only one incident beam, are focused on the same area on the sample surface, and the emitted beam with a frequency equal to the sum of the frequencies of the two-incident beam is measured. To obtain a spectrum the frequency of incident IR beam is varied, as shown in figure 2.2. SFG is only sensitive to molecules that lack inversion symmetry, which means that randomly orientated molecules in the bulk do not contribute to the SFG intensity. Only at the interfaces the centrosymmetry is broken and those species contribute to the SFG spectrum. SFG and SHG are then the ideal tool to probe the molecular vibration and orientation at the buried interfaces.

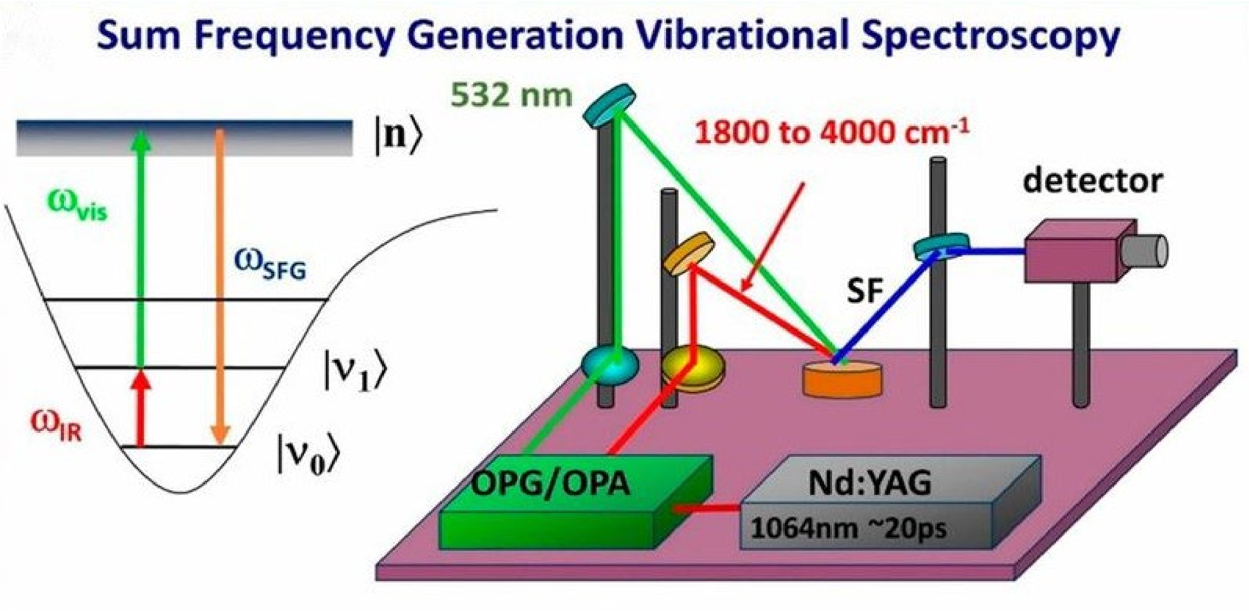

Figure 2.3 Schematic of SFG principle and the experimental setup. Reprinted with permission from ref (100). Copyright 2006 American Vacuum Society.

At neutral interfaces without electric field, the intensity of SHG/SFG signal depends on the second order susceptibly, $\chi^{(2)}$, but the existence of electric field at the interfaces could enhance the signal by introducing another nonzero term: $\chi^{(3)}$, and the total intensity is determined by the sum of both interfacial effect and the electrical field effect. The modulation by the electrical field is also known as electric-field induced sum frequency generation. The relationship between the final signal and these two terms can be described as

$$I \propto |\boldsymbol{P}^{(2)}(\omega_0) + \boldsymbol{P}^{(3)}(\omega_0)| = |\chi^{(2)}\boldsymbol{E}_{vis}\boldsymbol{E}_{IR} + \chi^{(3)}\boldsymbol{E}_{vis}\boldsymbol{E}_{IR}E_0|^2$$

Here the E_{vis}, E_{IR} is the local electric field vector of the incoming visible light and IR light, $\boldsymbol{P}^{(2)}(\omega_0)$ and $\boldsymbol{P}^{(3)}(\omega_0)$ are the nonlinear optical polarization in the second and third order, respectively. $\chi^{(2)}$ comes from the intrinsic nature of the interfaces that orientated molecules, and $\chi^{(3)}$ has contribution from isotropic molecules in the bulk and from the oriented molecules due to the existence of static electric field (101).

Based on the EDL model, the electric field also has an inhomogeneous distribution along surface normal so that the electrical field is no longer a constant E_0, and the third order nonlinear polarization could be expressed as:

$$\boldsymbol{P}^{(3)}(\omega_0) = \int_0^{+\infty} \boldsymbol{P}^{(3)}(z, \omega_0)dz = \int_0^{+\infty} \chi^{(3)}\boldsymbol{E}_{vis}\boldsymbol{E}_{IR}\boldsymbol{E}_{EDL}(z)dz$$

Where the z is the distance from the interfaces. If the molecules are isotropic at interfaces plane,

$$P^{(3)}(\omega_0) = \int_0^{+\infty} \chi^{(3)} E_{vis} E_{IR} E_{EDL}(z) dz = \chi^{(3)} E_{vis} E_{IR} \int_0^{+\infty} E_{EDL}(z) dz = \chi^{(3)} E_{vis} E_{IR} \Phi_0$$

Φ_0 is the surface potential. The above analysis assumes that the phases of incident and reflected beam don't change at different collection depth. Taking the phase change into consideration, the equation can be corrected (91):

$$P^{(3)}(\omega_0) = \int_0^{+\infty} \chi^{(3)} E_{vis} E_{IR} E_{EDL}(z) e^{i\Delta k_z z} dz = \chi^{(3)} E_{vis} E_{IR} (\Phi_0 + i\Delta k_z \int_0^{+\infty} \Phi(\mathrm{z}) e^{i\Delta k_z z} dz)$$

The imaginary part could only be retrieved by phase sensitive SFG and has little contribution to the overall polarization at high concentration. It reveals the interfacial polarity and sign of the surface charges in more details (102).

From the surface potential the surface charge density can also be derived.

$$\Phi_0 = \frac{2k_B T}{e} \sinh^{-1}\left(\frac{\sigma_0}{\sqrt{8000k_{BTN_A c\varepsilon}}}\right)$$

The presence of the electric field makes the third order term nontrivial and results in a larger detection depth in SFG experiments (97, 101, 103-105). The intensity of the second order term and third order term depends on the details of the development and the screening of the electric field by the ions and decreases as the ionic strength is lowered. At moderate or high concentration, the contribution from the second order term is higher than the third order term.

Generally when the ionic strength is higher than 0.1M, the diffusion length is much lower than the coherence length $l_c = \frac{1}{k(\omega_{SFG}) + k(\omega_{vis}) + k(\omega_{IR})} \sim 40nm$, and only a few layer of water molecules contribute to the overall SFG intensity, while the effect of electrostatic field is small. As the ionic strength decreases, the second order term almost remains the same while the third order term increases. As the diffusion length goes beyond l_c, SFG photons are generated from deeper parts below the surface (bulk). However, under such conditions the interference of SFG photons in deeper planes is destructive and its contribution is less prominent. Although the probing depth might be very large, the contribution from the top few layers still dominates (101).

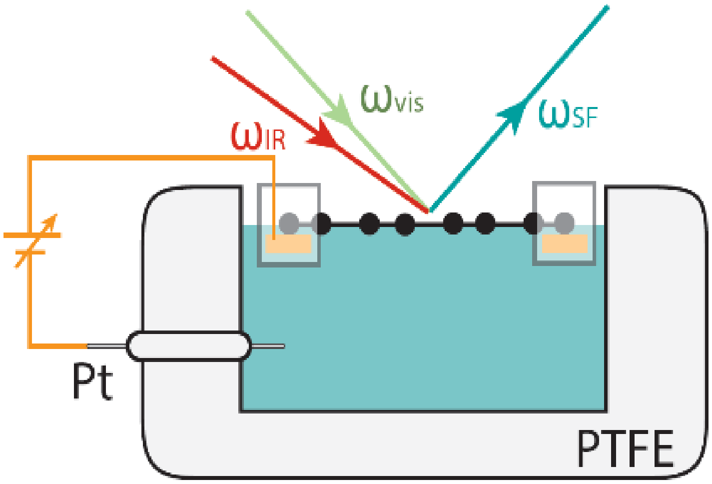

Figure 2.4 A typical electrochemical cell for SFG experiments. Reprinted with permission from ref (86). Copyright 2022, with permission from Creative Commons. Licensed under CC BY 4.0.

In recent years the combination of XANES and Second Harmonic Generation (SHG) enables a new technique: soft X-ray second harmonic generation (106-109). Such combination enables probing unoccupied orbitals (and then the electronic states) with surface confinement by the selection rule. Since the penetration of soft X-ray is still quite large, this tool has a large capability to probe the buried solid-liquid interfaces. Combination of the soft X-ray SHG probe and the optical pump will allow dynamical tracking of chemical reaction on surface in femtosecond domain (108).

In a short summary, SFG/SHG provides reliable way to probe the hydrophobicity/hydrophilicity, orientation of molecular species at the interfaces, the surface potential and the charge density could be derived from the formulars above. The development and application of SFG/SHG provides unique opportunities for a molecular understanding of electrochemical interfaces, biological membranes as well as mineral water interfaces.

2.1.3. Enhancement

In some vibrational spectroscopic techniques, such as Infrared and Raman, the contribution of surface species could be increased by order of magnitude by surface enhancements. This may be accomplished by the use of nanostructures as plasmonic optical antennas, including nanoparticles (SERS, SEIRA) or nanoantenna (SNOM) (110-116).

Early reports on surface enhancement of Raman and IR on metallic surfaces date back to 1970s (117-120). These metallic surfaces enhanced both the local field of incident light as well as the radiation field of Raman-scattered light in SERS, while only the local field in SEIRA. The enhancement of local or radiation field also depends strongly on the surface morphology through surface plasmonic resonance or lighting-rod effect, and for some cases even single molecules adsorbed on the surface could be identified.

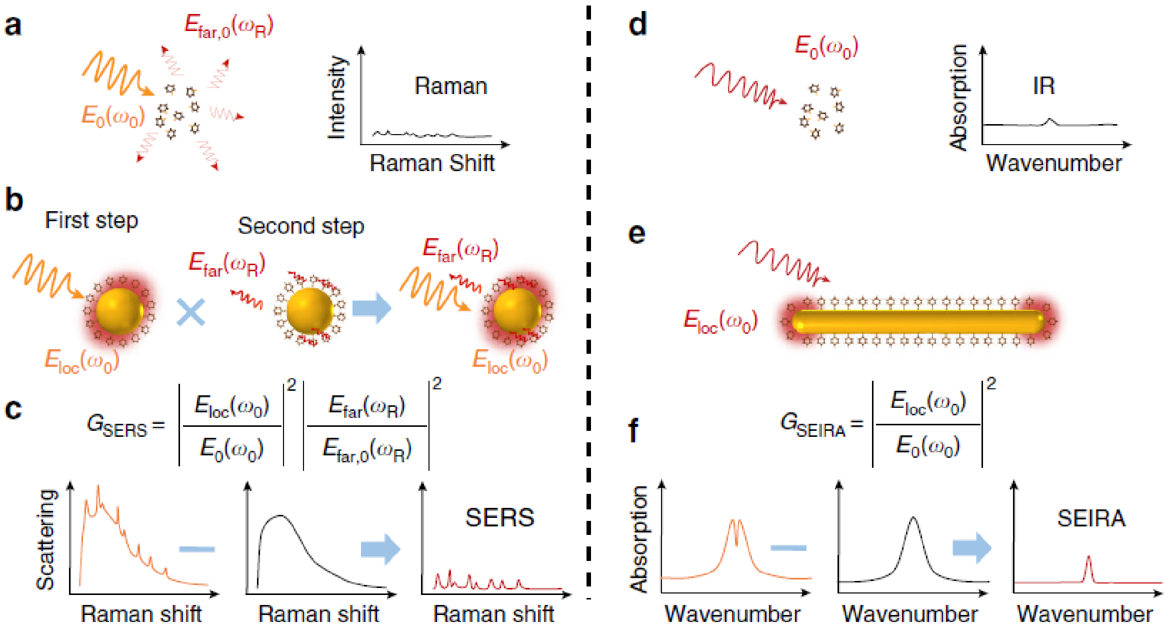

Figure 2.5 Basic principle of SERS (left) and SEIRA (right), reprinted with permission from ref(110). Copyright 2021, with permission from Creative Commons. Licensed under CC BY 4.0.

Microscopically, the incident light excites a collectively oscillation of electrons in the metallic material and induces a resonance electromagnetic field on the metal-dielectric interfaces. The coupling efficiency between the metallic substrate and the dielectric media depends on both the interfacial structure as well as the dielectric properties. In SERS, metallic materials including Au and Ag are usually used as the substrate and in SEIRA semiconductor, such as GaAs, Ge are mostly used (110, 121).

The total Raman intensity of SERS is given by (122, 123)

$$I_{SERS}(\omega_R) \propto |g_1(\omega_o, \boldsymbol{r}_m)|^2 |g_2(\omega_o, \boldsymbol{r}_m)\boldsymbol{\alpha}_m(\omega_R, \omega_o)\boldsymbol{E}_0(\omega_0)|^2$$

The enhancement factor of SERS is given by

$$G_{SERS} = \frac{I_{SERS}(\omega_R)}{I_{NR}(\omega_R)} = |g_1(\omega_o, \boldsymbol{r}_m)|^2 |g_2(\omega_o, \boldsymbol{r}_m)|^2$$

Where $|g_1(\omega_o, \boldsymbol{r}_m)|^2 = |\boldsymbol{E}_{loc}(\omega_o)/\boldsymbol{E}_0(\omega_o)|^2$ is the enhancement of the local field by the incident light and $|g_2(\omega_o, \boldsymbol{r}_m)|^2 = |\boldsymbol{E}_{far}(\omega_o)/\boldsymbol{E}_{far,NR}(\omega_o)|^2$ is the enhancement of the radiation field by the surface plasmon.

For SEIRA, the enhancement only happens for the local field by the incident beam:

$$G_{SEIRA} = \frac{I_{SEIRA}(\omega_k)}{I_{NR}(\omega_k)} = |g_1(\omega_k, \boldsymbol{r}_m)|^2$$

The product of enhancement factor g_1 and g_2 in SERS is typically higher than 10^7, sometimes can be as high as 10^{15}, allowing SERS even on a single molecule level (124, 125). Chemical effect based on the charge transfer between scatterer and metal could also contribute to the signal enhancement.

Raman and IR with surface enhancement has been widely used in both electrochemistry and biochemistry to study the interfacial species, such as reactants, self-assembly monolayer, and solvent (126-130).

Recent advancements in SERS involve the use of well controlled nanoparticle assembly, such as shell-isolated nanoparticles (SHINERS). The oxide coating effectively increases the stability of nanoparticle and isolates the metal core from the liquid (131). The clusters of such nanoparticles could greatly enhance the local field at the particle-particle gap as well as particle-electrode gap, and the species in that region have much larger contribution to the total Raman signal. This method has been proven effective to resolve some key interfacial species for electrochemical process (132, 133).

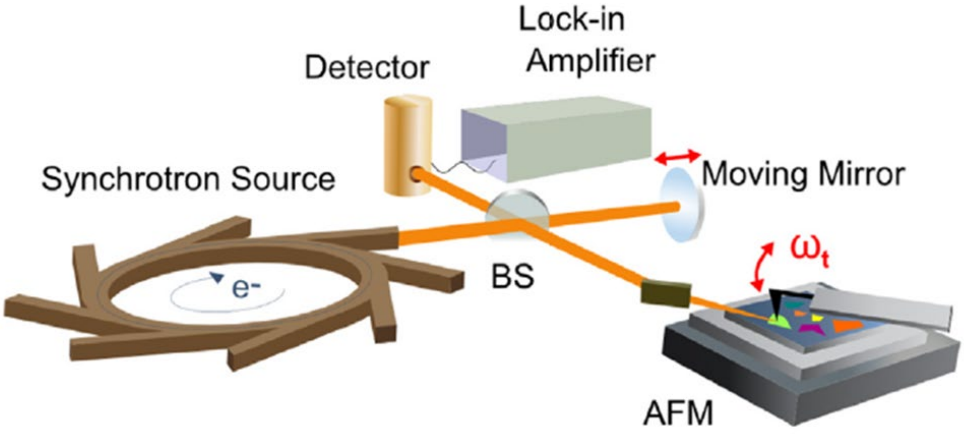

Figure 2.6 Schematic of IR-sSNOM using a synchrotron IR light as source. Reprinted with permission from ref (134). Copyright 2020 Elsevier.

The coupling between incident beams with a nanoantenna, typically a scanning probe, also enhances the local field while circumventing the diffraction limit of the IR or visible beam, thus attracts great interest recently. Aperture-less SNOM and aperture SNOM are the two most popular techniques in this direction. In typical aperture SNOM the spatial resolution is limited to the size of the aperture, which is then limited by the critical cutoff diameter $d_c = \frac{0.6\lambda}{n} > 1\mu m$. In aperture-less SNOM the spatial resolution is close or even lower than the tip radius (20nm) which results in a high surface sensitivity (115, 116, 135).

Two popular setups of the aperture-less SNOM are scattering-SNOM (s-SNOM, e.g., nano-FTIR) and Tip-enhanced microscopy (e.g., TERS). In the former case the nano-optical field around the microscopic tip apex polarizes the sample and the scattered signal is collected. In the latter case the local electrical field gets double enhanced by the tip and the sample and localized at the tip-sample junction (135).

Take nano-FTIR for the example of s-SNOM, AFM tip is brought to the close proximity of the sample surface and a bright coherent (broadband or single wavelength) IR beam is focused on the AFM tip, which is coated with a layer of noble metal like Au, Pt, etc. The incident IR excites the plasmons in the tip coating and get enhanced at the tip apex. In the microscopic volume around the tip apex a strong decaying near field emerges and interacts with the active IR or phonon modes inside the sample. The scattered beam from the tip-sample junction is then collected by the detector. The near field component is further extracted from the far field background by demodulation of the tip vibration, and the relationship between the probing volume and the harmonic is shown in Figure 2.7 (115, 134-139).

As shown in the Figure 2.7, the IR near field is confined to the tip-sample junction, which has the similar dimension to the tip radius, much smaller than the focus beam size. Due to the geometry of the tip, the plasmons along the tip will be excited, which produce a near field with a much larger component along the normal to the surface. The energy resolution of nano-FTIR originates from the interferometer, which allows both the amplitude and phase to be recorded concurrently.

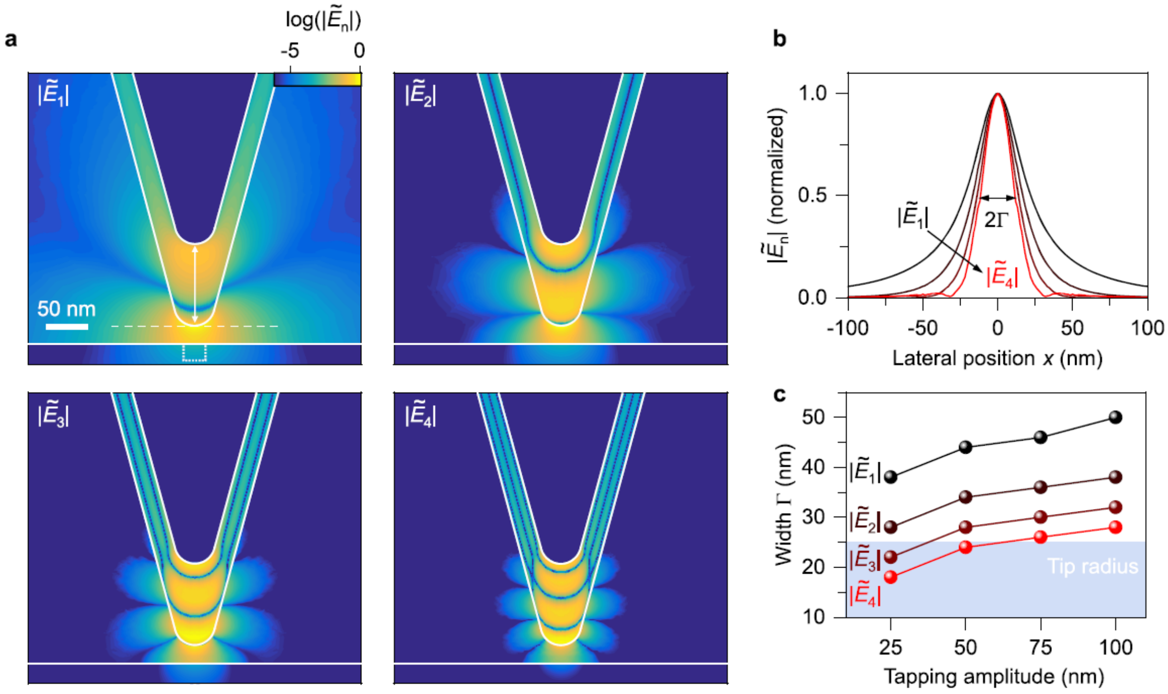

Figure 2.7 Spatial confinement of the IR near field around the tip apex in different modulation orders. The intensity along surface direction has a maximum at the origin (tip apex location), and a width that depends on the harmonic of the oscillation frequency, as shown in (b) and (c). Reprinted with permission from ref (140). Copyright 2021, American Chemical Society.

The scattered field strength from the tip can be written as (115, 135, 141):

$$E_s \propto \left(1+r_p\right)^2 \alpha_{eff} E_{incident}$$

r_p is the Fresnel reflection coefficient of the sample surface, and α_{eff} is the effective polarizability:

$$\alpha_{eff} = \frac{\alpha(a+\beta)}{1 - \frac{\alpha\beta}{16\pi(a+z)^3}}$$

β is the dielectric surface response function that depends on the dielectric function of the tip.

$$\beta = \frac{\varepsilon - 1}{\varepsilon + 1}$$

The probing depth of s-SNOM, or the extent of the near-field along the surface normal, is also closely related to the tip radius. Some other measurement parameters, such as the geometry of the tip, the dielectric function of the sample and the detection harmonic also play a role on the surface sensitivity, as shown in the above formulas and Figure 2.7. For most materials the decay length is usually around 15nm, while there is also some other evidence that the decay length is much higher for soft material, such as ~100nm for polymer (140, 142-144).

Metallic tip and surfaces could double-enhance the local electric field at the tip-sample junction under incident light, and this plays a central role in TERS. The enhancement originates from the combination of lighting-rod effect at tip apex and the localized surface plasmon (LSP) resonance due to the geometric shape of the AFM tip. The incident light (mostly laser) drives the electrons in the valence band to oscillate along the polarization direction, and net charge accumulates at the surface with a density that oscillates with the photon frequency. Like the case of nano-FTIR, as shown in Figure 2.8, the local electric field is greatly enhanced and confined at the tip-sample junction. The enhancement factor $|g_1(\omega_o, \boldsymbol{r}_m)|^2 = |\boldsymbol{E}_{loc}(\omega_o)/\boldsymbol{E}_0(\omega_o)|^2$ is lower than SERS but still quite high.

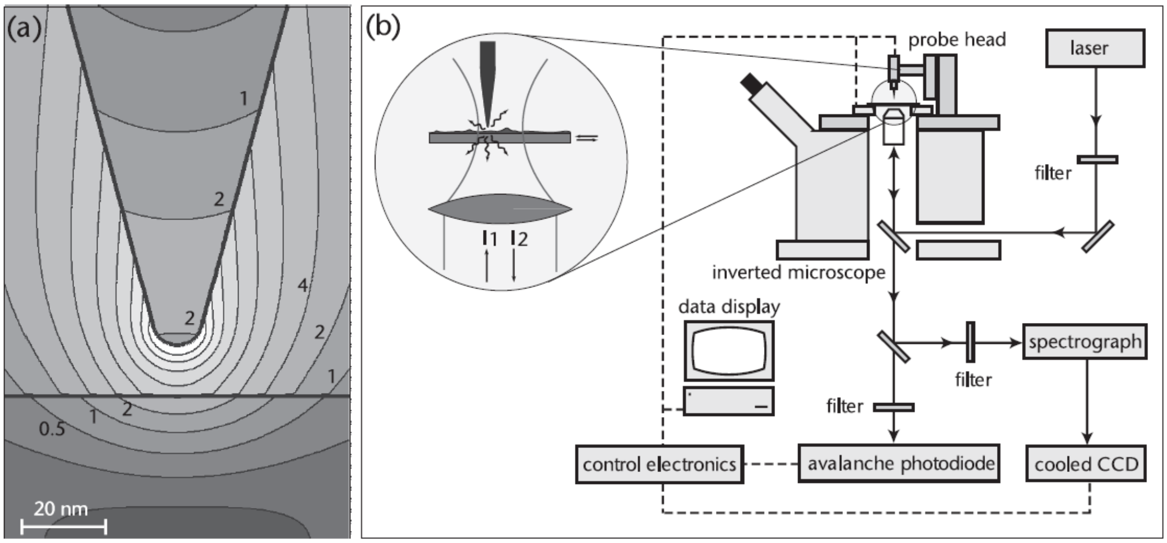

Figure 2.8 Spatial confinement of the electric field around the tip apex (left) and experimental setup (right) in TERS. Reprinted with permission from ref (135). Copyright 2008 Artech House.

In most cases TERS is used to probe the molecular species adsorbed on a metallic or transparent surface (Ag, Au, glass, etc.) and since the noble metal does not contribute to the Raman spectrum shape but enhances only the total signal strength, the chemical information then comes solely from the surface.

In summary, SERS and SEIRA, developed almost half century ago, are very powerful to offer molecular information from interfaces. They are relatively cheap (compared to SFG or APXPS) and do not need access to synchrotron facilities. They can be rather easily built, maintained, and incorporated into or with other techniques, such as DEMS (differential electrochemical mass spectrometry). SERS can easily penetrate liquid phase, and extra caution needs to be taken to lower the optical path in SEIRA. The molecular vibration information revealed by SERS and SEIRA has been the workhorse to interpret reaction processes at interfaces, such as the reaction pathways and electrochemical catalysis reactions (145, 146).

There are also some drawbacks of SERS and SEIRA. As the local field increases many orders of magnitude at the particle-particle and particle-substrate gaps, the energy gets is highly concentrated in space, so that the sample damage can become severe. The substrates used in these techniques have been limited to a few metals, such as Ag and Au so far, which also limit its general applicability (110).

In s-SNOM and TERS the electric field is confined to the tip sample junction and is not subject to the diffraction limit of the incident light. This spatial resolution makes them increasingly popular for nanoscale study of surface properties (142, 143, 147-150). Their operation in fluids, however, is more challenging compared to SERS or SEIRA. Strong damping of vibration motion of the AFM tip probe results in instability of the whole system and, in addition, both tip and sample might be contaminated (151, 152). Besides, the IR is also strongly absorbed by water, and this led to the development of graphene liquid cell, which has been a central part of this thesis. Information about its fabrication and use is covered in the following section in this chapter (152-156).

2.1.4. Other techniques

For many spectroscopic techniques such as THz (also referred as far IR) spectroscopy and ATR-FTIR, the difference spectrum under electrochemical conditions also reveals interfacial properties and reactions, such as the solvation state of ions (157-160).

THz spectroscopy mostly cover the spectral range from 3 cm^{-1} to 300 cm^{-1} (0.1THz-10THz, or 0.4 meV to 40 meV). This energy range corresponds to the rotational and collective movements of molecules; therefore, THz spectroscopy is ultra-sensitive to the dynamics of molecular species in liquid, liquid mixture, or liquid interfaces. For the solid part, THz is sensitive to the carrier density, and has been exploited to study the carrier density, dielectric properties, and the fermi level of electrode (157, 159). By coupling THz pulse with Second Harmonic Generation, the molecular details at the liquid interfaces can possibly be obtained. So far only proof of concept experiments has been performed for bulk samples (161-163).

For liquid phase THz spectroscopy has been used to investigate the rattling modes of ions with strong hydration shell and charge fluctuations of ions with weak hydration shells (164). Recently the hydration of ions and hydrogen bonding at the EDL has also been reported, in which the difference spectrum are obtained by subtraction of THz spectrum at potential V_i to the spectrum at the extreme applied bias V_{max}. The spectral features of species that have no response to the bias, (i.e., species in the bulk) will be subtracted and do not contribute to the difference spectrum. Only species at EDL will respond to the interfacial bias and then becomes nonzero (158).

THz also faces several drawbacks. THz sources are relatively hard to access, and bright, tunable and coherent THz sources often require synchrotron radiation or free electron laser facilities. Most of materials absorb THz radiation strongly, while the fabrication of THz electrochemical cell requires THz transparent window (159). The penetration depth of THz is very high, and the contribution of interfaces region in THz spectroscopy is very small (158):

$$SP_{THz}\sim\frac{3nm}{4\mu m}\times\frac{1}{4}\sim 2\times 10^{-4}$$

The resulting spectrum quality is much worse than the original spectrum.

As discussed above, subtraction of SERS, SEIRA and ATR-FTIR spectrum under different conditions can also reveal molecular information at interfaces. For example, various forms of SEIRA/PM-IRRAS/ATR-FTIR techniques have been used to reveal the key intermediates during CO_2 electrochemical reduction, and SERS is often used to resolve the adsorbates in CO_2 reduction and the surface oxygen dynamics in oxygen evolution reaction. IR and Raman are two of the most popular spectro-electrochemistry (SEC) techniques (82, 165-167).

2.2.Accommodation to liquid environment

Visible and THz beams could easily penetrate liquid phase, while for IR attenuation through aqueous solution is much stronger, in the order of several microns. In most cases attenuation is not the center focus of liquid cell design for these techniques.

THz and FTIR spectroscopy can operate in transmission mode, where the beam directly goes through a thin liquid film (several microns) sandwiched by two optical transparent windows, as shown in Figure 2.9.

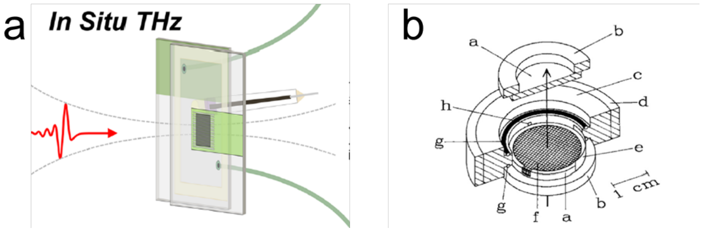

Figure 2.9 Illustration of the transmission approach for the application of surface-sensitive spectroscopy. Reprinted with permission from ref (159, 168). Left: Copyright 2018 American Chemical Society. Right: Copyright 1990 FEBS press.

In most of SERS or SEIRA experiments, the incident light transmits through the thin liquid film, the reflection or scattered signal are collected, as exampled by Figure 2.10 a and b, and in ATR-

FTIR setup the light travel through the inner reflection electrode (IRE) and is bounced by the electrode surface at least one time after which the emitted light is recorded. Liquid cells for these techniques have various designs for incorporating electrodes, mass flow between electrode surface, and channel for the products to escape, which are not the focus of this dissertation. A-c from Figure 2.10 represent the basic design of these liquid cells.

Unlike vibrational spectroscopy, where the photons can travel macroscopic distance in the environmental medium, and only the interfaces contribute to the measurement, most surface-sensitive techniques using near field or X-ray are strongly attenuated in the liquid/solid medium, so they need to be thin enough to let the near field/X-ray photoelectron penetrate. Besides most of these techniques need to be performed in an inert protective environment, such as High Vacuum (XPS, EY-XANES) or inert gas environment (nano-FTIR). Two approaches have been developed to address these challenges, one is to directly expose a thin liquid film over the sample electrode or a droplet array (droplet train) to the excitation source. The other approach is to use an ultra-thin membrane or optical transparent window to enclose the liquid inside a cell.

2.2.1. Through-liquid approach

In the through liquid approach for X-ray spectroscopy, a static or flowing liquid solution is directly exposed to the excitation source, as shown in Figure 2.10. In a UHV system, such liquid film will be in dynamic equilibrium with its vapor in the chamber, so that a differential pumping system is used to maintain the pressure difference between the chamber and the upstream/detector (41-47).

In this approach, a large portion of the signal comes from the liquid vapor interfaces or the bulk liquid, with only a small contribution from the solid-liquid film interfaces. For example, the contribution of water molecules at the interfaces to the total water peak (for a 10nm liquid film) in XPS using 4000eV photons as excitation source is less than 10%. The extraction of interfacial properties, such as potential drop, concentration profile, and chemical state, requires careful analysis and model simulations.

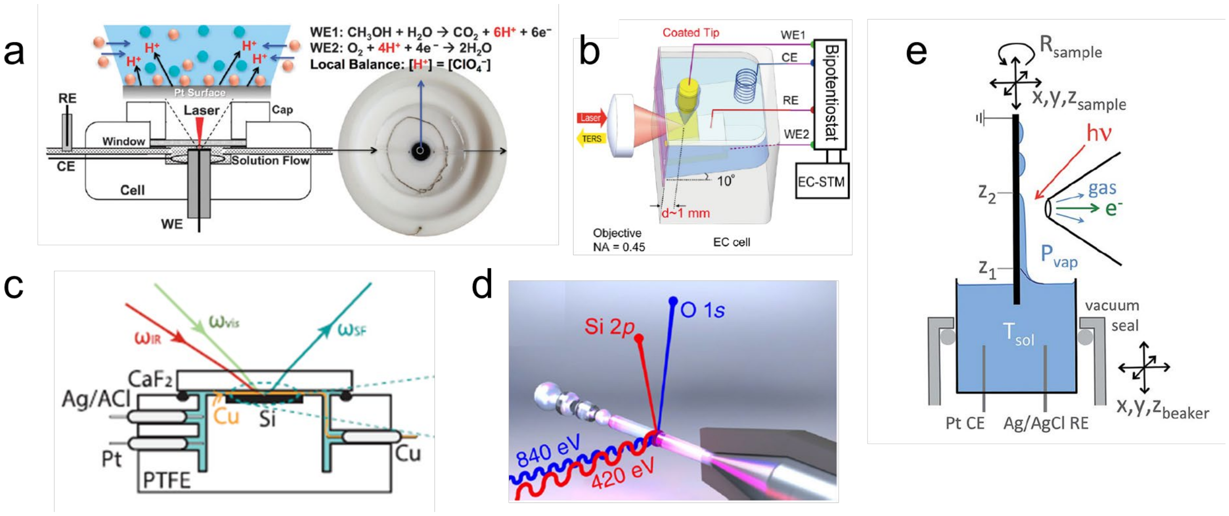

Figure 2.10 Illustration of the through-liquid approach for the application of surface-sensitive spectroscopy. (a) A typical electrochemical cell for Raman experiment. Reprinted with permission from

ref (169). Copyright 2015 Royal Society of Chemistry. (b) Electrochemical cell for TERS. Reprinted with permission from ref (124). Copyright 2015 American Chemical Society. (c) Electrochemical cell for SFG. Reprinted with permission from ref (170). Copyright 2022 American Chemical Society. (d) Liquid jet for XPS. Reprinted with permission from ref (171). Copyright 2016, with permission from Creative Commons. Licensed under CC BY 3.0. (e) Dip-and-pull liquid film experiment for APXPS. Reprinted with permission from ref (56). Copyright 2015 Royal Society of Chemistry.

2.2.2. Through-solid approach

In recent decades, a new approach has been developed to accommodate surface-sensitive spectroscopy to the solid-liquid interfaces, in which an ultra-thin membrane is used to enclose liquid in a cell, as shown in Figure 2.11. The membranes need to be robust to withstand the pressure difference between liquid inside the liquid cell and the outside environment, while also thin enough to be transparent to the photons or electrons.

Early attempts of liquid cell often use a thin X-ray transparent window (<200nm), to enclosed liquid for X-ray absorption/photoemission studies (67, 68, 172, 173). The common materials used are SiNx, SiC and polymers. For XAS studies a conductive layer (Au, or Pt) was evaporated onto the SiNx membrane and served both as the material of under study and as current collector. Both the drain current (from working electrode) or the compensating current (from the counter electrode) can be collected. These were proven to be the same with reversed polarity (23, 66, 68). Both currents are sensitive to the interfacial region extending ca. 1 nm into the liquid.

Thin silicon films have also been used for XPS in the tender energy regime (Figure 2.11 j). The mean free path of photoelectrons with ~6 keV kinetic energy is roughly 10nm, and more than 10% of the photoelectrons penetrate the 15nm window to reach the vacuum side (173).

Inspired by the development of graphene-liquid cell for TEM and XPS study, graphene has become a popular choice for the ultra-thin membrane starting since 2011 (174, 175). Graphene is a 2D material consisting of carbon atoms with delocalized π orbitals, exhibiting excellent mechanical strength and chemical stability over some certain potential range. The low electronic density its atomic thickness makes graphene (or other 2D material like BN) an excellent material as a window, as it allows for more transmission of photoelectrons from the sample inside the cell and less attenuation from the membrane itself. As shown in d-f in Figure 2.11, these graphene membranes are typically supported on a perforated silicon nitride window, with the holes diameters being typically on the order of a few hundred nanometers, which balances the mechanical strength of graphene membrane and the wetting/mass transfer of electrolyte to the graphene. Graphene can be prepared by either self-assembly by Langmuir-Blodgett method or chemical transfer from CVD graphene. In the former case the exact thickness of graphene flakes is not well controlled, so the graphene transfer method is now the standard one for fabrication (175). The fabrication details will be covered in the next section 2.3.1 and appendix.

The challenges of the graphene liquid cell approach are related to the fabrication method of the graphene, which is found to break easily under bias and under X-ray illumination. Ions driven by the electric field to the interfaces or produced by X-ray induced ionization/ hydrolysis can both react with and damage the graphene sheet (176). The graphene itself, in all current fabrication methods, consists of many grains on the size of microns and therefore contain numerous grain boundaries with weaker C-C bonds that facilitate their reaction and rupture.

Graphene supported on polymer electrolyte membrane (PEM) film has much higher stability than the free-standing graphene and has been successfully used for electrochemical XPS in many cases, such as Pt and Ir for oxygen evolution reaction studies (48, 51, 52, 177).

In the last few years graphene liquid cells have also been introduced to the near-field spectroscopic imaging techniques. The attenuation of the IR near field from the tip apex is around 15nm, so the thickness of the membrane should be less than 10nm. Graphene is then a great candidate for this purpose. As shown in a and b in Figure 2.11, graphene membranes separate the AFM tip with the sample solution and prevent the damage/contamination of both tip and sample. Single layer graphene is also transparent to the IR near field so that vibration information of molecules underneath the graphene layer could be revealed (154, 155).

Immediately after the application of graphene-liquid cell for these techniques, functionalization of graphene membrane becomes a hot topic, as graphene is not the only material of interest. Graphene can be covered with a layer of nanoparticles, polymer, protein or oxide/metal film, but most of the signal comes from the graphene-material interfaces, and the interpretation of the data becomes sophisticated.

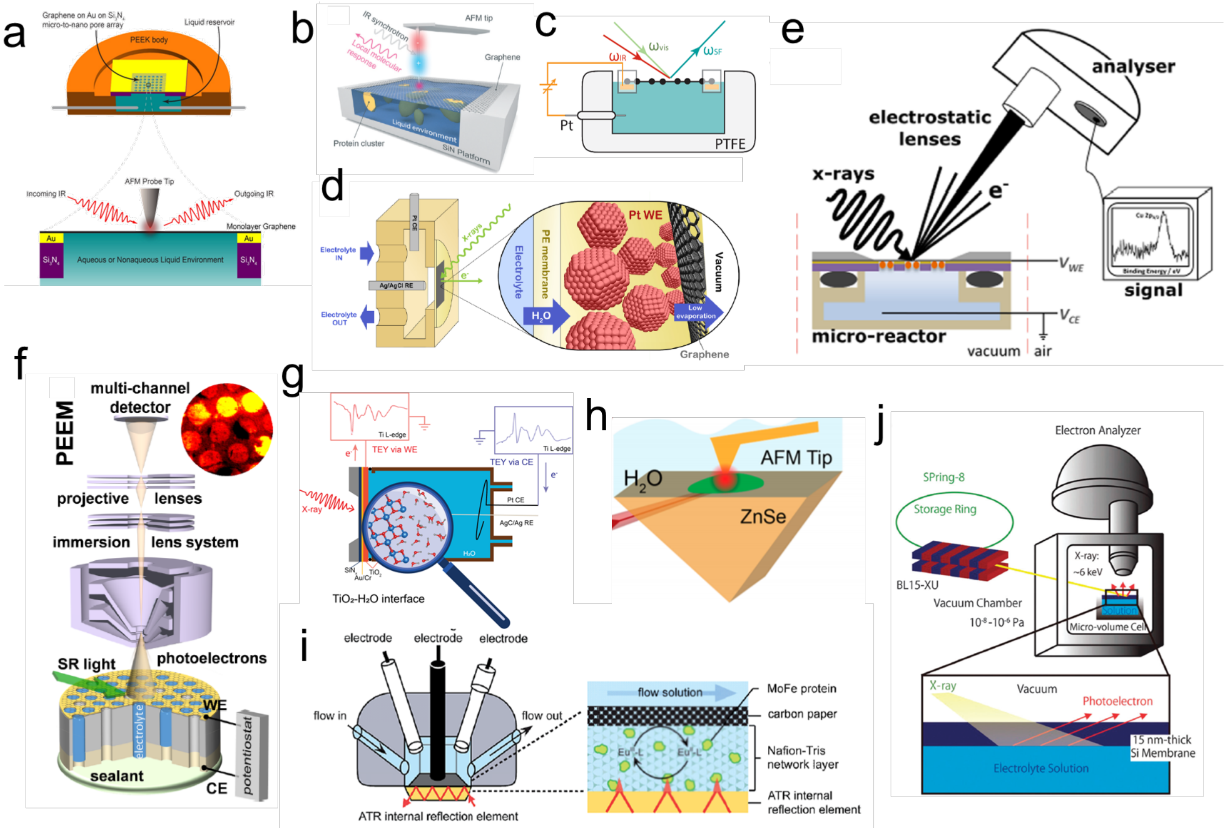

Figure 2.11 Illustration of closed liquid cell for surface-sensitive spectroscopy. Single/multiple layer graphene are used as window from a) to f), and photo-transparent membrane/crystal are used in g) to j).

(a) graphene liquid cell for nano-FTIR. Reprinted with permission from ref (155). Copyright 2019 American Chemical Society. (b) graphene microcell on a silicon chip for nano-FTIR. Reprinted with permission from ref (154). Copyright 2019 Royal Society of Chemistry. (c) Floating graphene as window for SFG. Reprinted with permission from ref (86). Copyright 2022, with permission from Creative Commons. Licensed under CC BY 4.0. (d) Graphene supported on PEM film as window for electrochemical XPS. Reprinted with permission from ref (51). Copyright 2019, with permission from Creative Commons. Licensed under CC BY 4.0. (e) Multi-layer graphene supported on holy SiNx membrane for electrochemical XPS. Reprinted with permission from ref (178). Copyright 2022, with permission from Creative Commons. Licensed under CC BY-NC-ND 4.0. (f) Multi-layer graphene supported on holy SiNx membrane as window for electrochemical PEEM. Reprinted with permission from ref (179). Copyright 2017 American Chemical Society. (g) SiNx membrane as window for EY-XANES. Reprinted with permission from ref (23). Copyright 2022, with permission from Creative Commons. Licensed under CC BY 4.0. (h) In liquid nano-FTIR, with the light goes through ZnSe prism. Reprinted with permission from ref (152). Copyright 2020 American Chemical Society. (i) Electrochemical cell for ATR-FTIR. Reprinted with permission from ref (180). Copyright 2017, with permission from Creative Commons. Licensed under CC BY 3.0. (j) Electrochemical cell based on thin SiNx membrane for hard XPS. Reprinted with permission from ref (173). Copyright 2013 AIP publishing.

2.3.Fabrication procedures

2.3.1. Graphene membrane

Up to now numerous graphene transfer methods have been reported, including mechanical exfoliation, chemical wet transfer, dry (tape) transfer, sonication, etc. Many of these methods are now commercialized. However, most of them are not suitable for the application in liquid cells. For instance, in mechanical exfoliation, the thickness and size of graphene flakes is not well controlled, while in dry transfer the adhesive tape used might damage the supporting perforated silicon nitride window.

Two graphene transfer approaches starting from CVD graphene are finally suitable for these purposes: PMMA-assisted wet transfer and polymer-free wet transfer (153, 155, 181). In PMMA-assisted transfer a PMMA layer is spin coated on top of CVD graphene to increase the mechanical stability and prevent graphene shrinking before the etching process and removed after the transfer process by hot acetone or vacuum annealing. For polymer-free transfer a frame, with the details shown in the appendix, instead of PMMA layer is used to stabilize the free-standing graphene and reduce contamination.

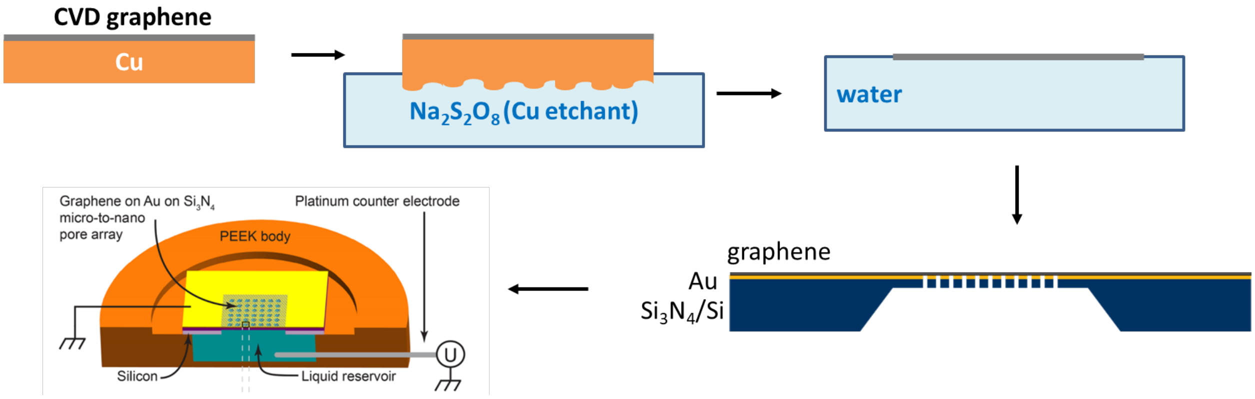

Figure 2.12 Illustration drawing of the graphene transfer process. The CVD graphene grown on copper (top left), copper under etching (top middle), graphene washed by DI water (top right), graphene transferred onto holy SiNx membrane (bottom right) and finally closing the liquid cell (bottom left).

The polymer free graphene transfer method was used in this dissertation. In brief, commercial single-layer graphene grown on Cu foil (Graphene Factory) by chemical vapor deposition (CVD) was used as base material. Residual graphene on the other side of the foil was removed by O_2 plasma. An adhesive Al foil frame window was stuck to the untreated side and then floated on a Cu etchant solution (~90ml 0.2 M sodium persulfate). After etching out the Cu the graphene with the Al window frame, was transferred to a deionized water reservoir (~500 ml) to remove salt residues. The transfer process to the water reservoir was repeated twice to ensure complete salt removal. A Cr (2.5 nm)/Au (25 nm) coated SiN membrane (100 nm thickness) perforated with an array of 1000 nm or 500 nm circular holes (Norcada) was placed in the reservoir underneath the graphene and carefully lifted up from the air/water interfaces to scoop the graphene and complete the transfer. After this the membranes were annealed in vacuum (lower than 10-6 torr) up to 573K to increase the adhesion between graphene and Au.

The details can be found in the appendix.

2.3.2. Oxide/metal membrane

Thin free-standing oxide/metal membrane have also been developed for various purposes, including liquid/gas cell XPS, nano-FTIR and KPFM. The oxide is deposited and supported by the graphene, to act as an electrode for electrochemical applications, or free-standing for other applications.

Figure 2.13 (a) shows a schematic representation of the fabrication process of oxide or metal film. It starts with a graphene film, or a formvar film (transfer with the same method, only substitute the graphene by formvar) supported on holy SiNx membrane. The oxide film is grown by plasma enhanced atomic layer deposition (PE-ALD) (182-186) on either side of the graphene (182-184), as illustrated in Figure 2.13 (a) step iii-a and iii-b. The graphene can be removed, if desired, by oxygen plasma to leave only the suspended metal oxide (step iv in Figure 2.13 (a)). Typically, however, we keep the graphene on the external side of the window as it adds mechanical strength and because it provides good electrical conductivity for biasing the metal oxide when acting as an electrode. Figure 2.13 (b) shows an atomic-force microscopy (AFM) topographic image of a region of the SiN with holes capped with graphene, while (c) is an image of the same area with a 2 nm TiO_2 film grown on the side facing the cell interior (corrugated side), showing its excellent conformal distribution. Figure 2.13 (d) shows a region of an Al_2O_3-covered array of holes which were initially covered by a Formvar polymer (polyvinyl formal). The polymer acts as support for the PE-ALD growth and was subsequently dissolved in chloroform so that the metal oxide membrane is freely suspended.

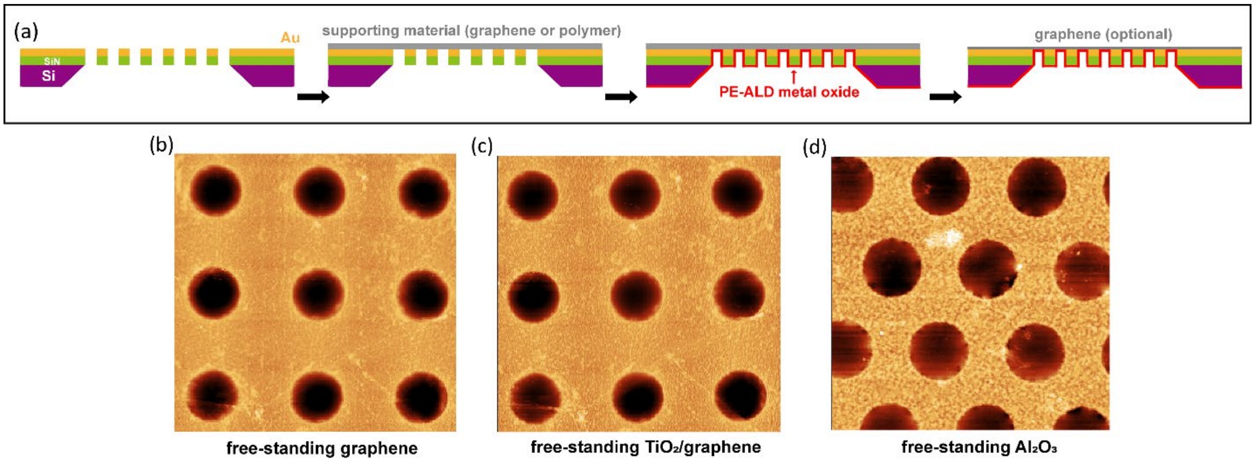

Figure 2.13 (a) Fabrication process of the free-standing ultra-thin metal oxide membranes. (b-d) AFM topographic image showing a region with a graphene/Formvar-capped array of holes ($\phi = 1$ µm), corresponding to step ii (before oxide deposition), step iii-a (after deposition of a TiO_2), step iv (after depositon of Al_2O_3 on Formvar (polyvinyl formal) as support). Reprinted with permission from ref (181). Copyright 2020 American Chemical Society.

For gas/liquid cell XPS and KPFM, the desired oxide/metal should be deposited on the corrugated side, since the top side residue material never contacts the solution while contribute more to the total signal strength (for the reversed approach where the flat side is in contact with solution, the corrugated side should not be coated). But ALD film is usually very conformal, exhibiting a very high aspect ratio, which means that both sides will be coated. Therefore, a special sample holder was used to block one side of the membrane. This sample holder is shown in Figure 2.14. SiNx membrane was placed down, with the flat side facing a Si chip substrate. Two screws were used to gently press the membranes against the Si chip. The nm scale flatness of Si ensures minimal precursors enter the gap between the SiNx membrane and the Si chip.

Graphene is chemically inert to thermal ALD, so plasma was used carefully to activate the graphene and reduce nucleation delay. For the PEALD deposition of SiO_2, Al_2O_3, TiO_2 and CoO_x, the deposition temperature was kept at room temperature or 393K and nucleation delay was found to be less than 20 cycles while for metal ALD deposition (473K, Pt) double layer graphene was used and the graphene was oxidized by O_2 plasma for 120s before deposition.

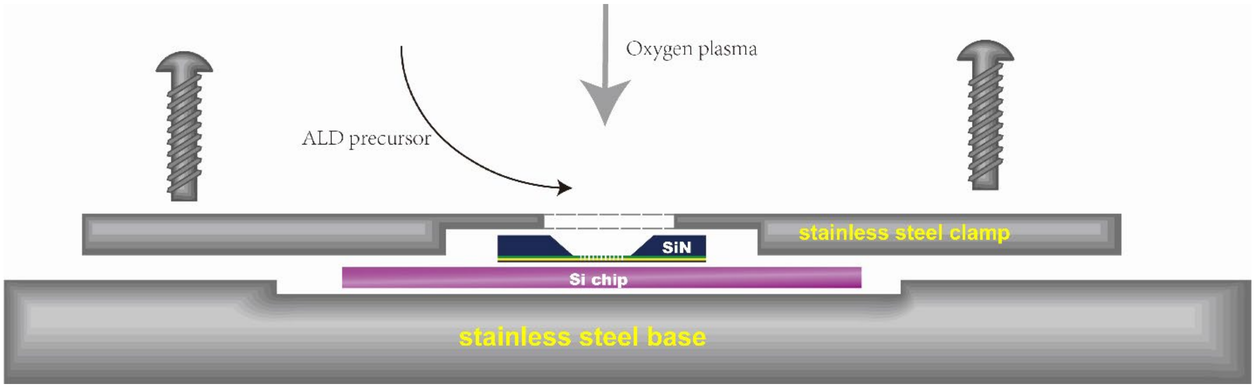

Figure 2.14 illustration of the ALD membrane holder for single side coating from a cross-section view. Reprinted with permission from ref (181). Copyright 2020 American Chemical Society.

The chemical composition and uniformity of the films were examined by scanning Auger spectroscopy (with spatial resolution of few nm), and by TEM/electron energy-loss spectroscopy (EELS). As shown in Figure 2.15 (a), when a TiO_2 film is deposited on the side facing the cell interior (corresponding to the SEM image in Figure 2(b)), the Ti LMM Auger peaks only appear when the electron beam is focused on the free-standing graphene/TiO_2 (magenta) but not on the region between holes (blue). Because of the short inelastic mean free path of the 380-eV Auger electrons (around 1 nm), the spectra show only Ti peaks on the suspended graphene region of the membrane. Figure 2.15 (c) shows a TEM image of a region of a SiN hole that is partly covered by a free-standing graphene/TiO_2 membrane (the missing part of the membrane is the brightest part). The Ti-$L_{2,3}$ edge EELS map from the region marked by a square that includes the ruptured edge is shown in Figure 2.15. Focusing on this edge region reveals the abrupt change in chemical contrast across the edge, confirming the continuity and uniformity of the metal oxide layer over the free-standing graphene. An electron-diffraction pattern from the electron beam irradiating the graphene/TiO_2 area is shown in Figure 2.15 (e). Only the hexagonal diffraction pattern from graphene can be seen since the amorphous metal oxide does not produce diffracted beams. This is expected from the low-temperature (313-393K) metal oxide deposition conditions(182-185, 187). Similar results were obtained for Al_2O_3/graphene membranes.

At the temperature used in the PE-ALD growth process, a high content of carbon (around 15%) was observed by XPS as a residue of the organic precursor. Surface OH^- groups could also bring out an excess of oxygen(188, 189). In a separate test, a 20 nm thick Al_2O_3 layer was grown on a SiN wafer to study in more detail its chemical composition and the possibility of cleaning the surface OH^- groups without altering the structural quality of the ultra-thin membranes. Figure 2.16 shows an XPS depth profile measurement and how the initial element concentrations of the uppermost layer converge to the stoichiometric 3/2 O/Al ratio in the bulk. The profile also shows that the carbon content drops to less than a 2% in the Al_2O_3 bulk. The carbon and OH^- groups can be eliminated by a gentle sputtering with Ar_{75}^+ clusters at low energy (8000 eV) without discernible damage on the ultra-thin film deposits (190).

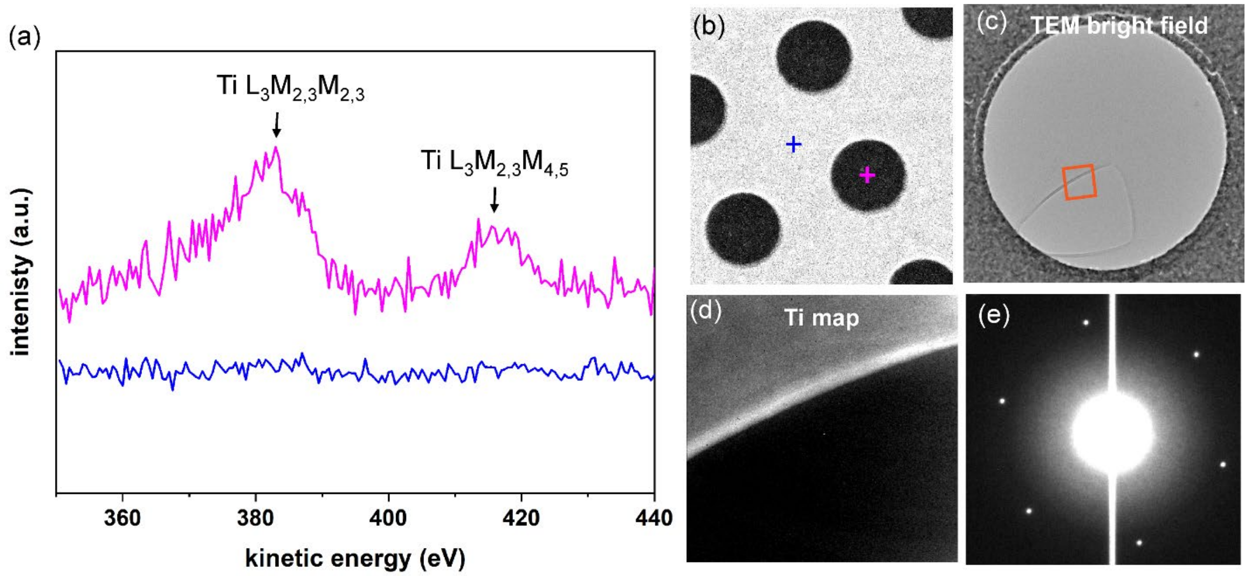

Figure 2.15 (a) High spatial resolution (a few nm) Auger-electron spectroscopy (b) SEM of 2nm graphene/TiO_2 window. (c) TEM bright-field image from a partially ruptured graphene/TiO_2 window (Ø = 1000 nm). (d) EELS (Ti-L edge) map from the region marked by a square in (c) containing the edge of the ruptured. (e) Electron diffraction pattern from a TiO_2/graphene region showing the hexagonal pattern from graphene with the amorphous TiO_2 contributing only to the background. Reprinted with permission from ref (181). Copyright 2020 American Chemical Society.

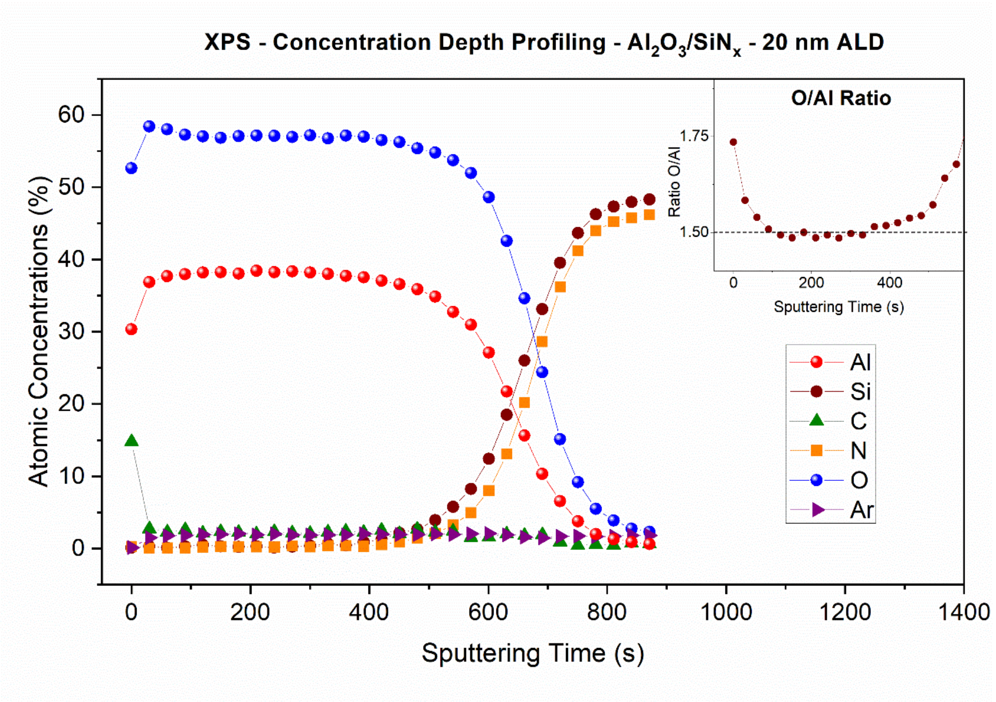

Figure 2.16 Depth profile XPS measurements of a 20 nm Al_2O_3 thin film grown by PE-ALD on a SiNx substrate. Reprinted with permission from ref (181). Copyright 2020 American Chemical Society.

2.3.3. Mechanical test

The mechanical behavior of the free-standing metal oxide membranes was investigated by nano-indentation using an AFM tip. To check for indentation-induced damage to the tip, AFM topographic images were acquired before and after each indentation. Figure 2.17 shows representative force-distance curves on a 1-µm-diameter hole covered with a suspended graphene membrane without (blue) and with (black) a 2-nm-thick TiO_2 film deposited on the membrane facing the cell interior. Only a small difference is visible between the loading and unloading curves in both cases, suggesting an elastic deformation process and no sliding between the graphene and TiO_2 layers during indentation, which is indicative of strong adhesion between graphene and TiO_2. The effective Young's modulus (E) of the suspended membrane was calculated using the following equation (183, 184, 191), which describes the force vs indentation depth of a suspended clamped circular sheet of an isotropic elastic material under a centrally applied load,

$$\mathrm{F} = \left[3\frac{4\pi E}{1-\nu^2}\left(\frac{t^3}{a^2}\right)\right]\delta + (\pi T)\delta + \left(\frac{q^3Et}{a^2}\right)\delta^3$$

where t = thickness of the suspended membrane, ν = effective Poisson's ratio, a = radius of the suspended membrane, T = pre-tension in the suspended membrane, q is a dimensionless parameter equal to $1/(1.05 - 0.15\nu - 0.16\nu^2)$, F = applied force, and δ = indentation depth. By using the equation and fitting the force-indentation curves, shown as green and red curves corresponding to graphene and graphene/TiO_2, respectively, in Figure 2.17, we obtain the Young's modulus of graphene, $E_{graphene}$, to be around 404 ± 14 GPa and that of the 2-nm-thick TiO_2 film on graphene, $E_{graphene/TiO2}$, to be 200 ± 100 GPa. These values are close to the values reported in the literature(183, 184), The $E_{graphene}$ value, however, is lower than that reported for graphene prepared by mechanical exfoliation of graphite (~1 TPa) (191), which could be due to defects in the graphene used in this study stemming from the chemical vapor deposition process and/or from the transfer processes. Assuming a tip radius between 10 and 50 nm, we estimate that our free-standing metal oxide membrane can withstand local pressures higher than 10^6 Pa, i.e, more than 10 bar, which explains its good performance as an environmental cell window to contain high pressure gas or liquids.

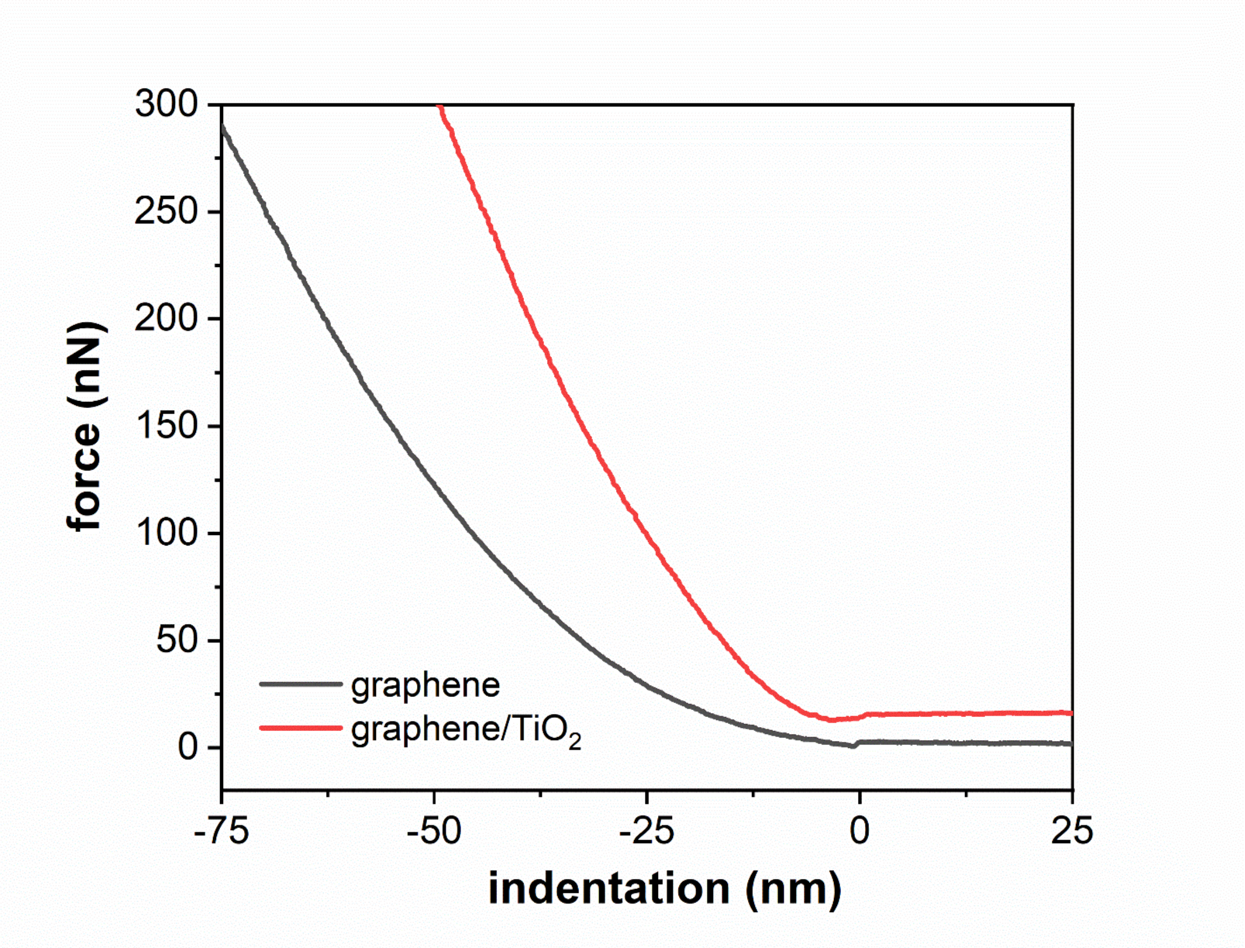

Figure 2.17 AFM nanoindentation curves of a suspended graphene (blue) and graphene/TiO_2 (black). The green and red curves correspond to the fitting results of graphene and graphene/TiO_2, respectively. The inset shows a schematic of the AFM nanoindentation experiment. Reprinted with permission from ref (181). Copyright 2020 American Chemical Society.

The mechanical strength of free-standing metal oxide membrane was also tested using a home-built pressure test station, which is shown in Figure 2.19. The pressure of the cell was brought up gradually by filling it with Argon while the chamber was pumped by both turbo and mechanical pump. The pressure inside the cell and outside the cell were recorded simultaneously and plotted in Figure 2.18. The pressure in the chamber increased as the gas pressure inside the cell increased from 1bar to 2 bar, suggesting there might be some leak or open holes. As the pressure kept increasing the turbo was turned off to protect the pump. The gas pressure was maintained up to 4 bars (the cell was isolated from the gas supply). Considering that the volume of the cell is much smaller than that of the chamber (more than 1000 times) we can conclude that most of the oxide membrane was still intact as the pressure went up. This experiment demonstrate that the free-standing oxide membrane can indeed hold pressure difference for at least 4 bar.

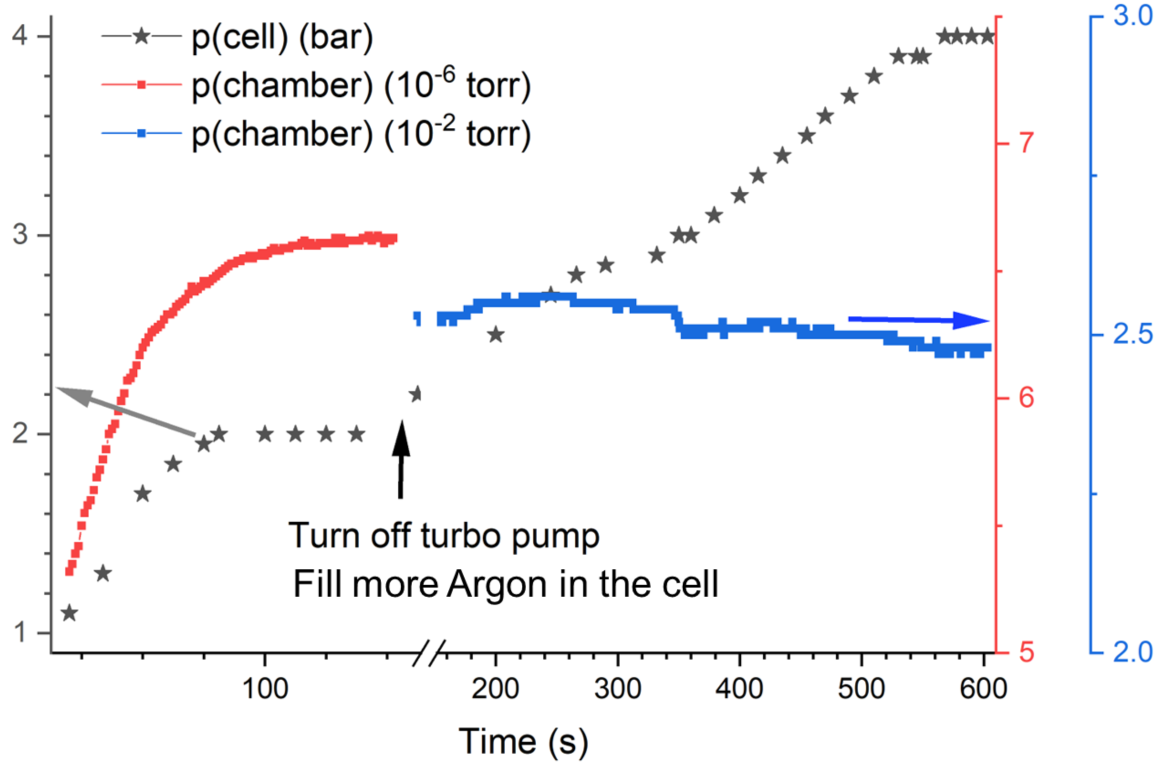

Figure 2.18 Mechanical test of the oxide film, with one side filled with gas, and other side vacuum.

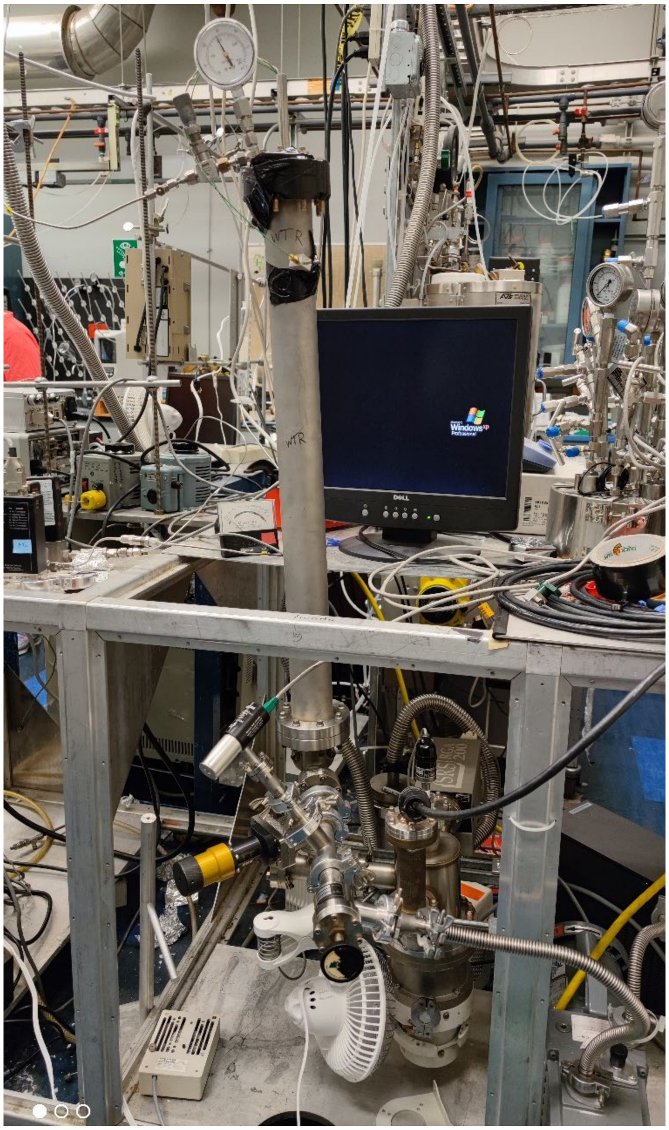

Figure 2.19 Vacuum tube with pump station for mechanical test of the liquid cell.

The sub-micrometer thickness of SiN membranes (and other materials) makes them transparent to high-energy radiation, in particular ≥100 keV electrons and X-rays, and for that reason they are frequently used for TEM (192, 193), and for X-ray absorption spectroscopies in the fluorescent-yield detection mode (FY-XAS) (194, 195). Other surface-sensitive spectroscopies such as XPS and EY-XAS which use emitted electrons traversing the membrane are not possible with standard SiN membranes because of the short mean free path of a few nm of low-energy electrons in solid materials. However, the ultra-thin metal oxide films presented above make possible XPS measurements of species present near the membrane, similar to the case of graphene (196). Figure 2.20 (a) and (b) shows the N1s and O1s photoelectron spectra from air at 1 bar enclosed by a 2-nm-thin Al_2O_3 free-standing membrane. The cell is located inside a vacuum chamber with 10^{-6}-10^{-7} Torr base pressure containing an XPS spectrometer. In Figure 2.20 (a), The N1s spectrum shows a sharp peak at a binding energy of ~405 eV from the N_2 gas phase, together with a small contribution at ~400 eV from N in the SiN support (196). Similarly, in Figure 2.20 (b), the O1s spectrum shows a doublet peak (due to paramagnetic splitting) at ~537-540 eV corresponding to the O_2 gas phase (197, 198) and another larger peak at 532.5 eV from the O in the Al_2O_3 membrane. The integrated intensity ratio of the N_2 to O_2 peaks is close to 4, as expected from the air composition.

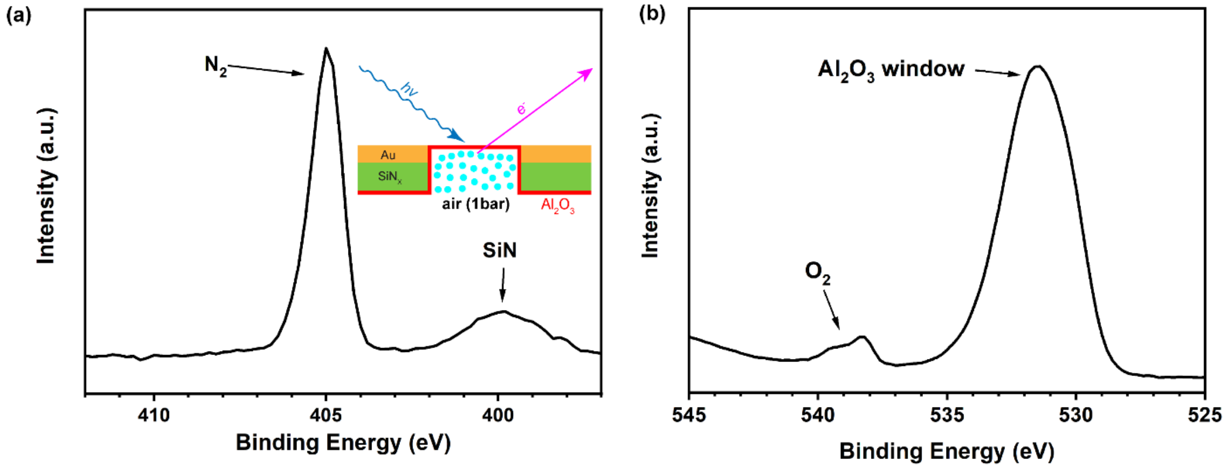

Figure 2.20 XPS measurements through a 2-nm-thick Al_2O_3 membrane closing a cell filled with 1 bar of air. The cell is located inside an XPS vacuum chamber with a 10^{-6} to 10^{-7} Torr background pressure. (a) N1s spectra, containing a sharp peak from N_2 gas in air and a smaller peak from the SiN support. (b) O1s peak showing the doublet peak from O_2 gas in air and a strong, broad peak from the Al_2O_3 oxide. The photon energy is 1135 eV. Reprinted with permission from ref (181). Copyright 2020 American Chemical Society.

2.4.Measurement methods

2.4.1. Atomic Force Microscopy (AFM)

Atomic Force Microscopy is typically used to measure the morphology of the membrane, and to count and mark the open holes (those not covered by graphene) of the membrane. The Icon and multimode AFM system from Bruker were mostly used for that purpose (Figure 2.21). In a typical experiment the cantilever holding the tip mechanically oscillated at its 75 kHz resonance frequency, with the free amplitude set to around 20nm. The set point is usually slightly higher (~12nm) to let AFM work in the attractive regime in most cases. Topographic height, phase, and amplitude error in tapping mode, and topographic height, modulus, and peak force error in peak force mode were recorded and compared to determine the percentage and locations of open holes/cracks of graphene.

Cypher AFM and Jupiter AFM were also used for topography and mechanical measurements (Figure 2.21).

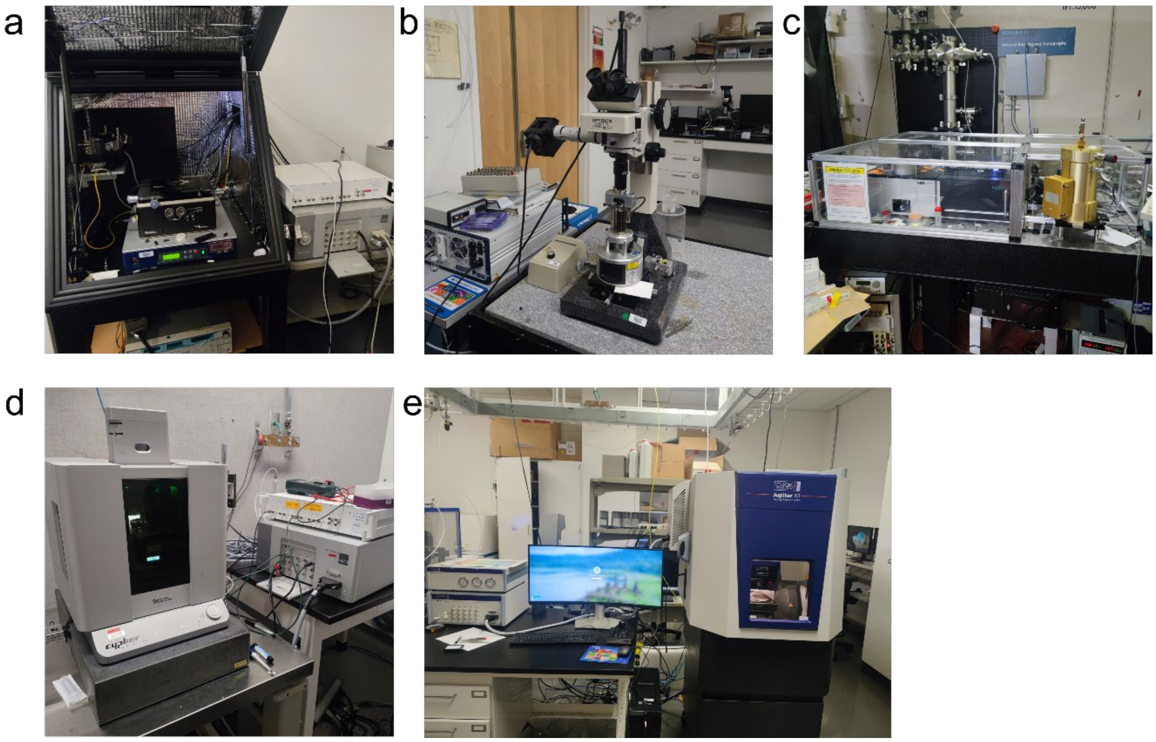

Figure 2.21 AFM setups used in the dissertation. (a) MFP-3D AFM for KPFM (b) Multimode AFM for topography (c) Neaspec nano-FTIR (beamline 2.4) for nano-FTIR experiments (d) Cypher AFM for in-liquid AFM and mechanical test (e) Jupyter AFM for topography and KPFM

2.4.2. Infrared Nanospectroscopy (nano-FTIR, or IR-SNOM, or SINS)

Synchrotron based nano-FTIR (also known as Synchrotron Infrared Nano Spectroscopy, SINS) measurements were performed at beamline 2.4 of the Advanced Light Source at the Lawrence Berkeley National Laboratory, using a neaSNOM (Neaspec, Germany) system (Figure 2.21). The measurements were performed under an inert environment with a constant N_2 purge and a <5% relative humidity. To minimize tip contamination, the IrPt-coated AFM tip was operated in noncontact tapping mode at the fundamental resonance frequency of the cantilever (250-350 kHz) with a free oscillation amplitude ranging from 70 to 80 nm and an amplitude setpoint of ~85%. Mercury-Cadmium-Telluride (MCT) detector and Copper doped Germanium (Cu:Ge) detector were used to collect high energy ($1000\text{-}2000\text{cm}^{-1}$) and low energy ($400\text{-}1000\text{cm}^{-1}$) IR photons, respectively. The scattered near-field IR signal is further filtered by a lock-in amplifier tuned to the second and higher harmonics of the cantilever oscillation to separate it from the far field non-local scattering background.

The complex-valued near-field spectrum is derived from a Fourier transform of the interferogram. The Fourier components can be expressed as real spectral amplitude "A" and phase "∅", both normalized to reference spectra:

$$A_i(v) = A_i^{sample}(v)/A_i^{reference}(v)$$

$$\emptyset_i(v) = \emptyset_i^{sample}(v) - \emptyset_i^{reference}(v)$$

where v is the wavenumber, with the reference spectra collected on bare Au-coated Si substrates. The nano-FTIR spectra displayed throughout the paper is the phase φ_2 of the scattered signal at the second harmonic of the cantilever oscillation frequency, which has been shown to be in good agreement with traditional FTIR absorption measurements (134, 136, 155). Each nano-FTIR spectrum has a third order polynomial background subtracted. The negative band around 1270 cm^{-1} present in all cases is likely associated with polydimethylsiloxane (PDMS) contamination on the AFM cantilever and tip, a material present in the gel box used to hold the AFM tips.

2.4.3. Kelvin Probe Force Microscopy (KPFM)

The MFP-3D AFM was used for KPFM measurements. The cantilever holding the tip mechanically oscillated at its 75 kHz resonance frequency, with free amplitude of around 15nm. The driving signal was provided by the output of a Zurich lock-in amplifier, as shown in Figure 2.21 (a). The cantilever was biased also using the output of the lock-in amplifier, which bias consisted of a DC plus a 2 kHz AC bias of 3.5V amplitude. The cantilever oscillation signal was then fed into the lock-in amplifier and the sideband was minimized dynamically by varying the DC offset value, which is equal to the CPD. The mechanical set point was usually set close to 10nm to ensure the tip worked in the attractive regime. The scan speed was carefully chosen to make sure the CPD contrast has the least influence from the topography. Both lock-in amplifier and graphene membrane were grounded. During the KPFM measurement the AFM was isolated from the outer environment to reduce the mechanical noise, and after the experiment the CPD value inside the suspended region was extracted from the images and referenced by the surrounding area.

2.4.4. Electron Yield X-ray Absorption Near Edge Spectroscopy (EY-XANES)

X-ray absorption can be measured directly by the attenuation of the primary photons during transmission or indirectly by measuring decay products, fluorescent photons or electrons, produced by the decay of excited core-hole states of the atoms absorbing the X-ray photons by transitions of electrons near the Fermi edge of the valence band. XAS is bulk sensitive measured in transmission or via fluorescence due to the long mean free path (>micrometers) of the X-rays. Conversely, in the electron yield mode, XAS can be highly interfaces sensitive.

The electrochemical flow cell used for XANES was made of PEEK (polyether ether ketone, a highly electrically insulating material), sealed by an X-ray-transparent 100-nm-thick SiNx membrane. The cell was loaded in the IO-XAS endstation of the IOS (23-ID-2) beamline at the National Synchrotron Light Source II, at the Brookhaven National Laboratory and at beamline 8.0.1 at the Advanced Light Source (Figure 2.22), at the Lawrence Berkeley National Laboratory. Deionized H_2O (Milli-Q 18.2 MΩ) was used without further degassing. As reference, the X-ray absorption spectra were also measured under ultrahigh vacuum (UHV), using total electron yield via the sample drain current.

Drain currents were measured at the counter electrode with the working electrode grounded, or at the working electrode with the counter electrode grounded.

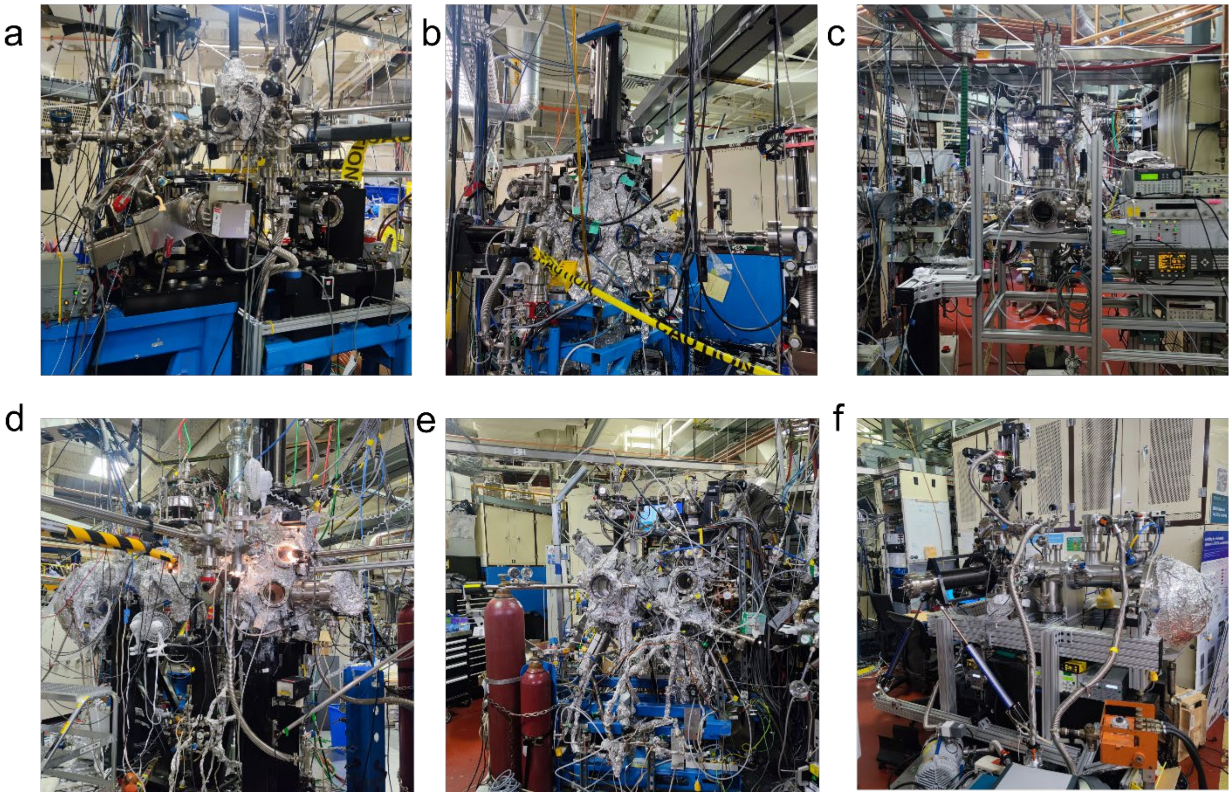

Figure 2.22 End stations at the various and beamlines for X-ray based techniques used in this dissertation. (a) XANES in beamline 7.3.1 (b) XANES in beamline 8.0.1.4 (c) home built XANES in beamline 9.0.1 (d) XPS in beamline 9.3.2 (e) XPS in beamline 11.0.2.1 (f) end station with liquid cell capability for beamline 11.0.2.1.

2.4.5. Sum Frequency Generation (SFG)

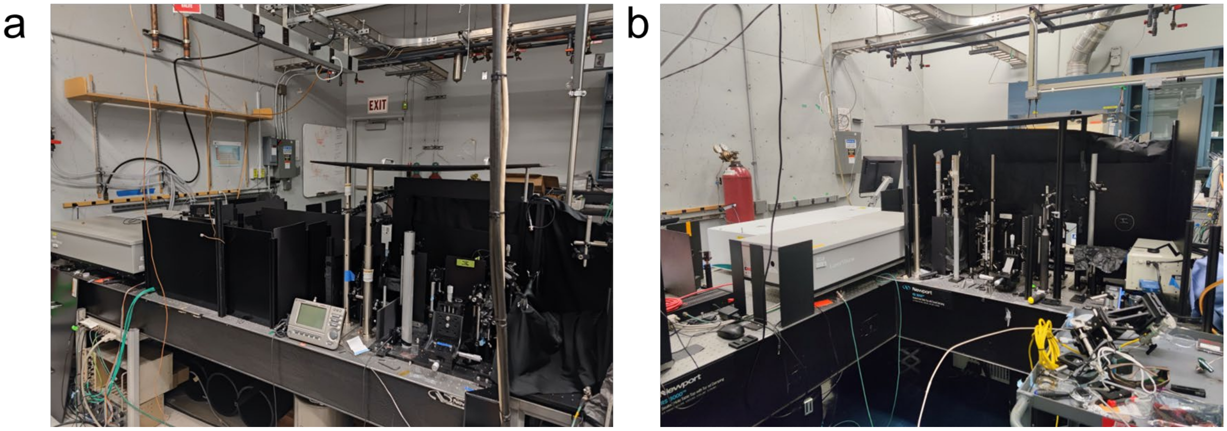

Figure 2.23 SFG setups for solid-liquid interfaces.

Figure 2.23 shows the SFVS-electrochemical cell set-up used in this Thesis, with a picosecond laser system to generate a 1064 nm near-infrared light with repetition rate of 20 Hz (199). A Laser Vision optical parametric generator and amplifier system converts the 1064 nm light to a visible 532 nm beam and a mid-infrared beam ranging between 2200 cm^{-1} to 4000 cm^{-1}. Sum frequency generation is achieved when the visible and infrared beams overlap spatially and temporally on the sample. The intensity of the sum frequency (SF) light as a function of IR frequency is a vibrational spectrum of the surface species measured in the visible region. All the spectra reported in this work were acquired with an SSP polarization combination, where the letters indicate the polarization of the sum frequency, visible, and IR beams, respectively.

2.4.6. Other techniques: TEM, XPS, SEM, Raman, FTIR

Other techniques including Raman, FTIR, SEM and XPS were frequently used to monitor the quality of graphene/graphene supported films. Raman was used to probe the graphene doping and layers/stacks, FTIR served as reference for nano-FTIR experiments, SEM and TEM were used to map the morphology of graphene membrane and graphene supported nanoparticles, XPS was used to determine the impurities and the chemical states of the sample.

Conclusions

This chapter briefly reviewed various surface-sensitive spectroscopic techniques for solid-liquid interfaces, including their basic principle, surface sensitivity, and their adaptation to liquid environments. X-ray based techniques (EY-XANES, XPS) are surface sensitive since only photoelectrons or secondary electrons produced near interfaces are collected; SFG/SHG are only sensitive to molecules with no central symmetry, which in this case are molecules near the interfaces. SERS, SEIRA and SNOM take advantage of the surface plasmonic enhancement from metallic electrode, and other spectroscopic techniques such as ATR-FTIR and THz use subtraction with spectra in reference conditions to track the chemical changes at the interfaces.

By directly exposing the liquid to the excitation source, or by enclosing the liquid in a closed cell, many surfaces sensitive techniques can now operate in liquid environments. For some applications the penetration of beam in the aqueous solution is small, so that the membrane itself becomes the material of interest. The membrane could be a thin silicon, silicon nitride, single/multilayer graphene, or membrane supported films or nanoparticles.

The liquid cell approach enables liquid circulating and refreshment, so the sample damage (by radiation or tip) reduces. The electrochemical setup is also close to that in normal electrochemistry setups, with unlimited mass transfer between the interfaces and the bulk liquid.

The fabrication of graphene and oxide membranes is also shown in this chapter.

Chapter 3 Probing the Electrical Double Layer structure

Abstract

The structure and properties of the electrical double layer (EDL) is a topic of great interest and controversy. For most research works in the field of electrochemistry the EDL structure and properties were assumed to be explained well by simple models, such as Helmholtz model or Stern model, but experimental characterization to elucidate, or even to confirm the validity of these models is still lagging. To simplify the mathematics of the EDL structure many assumptions have been made, which in most real cases give incorrect results. Chapter 3 shows how complex interactions are derived from these assumptions, and how they predict unexpected structures and properties.

Historical development of EDL models

Electrical double layer (EDL) is defined as the interfacial region between the electrode and bulk electrolyte, of which the structure is drastically different from the bulk. The counter ions accumulate to the electrode surface, and the co-ions are depleted from the interfaces. Under certain conditions the energy landscape of ion hydration structure is also different in the EDL compared to the bulk. In aqueous solutions water can form special hydrogen bonds to the electrode which results in a preferential orientation, depending on the nature of the electrode-water interaction and bias. The water molecules can protonate, deprotonate, and coordinate the surface and alter the interfacial properties in turn. All these properties of EDL have a critical impact on numerous natural processes and applied research, such as electrochemical energy storage and conversions, heterogeneous nucleation, and corrosion. A molecular understanding of the EDL from both theoretical and experimental methods has been a principal focus of material scientists over many decades (3, 158, 200-215).

The earliest EDL model dates to almost 170 years ago by Helmholtz in 1853. In his model the EDL is defined by two parallel planes with equal but opposite charges, one for the electrode surface and another for the solvated counter ions that reach to the proximity of electrode (later referred as the outer Helmholtz plane, OHP). The Helmholtz model predicts the EDL capacitance in the same magnitude as experimental value, but the model is also too simple and fails in explaining many electrochemical behaviors.

The EDL model was improved by Grahame, Gouy and Chapman. Grahame took specifically absorbed ions with broken solvation shells into consideration and defined it as inner Helmholtz plane (IHP). Gouy and Chapman used Poisson-Boltzmann equation to describe the ion distribution near the interfaces. Stern modified their theory and divided this region to an inner layer where the ions cannot access and diffuse layer, where the potential drops exponentially into the bulk electrolyte. The Gouy-Chapmann-Stern (GCS) model can already account for many experimental observations.

However, this model also has many weaknesses. It assumes that the ions are infinitely small and only interact by electrostatic force while neglecting any other correlations, including steric effects and formation of hydrogen bonds. This often results in a large discrepancy between the model and the experimental conclusions (201, 216-218). The electrode surface is also assumed to be perfectly sharp without spatial inhomogeneous. Many parameters used in this theory are adopt from bulk properties, such as the dielectric constant, while some recent experiments suggested that the dielectric constant of confined water at IHP is distinct from that in the diffuse layer (219, 220).

Many modifications and refinement in the following decades helped to improve the GCS model. For example, steric effect of ions, dipolar nature of water molecules and different permittivity have been taken into consideration (200-202, 221). These models and the mean-field theory have been widely accepted and utilized to interpret many macroscopic and microscopic electrochemical phenomenon. However, not all electrochemical behaviors can be explained by these models, even for a simple case, conductive flat electrode in contact with electrolyte (219, 222-224).

Beyond mean field theory, molecular dynamics, and classical density function theory (DFT) have also been used to simulate the EDL structure and properties. Recent development of DFT with Grand Canonical ensemble has become popular for electrochemical simulations and provide more details on EDL electronic structure (225).

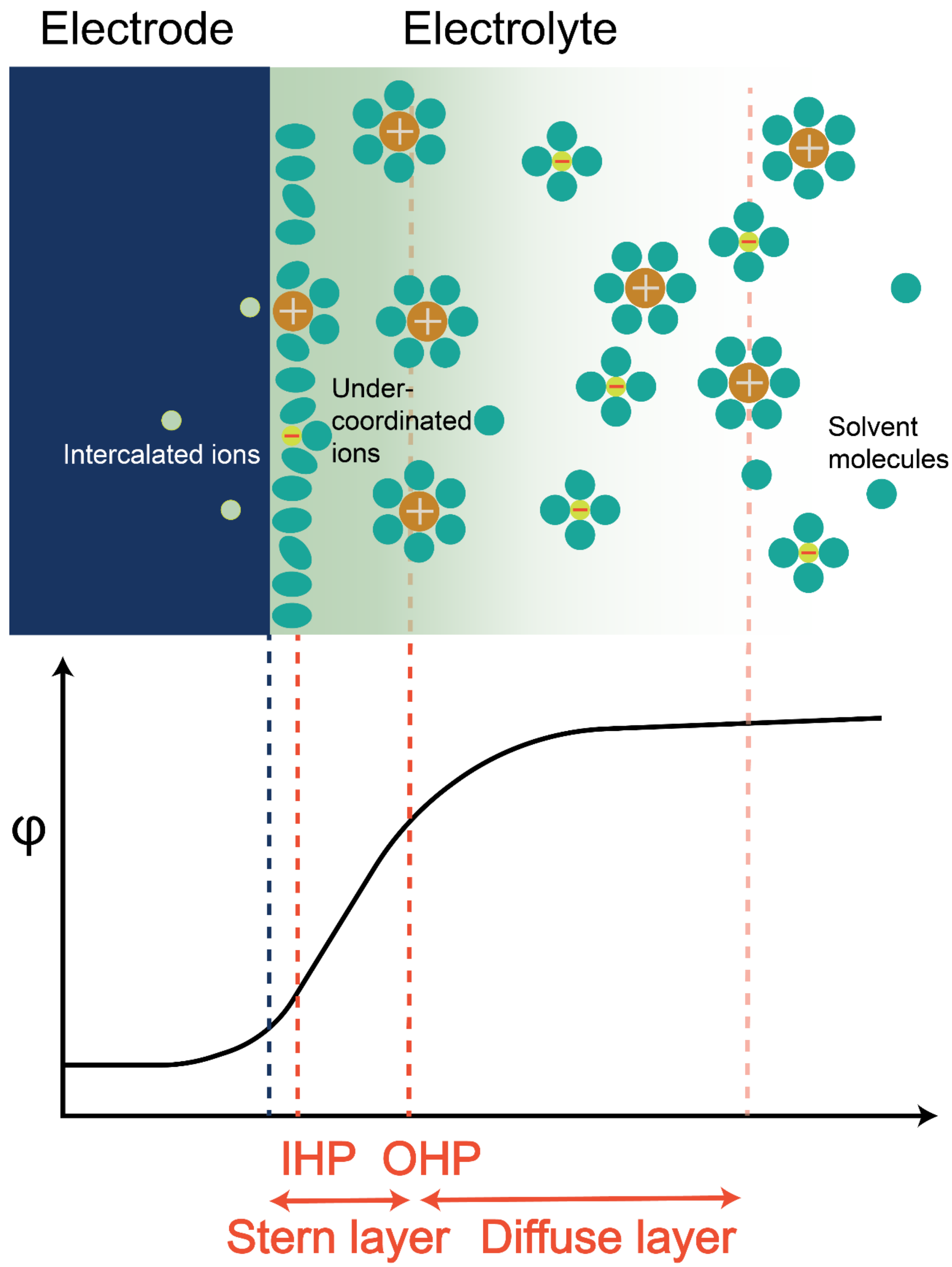

Figure 3.1 Classical model of the electrical double layer showing the Stern layer and the diffuse layer

Case I: graphene-sulfate solution interfaces

The graphene-electrolyte interfaces plays an important role in many applications and technological fields, such as electrocatalysis, energy storage, water desalination (226, 227), electricity generation (228-231), environmental (232-239), and biological sensors (240). In most of these applications the graphene is in contact with the electrolyte and with a supporting substrate. To improve our understanding of the electrical double layer (EDL) at the graphene-electrolyte interfaces without interference from the substrate we used suspended graphene, which also separates the solution from the ambient air.

Graphene is normally assumed to be hydrophobic (241), with a specific affinity for cations due to their interactions with graphene defects and π-orbitals.(242, 243) In recent work an affinity for anions, including OH^-, Cl^-, SO_4^{2-} has been proposed.(244-246) The ions are the main factors in the formation of the EDL, which is strongly influenced by the differential segregation of the electrolyte ions to the interfaces, driven by various physical and chemical forces. One arises from the image charge, where the abrupt change of dielectric properties across the solution-electrode interfaces leads to polarization effects that can be described by image charges outside the solution. This effect however does not lead to differential segregation here, as both cations and ions are affected alike. However, image charge interactions may assist the ion segregation at the interfaces in the presence of other mechanisms that break the symmetry between anions and cations. Another is the segregation of ions out of the solution due to the interplay of enthalpic and entropic forces in ion solvation,(247, 248) and by the different disruption of the H-bonding structure of water near ions in the bulk and interfaces. A third driver is the formation of bonds between ions and the electrode, of covalent, ionic or van der Waals character. Finally, external forces such as applied bias also play a crucial role. The purpose of this work is to obtain a molecular level understanding of these driving forces and the structure of the electric double layer they create. As we show below, the combination of nano-FTIR, Raman spectroscopy, SFVS, and KPFM, together with the use of suspended graphene electrodes provides a unique perspective and insight for such studies (86, 155).

Three salts, Na_2SO_4, $(NH_4)_2SO_4$ and NH_4Cl, were chosen for experiments because of their distinctive adsorption behavior at the air/water interfaces (249). Through Raman measurements we found that the doping of graphene by electrolyte species is very small at bulk concentrations below 10 mM and thus can be ignored. Under open circuit potential and for positive voltages, SO_4^{2-} ions are the dominant species at the interfaces. Spectra acquired at bias voltages on each side of the charge neutral point (CNP), also called point of zero charge, showed an asymmetric change with voltage for H-bonded bulk water molecules and for molecules with dangling OH groups at the interfaces. These changes are also evident in KPFM measurements of the contact potential difference (CPD) between the tip and graphene. Such results are partially consistent with previous observations (234, 246). The dangling O-H stretch vibrational peak of water is largely unaffected by changes in concentration and applied bias, except at voltages below -0.3V, where it shifts to lower frequency and gets buried into the peaks of H-bonded water, implying a change of hydrophilicity at a negative biased graphene electrode.

As shown in Figure 3.2, the graphene electrode can be doped by the ions in the solution near the interfaces. This charge was measured from the G-peak frequency shift in the Raman spectra, as shown in Figure 3.2. As can be seen, for a concentration of 100 mM the doping effect is very clear and reaches a minimum vs bias that corresponds to the charge neutral point (CNP), also known as point of zero charge, between 0.0 and -0.5 V bias, where the charge doping on graphene is near zero. As the salt concentration decreases the doping of graphene decreases also, becoming negligible at 10 mM concentration (red data points) for all bias voltages.

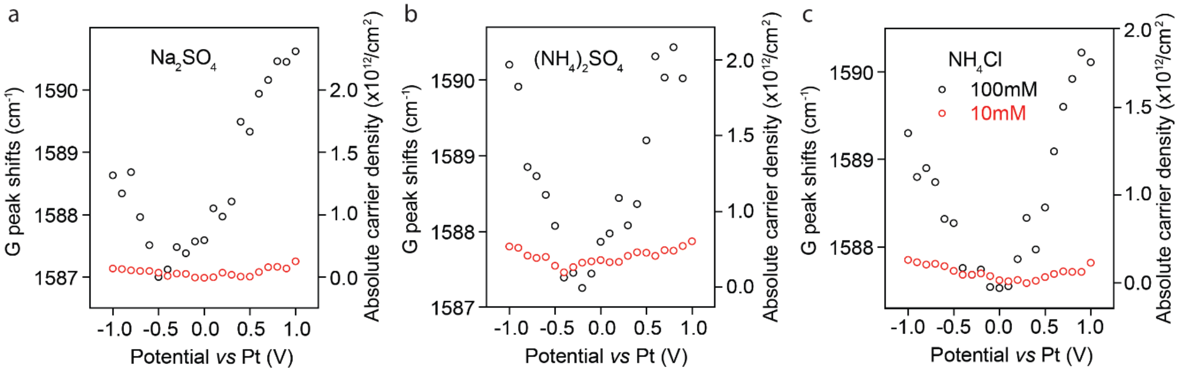

Figure 3.2 Graphene G peak shift (Left Y-axis) in Raman spectroscopy, and absolute carrier density (Right Y-axis), for (**a**) Na_2SO_4, (**b**) $(NH_4)_2SO_4$, and (**c**) NH_4Cl as a function of bias relative to the Pt electrode.

The Na^+ ion and Cl^- ion do not have a characteristic feature in IR spectrum, while NH_4^- and SO_4^{2-} have a strong IR cross section, even higher than water. To better understand the interfacial composition and speciation, we chose a 0.1 M $(NH_4)_2SO_4$ aqueous solution, with the aim to identify the nature of the species formed in the EDL, likely including NH_4^+, solvated SO_4^{2-}, H_2O, etc., with high depth resolution. The cell in this experiment has already been shown previously in Figure 2.11. We first performed ATR-FTIR on the same liquid to establish the IR absorption features of the bulk electrolyte. The result is plotted on the top panel of Figure 3.3 (a). The expected peaks from S-O stretching in SO_4, bending modes of NH_4 and water can be easily detected. The nano-FTIR performed over the suspended graphene covering the electrolyte solution is shown on the bottom panel of the figure for a voltage of zero bias between the graphene and the Pt counter-electrode. As can be seen, peaks of the same species are also observed here, although with very different intensities. This is the result of the different depth sensitivities of the two techniques, where ATR-FTIR reports the bulk structure, while nano-FTIR reports the nm-thick electrolyte layers near the electrode. It is clear that the concentration of solute ions is much higher near the surface, i.e., in the EDL. Other peaks near 1200 cm^{-1} and 1300 cm^{-1} from species, not yet identified, appear as well.

Interestingly, in contrast to the pure solvent case (155), in the 0.1 M $(NH_4)_2SO_4$ case, very clear differences exist between the ATR-FTIR and nano-FTIR spectra. In particular, in the plotted wavenumber range, the largest peak intensity measured for the ATR-FTIR is the water bending mode which dwarfs the sulfate and ammonium peaks, reflecting the low concentration of these species compared to water. However, in the nano-FTIR the sulfate (and ammonium) peak intensity is larger than (similar to) that of the water bending mode. This indicates a much higher concentration of these species, in comparison to the bulk, in the EDL near the graphene electrode. Additionally, two new features at 1207 cm^{-1} and 1286 cm^{-1}, are present that were not detected by ATR-FTIR. Consistent with the increased surface sensitivity to distinguish different relative concentrations in the EDL as compared to the bulk, these peaks are likely from new interfacial species. The capability to directly measure such species opens a significant opportunity for future simulation work, in collaboration with the methodologies described herein, to completely identify the composition of EDLs.

To confirm our above interpretation of the nano-FTIR data, we studied the effect of application of bias between graphene and Pt counter-electrode. The resulting spectra are shown as a color map in Figure 3.3 (b). The bottom spectrum was collected at a bias of 0V, while the top spectrum was collected at a bias of +0.5V relative to the Pt. A substantial change in near-field signal is observed by comparing the two data sets. At positive bias the near-field signals from the sulfate stretching, and the two interfacial species peaks increase, while ammonium and water peaks change only slightly relative to the zero-bias case. The increase in the sulfate region signal upon positive graphene bias is consistent with an electrostatically induced increase in relative anion (sulfate) concentration in the EDL near-graphene.

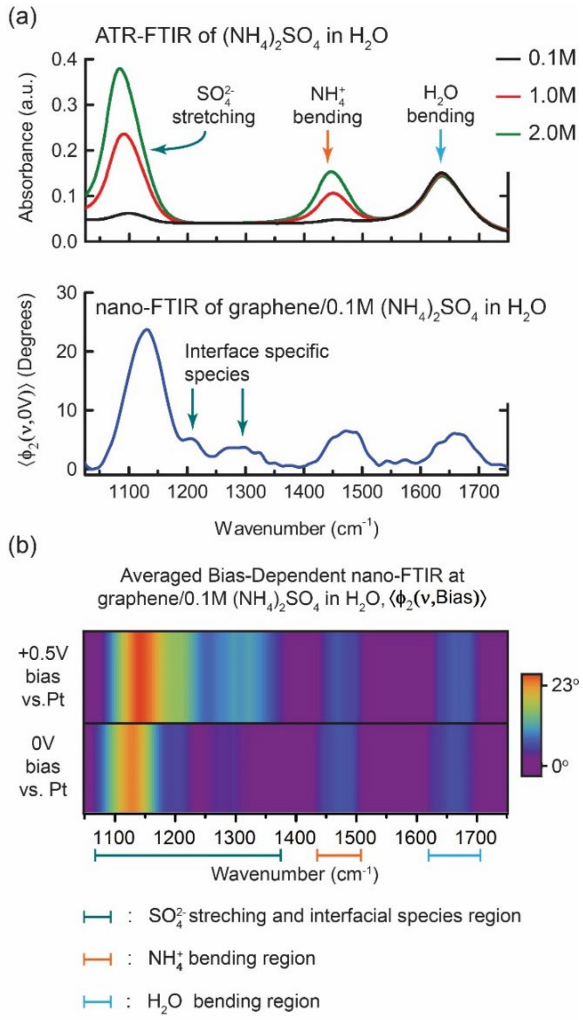

Figure 3.3 Comparison of nano-FTIR and ATR-FTIR spectrum of 0.1M $(NH_4)_2SO_4$ aqueous solution-graphene interfaces. (a) ATR-FTIR spectrum from a drop of $(NH_4)_2SO_4$ aqueous solution (top), and nano-FTIR (bottom) of the same electrolyte at zero applied bias. (b)Bias dependent nano-FTIR displayed as a color map for +0.5V (top) and 0V bias voltages (bottom) vs the Pt counter electrode. Reprinted with permission from ref (155). Copyright 2019 American Chemical Society.

As can been seen in the nano-FTIR experiment, electrochemical bias boosted the differential segregation of cations and anions near the graphene-water interfaces and creates an electric field in the double layer with an intensity that depends on ion concentration and interfacial electrical field strength. The field affects the vibration spectrum of the water molecules and changes the intensity of the peaks in the O-H stretch region, between 3000 and 3600 cm^{-1}. This change is the result of the symmetry rules governing the sum frequency generation (SFG) process, which requires lack of inversion symmetry. At the interfaces there is an intrinsic lack of inversion symmetry manifested by the intense peak around 3620 cm^{-1} due to the dangling O-H stretch vibration mode of the water molecules at the interfaces next to the graphene, which is not affected by salt concentration. However, most of the H-bonded water molecules below the first layer are randomly oriented, i.e., they are symmetric as an ensemble within a volume of wavelength dimensions and therefore cannot generate an SFG output. The orientation ordering is not abrupt but decays rapidly from the interfaces to the bulk interior. As a result, the O-H stretch vibration peaks of the molecules have small intensities.

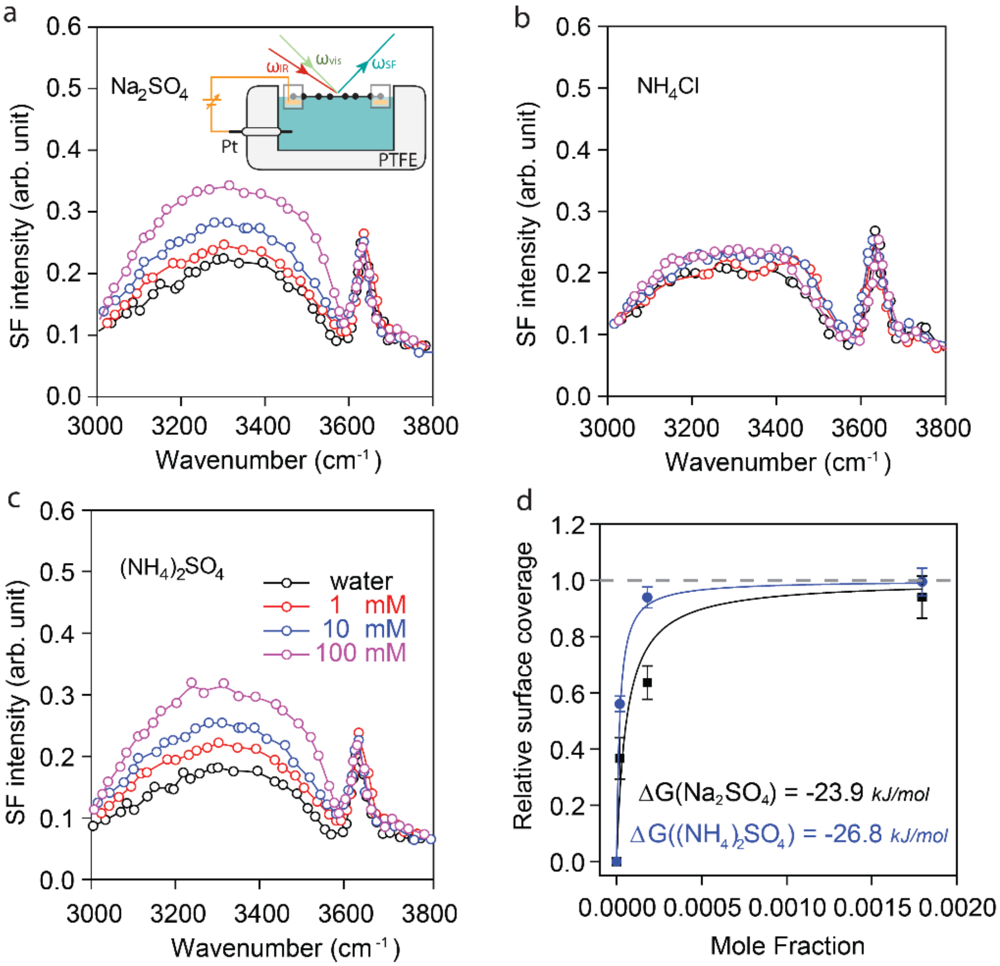

Figure 3.4 SFVS measurement of the vibrational spectrum of water in the O-H stretch region at open circuit potential for: (**a**) Na_2SO_4, (**b**) NH_4Cl and (**c**) $(NH_4)_2SO_4$, for concentrations of 0 mM, (i.e. pure water, black), 1 mM (red), 10 mM (blue), and 100 mM (magenta), respectively. Reprinted with permission from ref (86). Copyright 2022, with permission from Creative Commons. Licensed under CC BY 4.0.

We should note here that the probing depth of SFG is not determined by the penetration depth of the photons, which is macroscopic for the visible, and of μm for the IR, much larger than the Debye length (of the order of 1 nm), or the Gouy-Chapman length (Angstroms). Instead, it is determined by the depth of the illuminated region lacking inversion symmetry. The presence of electric fields tends to orient the molecular dipoles along the field direction, i.e., perpendicular to the interfaces, which break the inversion symmetry and cause the intensity increase observed in the SFVS signal seen in Figure 3.4. The fact that the intensity of the H-bonded water peak increases with the sulfate salts concentration indicates a higher density of ions near the interfaces at OCP.

The intensity of the SFVS peaks is determined by the effective surface nonlinear susceptibility, $\chi_{S,eff}^{(2)}$ (ω), of interfacial water which depends on the electric field E_{DC} following the expression (250) :

$$\chi_{\mathrm{S,eff}}^{(2)}(\omega) = \chi_{\mathrm{S}}^{(2)} + \int_{0^+}^{\infty} \chi_{\mathrm{B}}^{(3)} E_{\mathrm{DC}}(z) \mathrm{e}^{i\Delta k_z z} \mathrm{d}z$$

Where $\chi_S^{(2)}$ denotes the contribution from water molecules right at the interfaces, while the integral describes the contribution from field-induced polarization of water molecules in the diffuse layer. $E_{DC}(z)$ is the distance-dependent field along the surface normal, $\chi_B^{(3)}$ is the third order nonlinear susceptibility of bulk water, and Δk_z the phase mismatch in the SFVS process. The change of $\chi_{S,eff}^{(2)}$ (ω) directly reflects the change of $E_{DC}(z)$ in both magnitude and direction. Details of the surface sensitivity has been shown in the section 2.1.2.

SFVS measurement of the vibrational spectrum of water in the O-H stretch region at open circuit potential for: (**a**) Na_2SO_4, (**b**) NH_4Cl and (**c**) $(NH_4)_2SO_4$, for concentrations of 0 mM, (i.e. pure water, black), 1 mM (red), 10 mM (blue), and 100 mM (magenta), respectively. Figure 3.4 a-c show the SFVS results for the 3 salts, with concentrations ranging from 0 to 100 mM at OCP, which we know is around 0.0 volts relative to the Pt counter electrode. As we see, within measurement error, the spectrum of the graphene/NH_4Cl interfaces shows only a small change with salt concentration (Figure 3.4 b), indicating that NH^{4+} and Cl^- ions do not adsorb or segregate differentially to the interfaces unless, as we show below, they are separated by an externally applied bias. For the two sulfate salts however, the intensity of the H-bonded water peaks in the 3000-3600 cm^{-1} region, increases with salt concentration. From the contact potential measurements shown below, we know that SO_4^{2-} ions are preferentially concentrated near the graphene interfaces at OCP. The surface coverage of sulfate ions can be deduced from the increase in H-bonded peak intensity relative to that of pure water in Figure 3.4 (a) and (c). According to selectivity the intensity is correlated to the electric field produced by the surface charge, i.e., ion concentration, which we used to plot the two adsorption isotherms shown in Figure 3.4 (d). From fitting the data with Langmuir adsorption isotherms, we obtained the free energy of segregated sulfate ions, with values of -23.9 and -26.8 kJ/mol, for Na_2SO_4 and $(NH_4)_2SO_4$, respectively, with the 2.9 kJ/mol variance likely being due to the effect of the different positive ions in the salts.

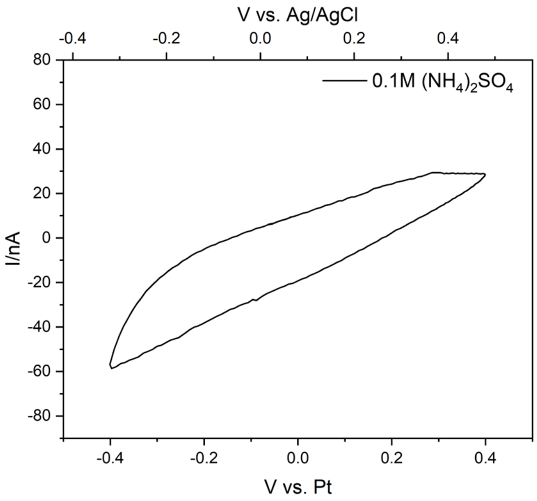

Figure 3.5 Representative Cyclic Voltammetry curve for graphene in contact with 0.1M $(NH_4)_2SO_4$ electrolyte. Other electrolytes will be very similar. Reprinted with permission from ref (86). Copyright 2022, with permission from Creative Commons. Licensed under CC BY 4.0.

The nature of the driving force responsible for the preferential segregation of sulfate anions is not clear at present. Our experimental measurements indicate that it is not of electrostatic origin since there is no doping charge on graphene at OCP, as shown by the Raman results in Figure 3.2. Formation of a specific chemical bonds with graphene is also unlikely given the strongly bound water solvation shell around the anions that prevent close proximity for chemical bonding, and Van der Waals forces between the anions and graphene are expected to be one order of magnitude smaller than the values obtained. Other factors worthy of consideration include contributions from possible sharing of water molecules between sulfate ions close to the graphene interfaces, although this is unlikely in view of the large molarity difference between sulfates (< 1M) and water (55 M). Partial de-solvation that could introduce a local asymmetry in the solvation molecules around the anion and thus increase their contribution to the SFVS is unlikely since the energy of de-solvation of the doubly charged sulfate anions is ~1 eV per molecule (251-253). Finally, distortions of the solvation shell of anions near the graphene may introduce asymmetries in the vibration modes that could increase the intensity of the SFVS peaks. Since the peak intensities were used to calculate the segregation energy, this could conduce to an overestimation of the energy. These are all important questions that point the way for further investigation in theory and experiment.

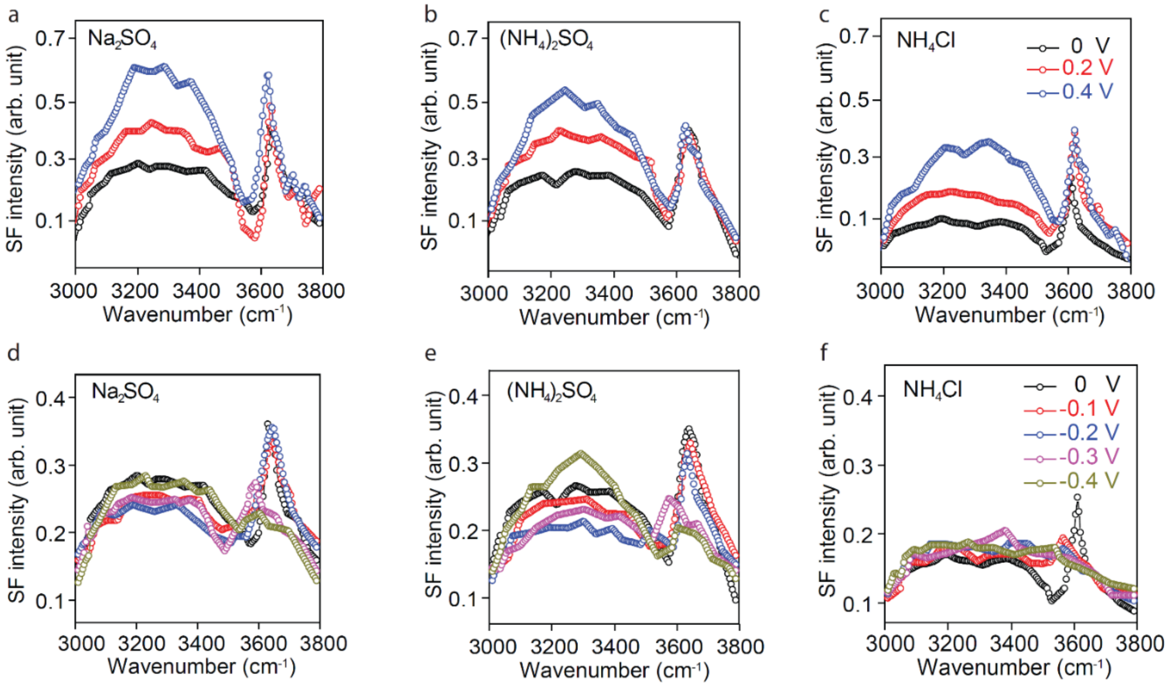

Figure 3.6 SFVS as a function of applied bias for 10 mM solutions of Na_2SO_4, $(NH_4)_2SO_4$, and NH_4Cl. Top (a,b,c) for positive bias (vs Pt): 0.0 V (black), +0.2 V (red) and +0.4 V (blue). Bottom (d,e,f) for negative bias: 0 V (black), -0.1 V (red), -0.2 V (blue), -0.3 V (magenta) and -0.4 V (dark yellow), respectively. Reprinted with permission from ref (86). Copyright 2022, with permission from Creative Commons. Licensed under CC BY 4.0.

In the previous section we showed how increasing the salt concentration at OCP increases the strength of the EDL field due to differential accumulation of ions at the interfaces. Here we present SFVS results showing the changes in interfacial water structure arising from externally applied fields. A cyclic voltammetry test indicated a capacitive behavior, with the absence of chemical reactions (Figure 3.5). The results at 10 mM concentration where graphene doping is negligible, reveal that positive bias (Figure 3.6 a-c) increases the intensity of the H-bonded water peaks for all 3 salts, while negative bias (Figure 3.6 d-f) decreases the peak intensity to a minimum around -0.2 V for Na_2SO_4 and $(NH_4)_2SO_4$ (Figure 3.6 d-e) and 0.0 V for NH_4Cl (Figure 3.6 f), indicating that this is the CNP, in agreement with the results of the Raman experiments in Fig.1. Interestingly, however for negative bias voltages below -0.2 V a moderate increase in the intensity of the H-bonded water peaks is observed, although barely surpassing the intensity observed in pure water. The different response of anions and cations to the applied bias is another interesting result that is not well understood at present and one that calls for additional experiments and theoretical calculations.

Another important result is the behavior of the water molecules nearest to the graphene with a dangling O-H bond peak at 3620 cm^{-1}. In studies of the neat water interfaces with air it is well-known that the dangling O-H stretch peak appears around 3700 cm^{-1} and serves as an indicator of the hydrophobicity of the interfaces (254). The peak does not appear when the interfacial water molecules form H-bonds with a surface, as it occurs on most oxides and hydrophilic interfaces. In our spectra the peak is found around 3620cm^{-1}. This value can be compared with literature values (255) where the dangling OD in H_2O / D_2O mixtures in contact with graphene is redshifted by about $38cm^{-1}$ compared with the air/water interfaces. The H-D mass difference adds a red-shift of around $50cm^{-1}$. In our data the redshift is $80cm^{-1}$, in agreement with the reported values. We have seen that the frequency and intensity of this peak does not change as a function of concentration (Figure 3.4) nor with the application of positive bias (Figure 3.6 a-c). However, it does change at negative bias (Figure 3.6 d-f), decreasing in intensity and red-shifting towards the position of the H-bonded water. This result may indicate that the water molecules next to graphene undergo some orbital hybridization between the dangling H and graphene that causes it to redshift and overlap with the bonded OH region peaks.

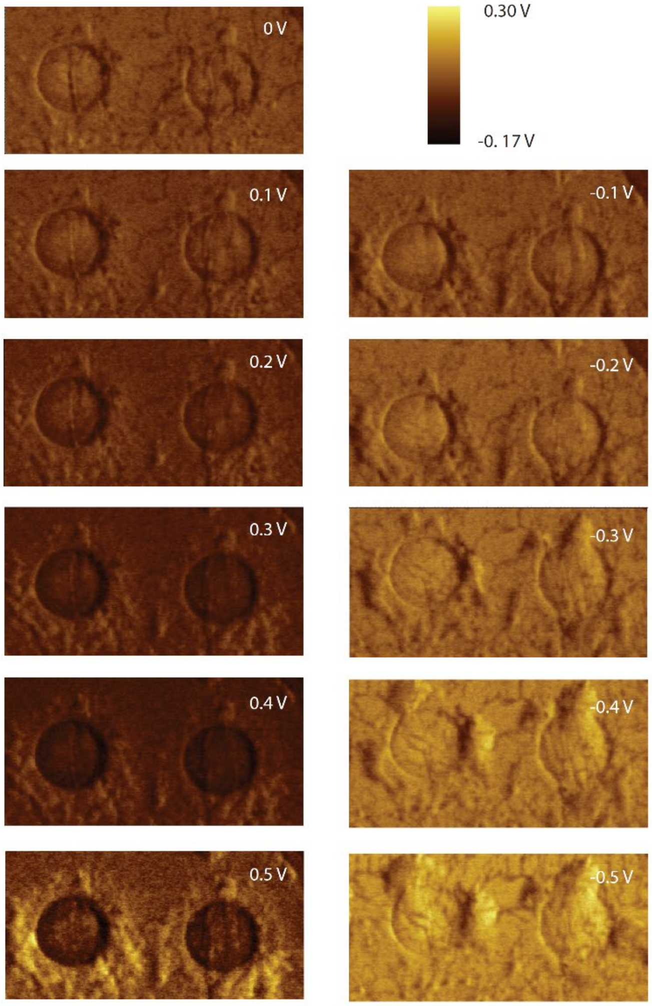

Figure 3.7 Contact Potential Difference (CPD) images from the KPFM measurements on suspended graphene over micrometer diameter holes in a 100 nm thick SiNx membrane covered with a 20 nm gold layer. The bias on the graphene varied from -0.5 V to +0.5 V relative to the Pt counter electrode. Images at -0.4V and +0.4V are used in Fig. 4b of the main text. Reprinted with permission from ref (86). Copyright 2022, with permission from Creative Commons. Licensed under CC BY 4.0.

The differential segregation of ions to the graphene electrode is also manifested in the increasing ionic charge near the graphene calculated from contact potential change measured by KPFM (Figure 3.7). For the KPFM measurements we used a different cell where graphene covered a gold-coated 100 nm thick SiNx membrane (256) perforated with 1 μm diameter holes (Figure 3.8 a). The graphene over the hole regions was suspended and in contact with the solution underneath. Figure 3.7 and Figure 3.8 b shows KPFM images at -0.4 and +0.4 V bias for a 10mM Na_2SO_4 solution. The ionic charge near the graphene electrode that orients the hydrogen bonded water vs bias deduced from the SFVS measurements is shown in the left Y-axis in Figure 3.8 (c). The charge from these ions is also proportional to the CPD value measured by KPFM with the tip over the holes minus the CPD value with the tip in the region between holes (ΔCPD). The difference eliminates possible changes in the tip work function due to contamination. The results are plotted in Figure 3.8 (c) right Y-axis, normalized to match the SFVS charge value at the CNP.

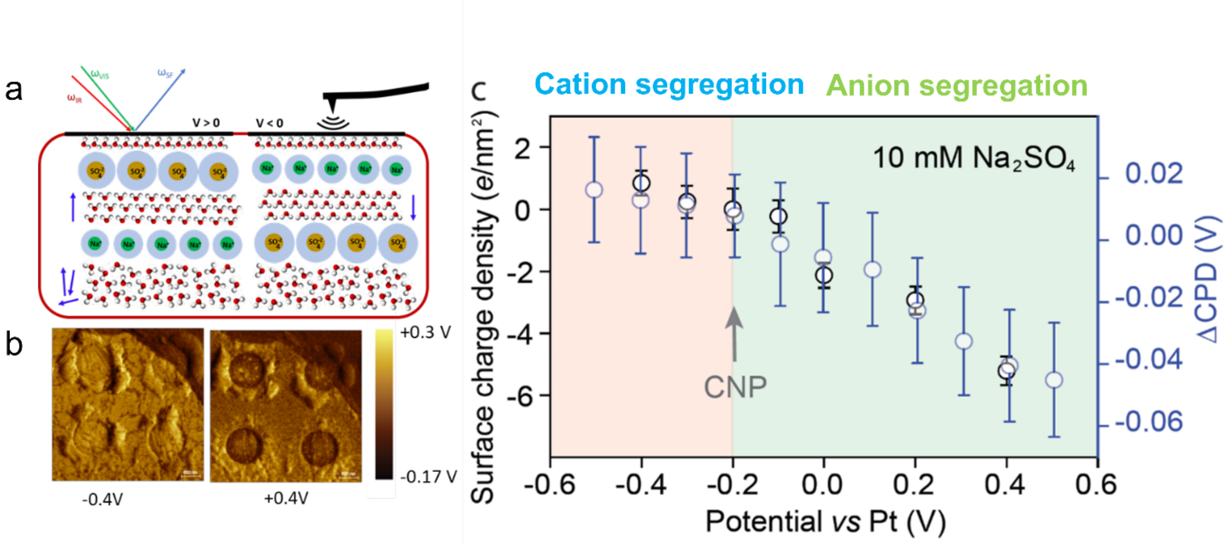

Figure 3.8 (**a**) Schematic of the graphene/electrolyte SFVS and KPFM experiments. (**b**) Contact potential (CPD) images from KPFM obtained by scanning the tip over and across suspended graphene in contact with the electrolyte solution. (**c**) Comparison between the charge density near graphene deduced from the SFVS peak intensity increases of the H-bonded water, left Y-axis and, black circle data points, and the difference in CPD measured by KPFM between suspended graphene and surrounding supported graphene (ΔCPD), which is proportional to the ionic charge near the graphene electrode (right Y-axis). Reprinted with permission from ref (86). Copyright 2022, with permission from Creative Commons. Licensed under CC BY 4.0.

As can be seen the ion charge density curves measured from SFVS and from CPD show the same behavior, with a smaller slope for negative biases (pink background), than for positive biases (green background). Such asymmetric behavior was also observed on supported graphene electrode/pure water interfaces (87). The nonlinear response of the water orientation to different gating potentials and ion species, indicates again that the Stern-Gouy Chapman model does not describe properly the EDL at the microscopic scale (257) and that more advanced EDL models that include effects of solvent dipoles (200, 258), ion solvation structure (158), ion finite size (201) and non-electrostatic forces between molecular species and electrode surfaces (211, 259) should be used. Since the alignment of the water dipoles by the electric field is the result of competition between the torque on the water molecules by the field–dipole interaction and the hydrogen bonding network near the interfaces the electric field E_{DC}, its dependence on distance to the interfaces, solute type, and ion species, should be considered more carefully and needs correction when deducing the surface change density at the interfaces. However, we believe that the model still provides a reasonable approximation of the field created by the segregated ions, as shown by the good agreement between the charge concentration measured from the increase in SFSV peak intensity and the values obtained using the contact potential difference produced on the graphene as measured by the Pt tip located outside the solution in the KPFM experiments.

In summary, through the combined use of nano-FTIR, Raman spectroscopy, SFVS and KPFM, we determined the effects of the differential ion segregation at the graphene-electrolyte interfaces in three salt solutions, Na_2SO_4, $(NH_4)_2SO_4$, and NH_4Cl, and their effect in creating a double layer structure that orients the interfacial water. The first water layer in contact with graphene has dangling O-H bond that points to the graphene and remains unchanged both with salt concentration and with increasing positive potentials but undergoes a chemical interaction with graphene at negative values that decreases its peak intensity and redshifts its frequency. We showed that a preferential anion-accumulation at the interfaces is driven by segregation from the solution bulk, which increased with ion concentration. We have shown that the differential segregation at OPC is not driven by electrostatic effects nor by formation of specific chemical bonds, which is impeded by the large energy required to de-solvate sulfate anions. While the origin of this phenomenon remains unclear, we speculate that it could be due to reorganization of water in the solvation shell that breaks the symmetry of the bonded O-H stretch modes. This therefore requires further experimental or theoretical study of the structure of the EDL. We showed also how externally applied fields further enhance the segregation effects and lead to an increased orientation of interfacial water. The asymmetric change of the field-induced H-bonded water orientation was proved by both SFVS and KPFM and brings to the fore the need for further studies, particularly theory to better understand it. Finally, we found that the dangling O-H peak of the water molecules next to the graphene remained largely unchanged as a function of concentration and also under positive bias, but redshifts and decreases in intensity at negative bias, pointing to orbital hybridization between dangling H and graphene.

Case II: anatase-solution interfaces

Titanium dioxide is one of the most common minerals on earth. Owing to its high dielectric constant, superhydrophilicity and unique band structure, TiO_2 has also been widely used for photocatalytic water splitting, self-cleaning surfaces, and corrosion-resistant coatings. For each of these applications, the interaction between TiO_2 and water is crucial (4, 260).

Substantial efforts have been made to understand the basic process and reactions taking place on the TiO_2–water interfaces. However, many fundamental and critical questions remain unclear, which limit our understanding of the TiO_2 water interfaces (214). For instance, does water dissociate on TiO_2 surfaces? What is the structure of the few water layers near TiO_2 and how would this structure be altered on different TiO_2 phases? Does TiO_2 form a hydration layer (Ti-O-H) in contact with water and if so, what fraction of the surface is hydroxylated? How do the surface oxygen vacancies in TiO_2 affect the dissociative adsorption of water molecules on the surface? These long-lasting questions necessitate an atomic/molecular understanding of the structure and properties TiO_2 water interfaces under realistic condition (e.g., in the presence of bulk water/aqueous solutions, under electric field, or photon illumination).

Progress in understanding these questions have been achieved using different experimental and theoretical tools, starting from the model system of water molecules absorption on TiO_2 single crystal (261, 262), to more realistic case of TiO_2 film in contact to bulk electrolyte (263, 264). However, most of the research focus on water layer structure only, with assumption that the chemical state of the TiO_2 surface remains the same, which contradicts the fact of strong chemical interaction between TiO_2 and water (265, 266). Besides, these experiments remain distinct and mostly indirect, therefore bringing more inaccuracy or even controversy to these questions, among which the most famous one is whether water dissociates on TiO_2 surface. A direct spectroscopic tool probing both the oxide and water layer structure is critical for a comprehensive study of TiO_2–water interfaces.

In this section we are combining soft XANES with electrochemical flow cells to probe the TiO_2/water and TiO_2/electrolyte interfaces. The results provide the first direct (X-ray spectroscopic) proof of the existence of ice-like water bilayer at TiO_2/water interfaces and also shows the solvation/de-solvation of electrolyte ions near the TiO_2 as the function of bias, concentration and bias (23, 181).

The electrochemical flow cell (Figure 3.9) used in this study was made of PEEK (polyether ether ketone, a highly electrically insulating material), sealed by an X-ray-transparent 100-nm-thick SiN_x membrane (267). Onto this membrane, a layered structure comprising TiO_2/Au/Cr was deposited with respective thicknesses of 6.6/10/2 nm, with TiO_2 facing the water inside the cell. The TiO_2 was deposited using plasma-enhanced atomic layer deposition after Au and Cr were deposited using thermal evaporation. XAS revealed that the structure of the TiO_2 is that of the anatase phase. As reference, the X-ray absorption spectra for the same TiO_2/Au/Cr stack on SiN_x were also measured under ultrahigh vacuum (UHV), using total electron yield via the sample drain current.

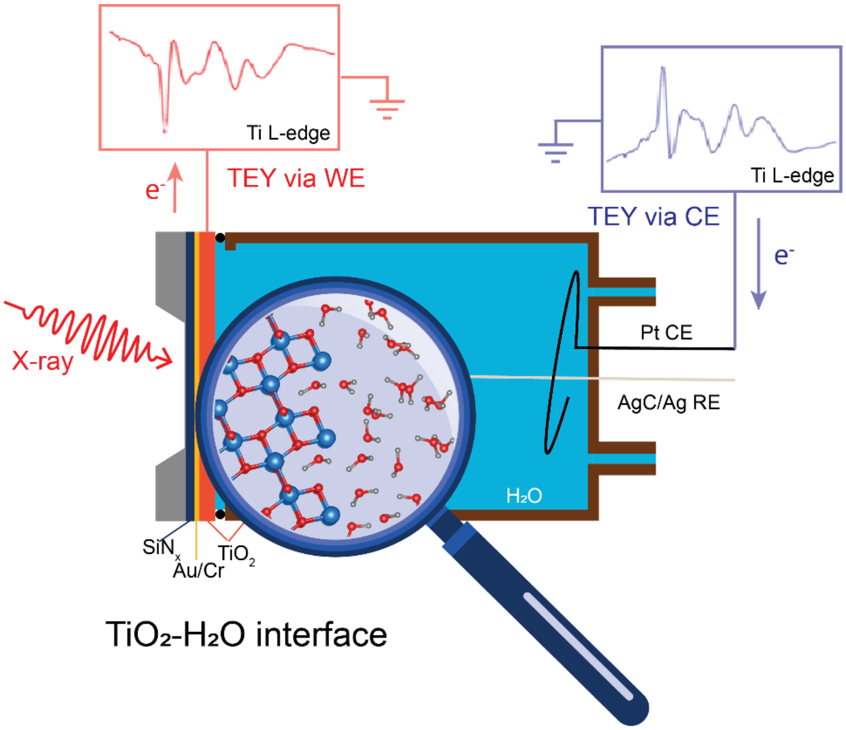

Figure 3.9 Illustration of the XANES experiments with electrochemical flow cell. Reprinted with permission from ref (23). Copyright 2021, with permission from Creative Commons. Licensed under CC BY 4.0.

Drain currents were measured at the counter electrode with the working electrode grounded (Figure 3.10 a), or at the working electrode with the counter electrode grounded (Figure 3.10 b). The choice of electrode where the current is measured determines the name used, i.e. “total ion yield” if measured at the counter electrode (Figure 3.10 a) (69, 70, 268, 269) and “total electron yield” if measured at the sample/working electrode (Figure 3.10 b) (65, 66, 68, 176). To avoid confusion, here we refer them as counter-electrode drain current (Figure 3.10 a) and working-electrode drain current (Figure 3.10 b). Note that the total electron yields as depicted in Figure 3.10 (b) is different from the “one-electrode” total electron yield in which, by keeping the counter electrode floating, no signal from inside the cell could be measured.

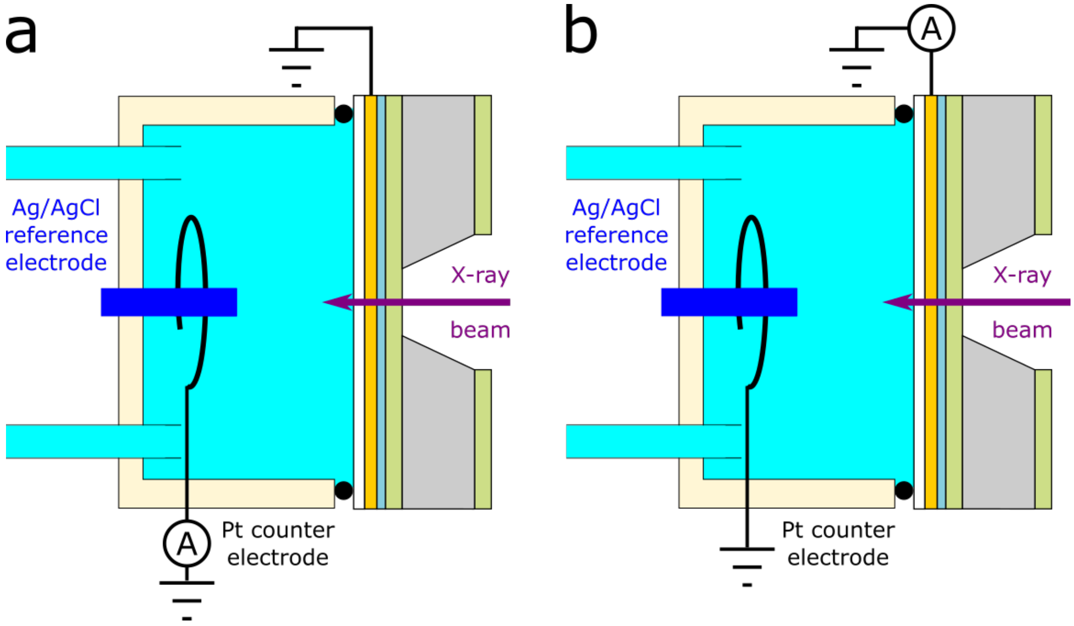

Figure 3.10 Electrochemical flow cell, filled with pure H_2O, showing the sample (working electrode) comprising three layers: TiO_2 (6.6 nm, white) facing the electrolyte, Au (10 nm, yellow), and Cr (2 nm, blue) on a free-standing, X-ray-transparent SiN_x film (100 nm thick, 1 mm^2, green), supported on a Si frame (gray). Drain currents are measured at the counter electrode (a) or at the working electrode (b), each with the other electrode grounded. Reprinted with permission from ref (23). Copyright 2021, with permission from Creative Commons. Licensed under CC BY 4.0.

Comparison of the counter-electrode and working-electrode drain currents shows that they are inverted relative to each other but otherwise practically identical (Figure 3.10 a). This is emphasized by the near complete overlap between the inverted working-electrode drain current and the counter-electrode drain current (Figure 3.10 b), clearly showing that both signals contain the same information.

Spectroscopically, the Ti L-edge spectra (Figure 3.11) contain all the features typically observed for TiO_2, which are ascribed to Ti $2p \rightarrow 3d$ transitions. The L edge is split into two components because of spin-orbit coupling. These two are labeled L_3 and L_2 and related to excitation from Ti $2p_{3/2}$ and $2p_{1/2}$, respectively. Both components are further divided into two peaks, originating in the crystal-field splitting of the Ti $3d$ band and assigned to Ti $2p \rightarrow t_{2g}$ and $2p \rightarrow e_g$. Finally, the L_3-e_g peak comprises two closely spaced maxima with their relative intensity depending on, among other things, the TiO_2 crystal structure (270, 271). The origin for the L_3-e_g splitting is debated: short-scale distortions in the bonding in the TiO_6 (270, 271) range distortions between octahedron (63) and dynamic coupling of electronic and vibrational states have been proposed (272, 273).

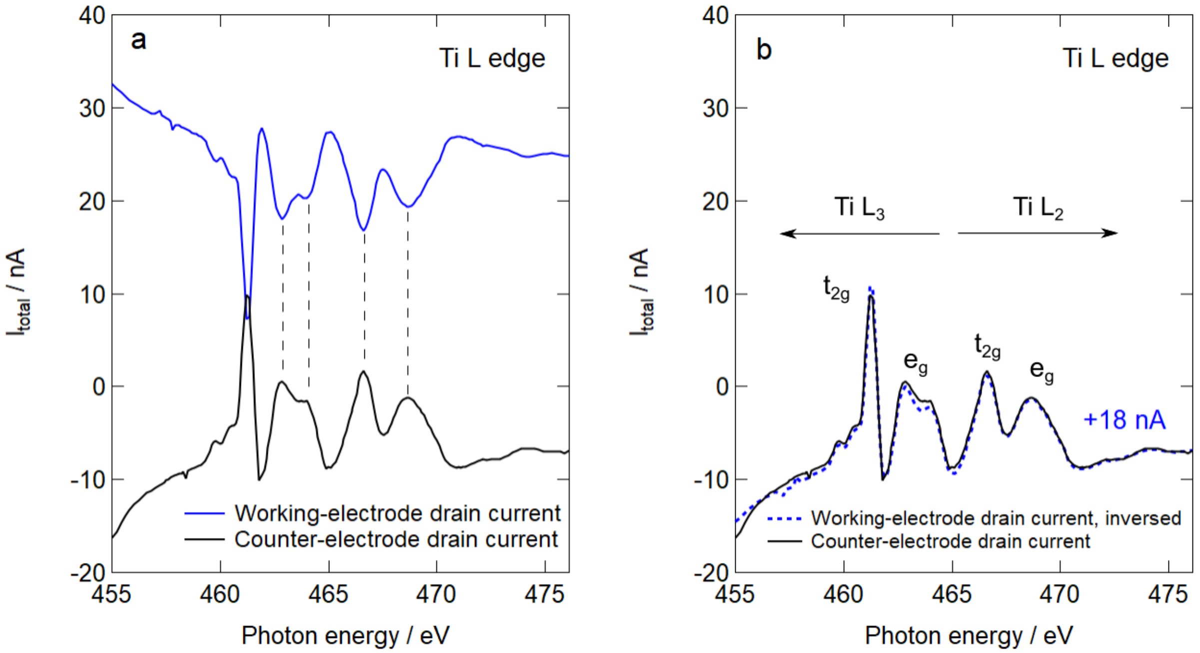

Figure 3.11 Ti L-edge spectra of TiO_2 in deionized water (a), measured via the counter-electrode (black) or via the working-electrode drain current (blue). Similarities are highlighted by inverting and overlaying the working-electrode drain current (b). Reprinted with permission from ref (23). Copyright 2021, with permission from Creative Commons. Licensed under CC BY 4.0.

Both the counter and working-electrode drain currents originate in X-ray absorption at the working electrode-liquid interfaces because Ti is only present in the 6.6-nm-thick TiO_2 film in the working electrode. The TiO_2 film was stable for hours in the liquid under irradiation by the X-ray beam, indicating negligible leaching of Ti and/or redeposition on the counter electrode (a Pt wire). Furthermore, the soft X-rays are fully absorbed by the liquid and cannot reach the counter electrode (transmission of X-rays up to 1 keV through 0.15 mm H_2O is less than a 10^{-6}) (274), and the typical electrode separation is several millimeter).

It may seem counter-intuitive that the spectrum of the H_2O-TiO_2 interfaces can be measured via the counter-electrode drain current, given the short inelastic mean free path of electrons in liquids, around 1–2 nanometers (75). The mechanism of the charge transfer from working to counter electrode is not yet clearly understood. However, a crucial step is the emission of energetic Auger and secondary electrons from the working electrode into the liquid, ionizing the liquid, and leading to a multitude of positive ions and secondary electrons. As the electrons lose energy, they may recombine with cations, get attached to neutral molecules creating anions, or become solvated electrons. In this thermalization process, a cascade of charged species is generated, possibly with longer lifetimes and diffusion lengths. The transport pathway of these species is interesting and deserves careful investigation, likely needing additional experiments (73-76, 275-277). This is however outside of the goals of this work.

The observation that both drain currents carry the same signal is not unexpected because the cell walls are electrically insulated. To maintain charge neutrality, all electrons flowing into the liquid cell via one electrode must be balanced by the same number of electrons leaving the cell via the other electrode. The spectra are inverted because they represent the same current measured in opposite directions. In Figure 3.11, Ti L-edge spectra of TiO_2 in deionized water (a), measured via the counter-electrode (black) or via the working-electrode drain current (blue). Similarities are highlighted by inverting and overlaying the working-electrode drain current (b)., the current was such that electrons entered the cell via the counter electrode and left via the working electrode. Even though X-ray absorption initially leads to the emission of Auger (and secondary) electrons from the working electrode into the liquid, more secondary electrons generated in the liquid leave the cell via the working electrode. Because both drain currents are essentially the same signal, distinction between "total ion yield and "total electron yield" is not very meaningful. It is also confusing because total ion yield XAS is employed in liquid-jet experiments or in ionization chambers, where the primary ionized atom can actually be measured (278, 279). The solid-liquid XAS measurements resemble more the conversion electron yield detection, which has been established for XAS on the solid-gas interfaces (280).

The conclusion that both drain currents are interfaces sensitive diametrically opposes the interpretation presented by Schön *et al.*, which was based on the O K edge spectra measured from self-assembled monolayers, $HOOC–(CH_2)_n–SH$ with n=3,11, and 16, on Au (69, 70). The main argument in favor of the bulk sensitivity of the counter-electrode drain current was the observation that the signal from the COOH group at 532 eV was clearly visible when the cell was filled with CH_3CN but not when it was filled with H_2O. In the latter case, the spectral features of $H_2O(l)$ dominated the O K edge spectra. Based on the current findings, we speculate that the self-assembled monolayers were not stable in the aqueous environment under X-ray irradiation. In the current work, spectra obtained from both the Ti L *and* O K edge (see below) clearly show the interfaces sensitivity of both the drain currents. Furthermore, we anticipate that TiO_2 suffers less from beam-induced artifacts. Possible reduction of TiO_2 in the beam would have been obvious difference from the spectra and was not observed (281). Furthermore, we believe that the signal intensity is strongly correlated with the potential drop across the interfaces, which in term is determined by the potential difference between electrodes, applied and/or contact potential, electrolyte concentrations, *etc.* Deionized water is in this respect not an ideal medium, as small amounts of absorbed CO_2, increasing over time, have relatively large effects on the ion concentration.

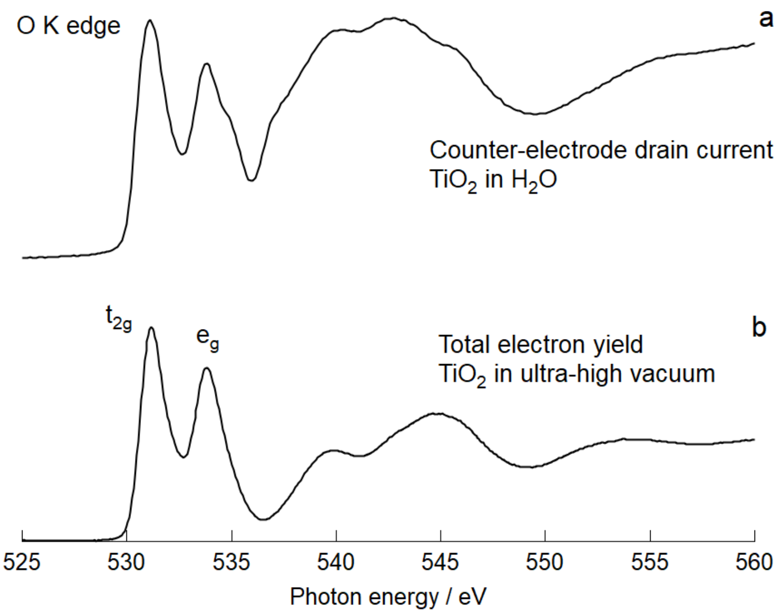

Figure 3.12 O K-edge spectra of (a) TiO_2 in deionized water measured via the counter-electrode drain current (Figure 3.10 a) and of (b) TiO_2 under UHV measured via the conventional total electron yield. Reprinted with permission from ref (23). Copyright 2021, with permission from Creative Commons. Licensed under CC BY 4.0.

Focusing on the O K-edge spectrum of the TiO_2-H_2O system (Figure 3.12 O K-edge spectra of (a) TiO_2 in deionized water measured via the counter-electrode drain current (Figure 3.12 a) and of (b) TiO_2 under UHV measured via the conventional total electron yield.), the spectral features of TiO_2 can be clearly recognized between 530 and 535 eV, partially overlapping with features from the oxygen of H_2O above approximately 535 eV. Comparing the TiO_2-H_2O spectrum with that obtained from TiO_2 alone, *i.e.,* in UHV (Figure 3.12 b), shows the H_2O contribution to the TiO_2-H_2O spectrum is modest, further confirming the surface sensitivity of the spectra collected via the counter-electrode drain current. The bulk-sensitive spectra recorded in via partial fluorescence yield (Figure 3.13) are completely different for these two cases. For the TiO_2-H_2O measurement, the fluorescence showed no obvious sign of TiO_2 and was dominated by $H_2O(l)$.

Both the spectra for TiO_2-H_2O and TiO_2-UHV have two sharp peaks assigned to O $1s \rightarrow t_{2g}$ and O $1s \rightarrow e_g$ transitions in TiO_2 (282, 283). These transitions are dipole-allowed through the hybridization of the O $2p$ and Ti $3d$ orbitals. The broad features above 535 are assigned to transitions to higher unoccupied orbital, O $1s \rightarrow a_{1g}$ and O $1s \rightarrow t_{1u}$ (283). Some differences between the TiO_2-H_2O and TiO_2-UHV spectra are visible, such as a weak shoulder around 535 eV, an increase in edge intensity starting at 537 eV, and a broad peak around 542.7eV (Figure 3.12).

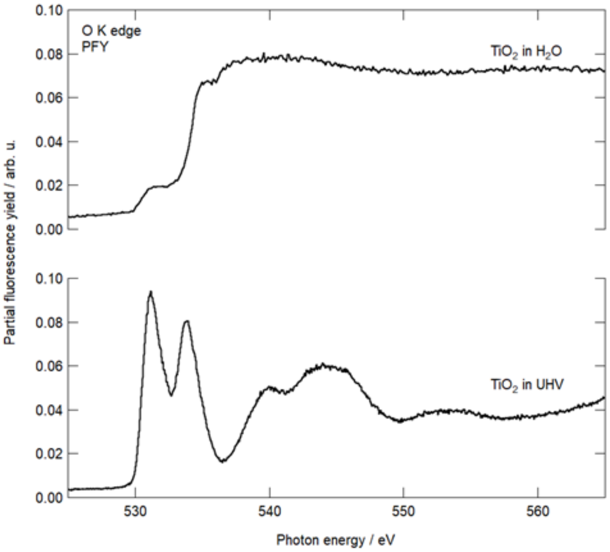

Figure 3.13 O-K-edge spectra obtained via partial fluorescence yield of the TiO_2 in contact with bulk H_2O(l), top, and in ultra-high vacuum (UHV), bottom. Reprinted with permission from ref (23). Copyright 2021, with permission from Creative Commons. Licensed under CC BY 4.0.

Subtraction of the TiO_2-UHV spectrum from that of TiO_2-H_2O unveils the spectral contribution of H_2O (Figure 3.14 black curve,). The difference spectrum resembles ice on various surfaces.[25] Specifically, the similarity with ice at 268 K is remarkable (red curve, Figure 3.14). At this temperature, the of the ice is premelted and covered by a *ca.* 1-nm-thick layer of liquid water (284). Interestingly, *ab initio* molecular dynamics by Selloni *et al.*, predict that water on anatase TiO_2 forms a stable bilayer of molecules with ice-like dynamics (26, 264, 266). The difference spectrum reveals additional features, between 529.5 and 533 eV, which cannot be attributed to H_2O, possibly artefacts from the subtraction method, contaminants in the TiO_2 that are unstable under the UHV conditions of Figure 3.14 (b) or hinting at other unique features of the TiO_2-H_2O interfaces.

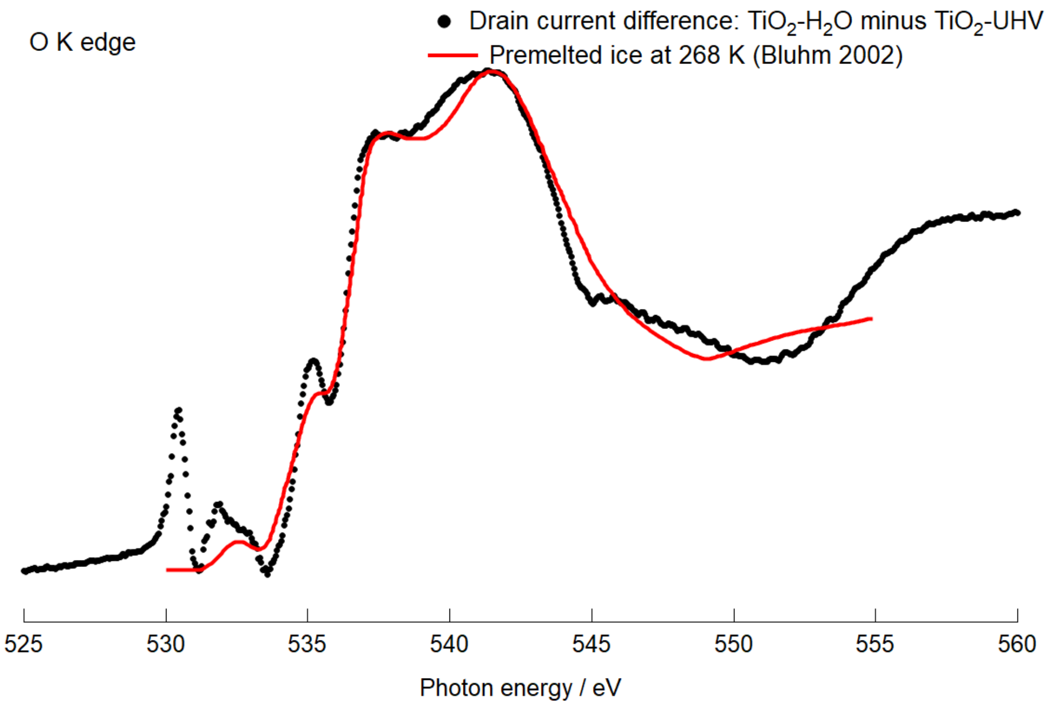

Figure 3.14 Difference spectrum (black) obtained by subtracting the O K edge spectrum of TiO_2 in UHV (**Figure 3**b) from that of TiO_2 in H_2O (**Figure 3**a), after scaling to match the O 1*s*→t_{2g} peak intensity (531.1 eV). The difference spectrum has been corrected for X-ray absorption by the SiN_x. The difference spectrum closely resembles the spectrum (red) of ice during the melting transition (reproduced with permission from Ref (285).). Reprinted with permission from ref (23). Copyright 2021, with permission from Creative Commons. Licensed under CC BY 4.0.

Comparing the relative contributions of TiO_2 and H_2O shows that TiO_2 is the major contributor to the O K-edge spectrum of TiO_2-H_2O. The H_2O contribution in the TiO_2-H_2O spectrum is about 0.4, determined by dividing the absorption step rise between 525 and 550 eV of the difference spectrum (mostly H_2O contribution) by that of the TiO_2-H_2O spectrum (Figure 3.13 b and a, respectively). A similar number was obtained by dividing the area of the difference spectrum between 534.4 eV and 550 eV by the area of the TiO_2-H_2O spectrum (525–550 eV). The latter assume that the intensity in the difference spectrum above 533.4 eV stems from H_2O. Fitting the difference spectrum with a linear combination of the spectra for liquid water and ice at 234 K from Bluhm *et al.*, showed that the contributions of $H_2O(l)$ and $H_2O(s)$ were very close to 1:1 (285).

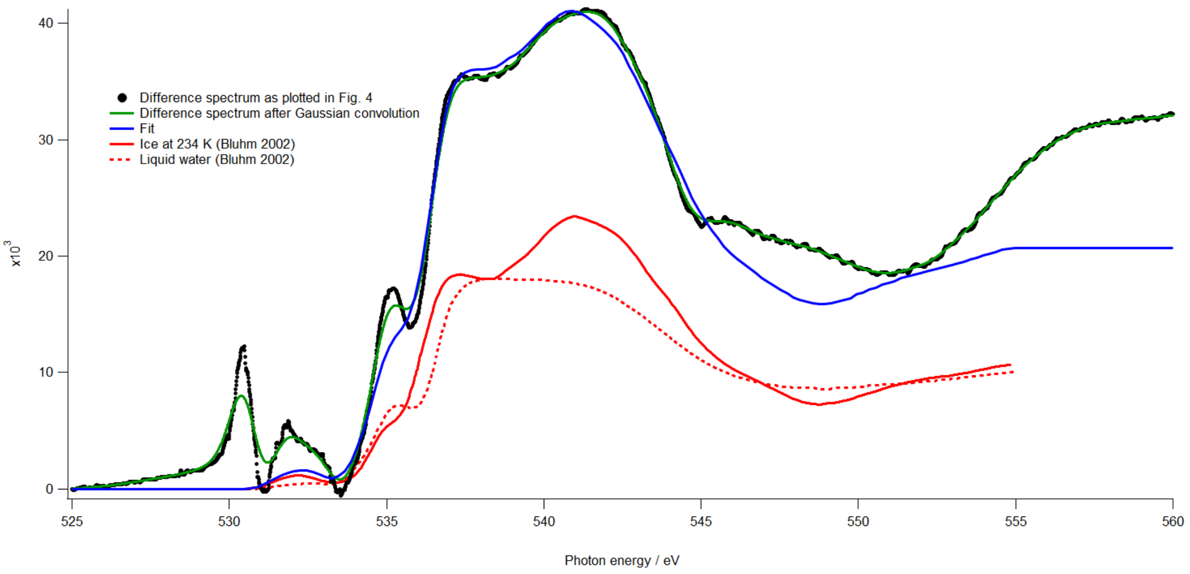

Figure 3.15 Fitting the difference spectrum (Figure 3.14) by a linear combination of the spectra for H_2O(l) and H_2O(s). Copyright 2021, with permission from Creative Commons. Licensed under CC BY 4.0.

A quantification of the interfaces sensitivity and a precise determination of the probed H_2O(l) layer is complex and is likely to depend on the relative amplification of the signal by the generation of secondary electrons in the solid and liquid phases. The amplification is expected to depend on the local potential drop, local electrolyte concentrations, *etc*. Based on the similarities between the O K edge spectra of TiO_2–H_2O and TiO_2–UHV, an upper estimate of the interfaces sensitivity of a few nanometers can be established with relative certainty. This can be further narrowed down because molecular dynamics simulations predicts that the thickness of the ice-like interfacial water is 2 layers (263). Using that information in combination with the fit results (Figure 3.15) leads to an interfaces region probed of about 4 layers of water, or *ca.* 1 nm. These values should be treated with caution, and more experiments were carefully constructed samples are needed to support this estimation, which are the focus of current efforts.

Conclusion

In a summary the surface-sensitive microscopic/spectroscopic studies of graphene-electrolyte and anatase-electrolyte are presented here as model system for electrical double layers. In graphene case, it is clear that each individual technique only probes partial information of the interfaces and is not sufficient to provide a comprehensive molecular picture of the interfaces. The combination of different techniques, however, provides the structure of EDL from many aspects. For instance, without Raman it is very challenging to tell what leads to the contrast of KPFM images under bias, whether it is the ion segregation or the doping charges on graphene, while the asymmetric behavior is “loose and weak” without KPFM.

However, some drawbacks further limit these studies. From the case of anatase-electrolyte interfaces we realized the power of the DFT calculation of the solid-liquid interfaces, but the system of solid-liquid interfaces is way too large for a conventional DFT (e.g., to simulate the interfaces between graphene and 0.1M Na_2SO_4 and include the ion-ion interaction, at least 30 ions and 5500 water molecules need to be included) so that it is both time and effort consuming. Even with the optimized DFT model the connection between DFT structure and spectrum is still weak. The simulation of SFG, KPFM, XANES are still underdeveloped or again time/effort consuming. A direct connection such as the digital twin method (286), could possibly bridge the DFT calculation and the experimental observations and hold the promise of future research direction.

In the experimental side, contamination and reproducibility are the major concerns. How clean the sample, the liquid, or even the air/vacuum should be? Unlike the LT- UHV studies, the measurement of liquid nearly always comes with some factors that are hard to control, such as the impurities on the graphene, the ions or carbon dioxide dissolved in the liquid, or even the temperature fluctuations. The noise is also affected by the experimental setup, the vibrations in the building and even the number of people in the room. These factors bring many side-effects, affecting the experimental observations and lowering the reproducibility. In many cases for the above-mentioned projects, the experiments were repeated several times, and both the trend and the absolute values were compared to ensure the reported value and figures represent the typical experiment results.

The systems discussed here are mostly model systems. They are away from realistic conditions much so that there is a huge material gap. It is anticipated here that in the future more realistic cases, such as EDL structure on Cu for CO_2 reduction will be investigated thoroughly.

Chapter 4 Spectroscopic imaging of soft material at interfaces

Abstract

Soft materials, especially polymers and biopolymers, are basically made of organic building blocks and show superior performance compared to inorganic materials in many applications. In industry soft materials are widely used in semiconductor manufacturing, in biomedical engineering, and in energy storage and conversion. *Operando* nano scale characterization of soft materials, however, has problems related to the damage caused by the x-ray and electron probes used for spectroscopic and structural studies of organic materials. For example, the X-ray and electron probes ionize the organic molecules into radicals and ions with unsaturated bonds, which then dissociate or crosslink to convert into new species. In this chapter nano-FTIR was utilized to probe the nano scale chemical properties of soft material nondestructively in their native environments. The photon energy of IR is usually on the order of 100 meV, much lower than that of the X-ray photons and electrons used in electron microscopy, which eliminates the radiation damage. We will show two results of studies of soft materials, one is an investigation of photoresists, used industrially in the production of microelectronic chips, described in Case I. The second case illustrates the use of a combination of liquid cell and nano-FTIR, to study the dynamics of protein assembly as well as nanoparticles and their organic ligands in electrochemistry under realistic conditions.

Case I: Interfaces in metal-oxide photoresists

The first extreme case is that of metal oxide photoresists, which is a promising candidate for Extreme Ultra-Violet (EUV) lithography. Figure 4.1 shows the first proof-of-concept experiment of the use of nano-FTIR to characterize the chemical gradient at tens of nanometer length scale on a proprietary dry-deposited metal-containing EUV resist (287) of Lam Research. Modulation of chemical composition was observed on line/space patterns, which informed the local chemical transformation induced by exposure. The results demonstrate the capability of this spectro-microscopy technique to provide chemical information on EUV resists at sub-micrometer length scale. Improvement is needed to further reduce the spatial resolution and enable meaningful resist characterization at relevant length scales.

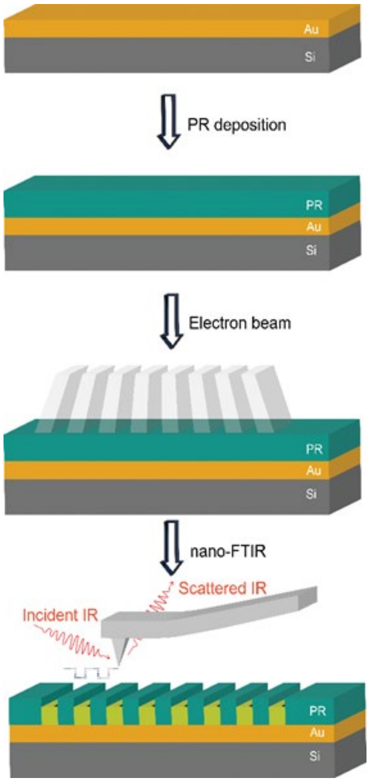

Figure 4.1 Schematic workflow from photoresist deposition to nano-FTIR measurement. Reprinted from ref (288). Copyright 2022 Society of Photo-Optical Instrumentation Engineers (SPIE).

ATR-FTIR spectra were collected on large areas of unexposed and fully exposed resist films to reveal the most significant spectral difference before and after exposure, as depicted in blue and brown traces in Figure 4.2 , respectively. The metal oxide resist used in this study is sensitive to a variety of excitations, including EUV and UV light as well as e-beam. There may be some detailed difference in reaction mechanism in terms of how the resist materials change under different forms of excitation, but the composition of the fully exposed film is the same, which is characterized by the removal of alkyl group as well as crosslinking of metal oxide clusters (289). Here, a resist film over-exposed under a UV lamp was used as the “fully exposed” film, representing the extreme case where all bleachable motifs are consumed.

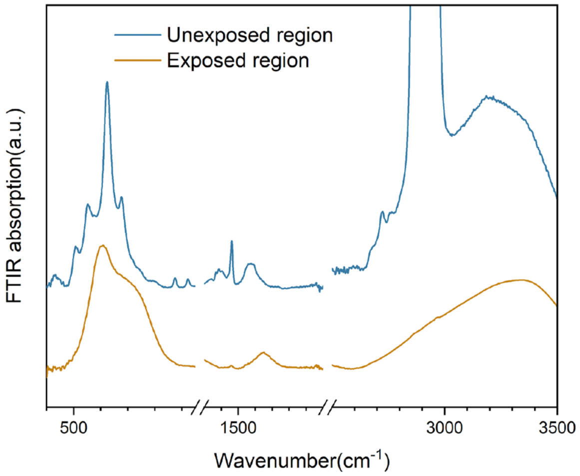

Figure 4.2 ATR-FTIR spectra of unexposed (blue trace) and fully exposed (brown trace) photoresist film. Reprinted from ref (288). Copyright 2022 Society of Photo-Optical Instrumentation Engineers (SPIE).

ATR-FTIR of unexposed and exposed resist films showed three wavenumber regions with the most noticeable spectral changes: 1) 2800 - 3000cm^{-1}; 2) 1400 - 1700cm^{-1}; 3) 450 - 850cm^{-1}. Peaks in regions 1 and 2 can be attributed to C-H stretch and scissor modes, respectively (290, 291). The disappearance of peaks in these two regions indicates complete consumption of the C_xH_y component in the resist film when over-exposed. In region 3, unexposed film exhibited distinctive fingerprint features, indicating metal-containing nanoclusters with well-defined size and/or geometry. After exposure, these fingerprints evolved into broadened hump with decreased intensity, characteristic of amorphous metal oxides.

The spectral difference observed in unexposed and exposed resist films suggests that the most informative features that we should monitor in the Nano-FTIR characterizations are those related to C-H bonds and metal-oxygen (M-O) bonds. Since in most cases the detection efficiency in nano-FTIR experiment is optimum around 1000 cm^{-1} -1600cm^{-1} with the MCT detector efficiency decaying rapidly in the high wavenumber side (136), the C-H scissoring peak at 1460cm^{-1}, instead of the most intense C-H stretch peaks at 2900cm^{-1}, were selected in the subsequent Nano-FTIR experiments.

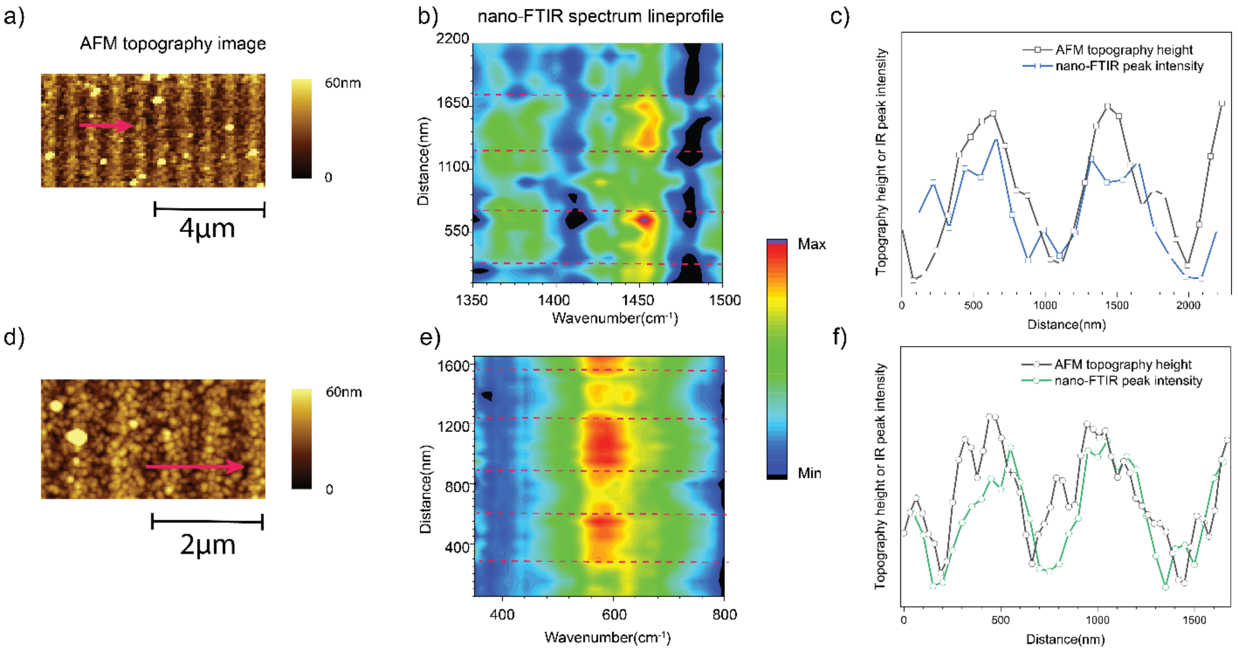

Figure 4.3 (a, d) Images of AFM topography over the line/space pattern on the same resist film in different measurements. The scan size is 8μm×4μm for (a) and 4μm×2μm for (d), respectively. The grainy morphology comes from the grains of the thermally evaporated Au films underneath. The red arrows in (a) and (d) mark the position where the subsequent line scan was acquired. (b, e) Corresponding color map representations of the nano-FTIR spectral intensities (arbitrary units in the color scale) of resist film across the line/space patterns in different wavenumber ranges. Red dashed lines in both color maps represent roughly the boundary position between exposed and unexposed areas. (c) The C-H scissoring peak intensity integrated from 1433 to 1467 cm-1 in the line scan shown in (b), overlaid on the AFM topography height profile extracted from (a). (f) The M-O peak intensity integrated from 440 to 760 cm-1 in the line scan shown in (e), overlaid on the AFM topography height profile extracted from (d). Reprinted from ref (288). Copyright 2022 Society of Photo-Optical Instrumentation Engineers (SPIE).

Figure 4.3 (a) and 3(d) show the AFM topography over the line-space patterns on the same resist film in two different measurements. As discussed in experimental methods, different detectors are required for the two wavenumber regions of interest, which is why the data presented here were acquired in two separate measurements. Because the resist film loses C_xH_y component and shrinks upon exposure, the bright regions in the AFM topography image represents unexposed areas while the valley region were exposed.

Line scans in the C-H scissoring and M-O regions were acquired along the red arrows marked in Figure 4.3 (a) and 4.3(d), respectively. During the measurement, the AFM tip moved along the direction of the arrow while taking FTIR spectra at 40-50nm intervals. In both C-H and M-O regions, peak intensity modulation can be seen across the line/space patterns. When the integrated intensity of peaks in both C-H and M-O regions are plotted as a function of distance, both chemical profiles track the topography height profile relatively well.

In summary, this section demonstrated the feasibility of using nano-FTIR to obtain nanoscale chemical information of nanopatterned photoresist films. The exposure removed C_xH_y species and transformed photoresist into amorphous metal oxide, as evidenced by peak intensity change in nano-FTIR spectrums. The observed modulation of C-H and M-O peak intensity across the line/space pattern can be directly correlated to alternating exposed/unexposed areas. The nanoscale spatial resolution, chemical sensitivity, and minimal radiation damage make nano-FTIR a promising candidate for fundamental study of material properties relevant in EUV lithography.

Case II: Protein assembly at interfaces

The structural and catalytic role of proteins is the foundation of living systems. Most proteins organize into well-defined hierarchical architectures with dynamic interactions (292, 293). Their assembly is governed by protein-protein interactions based on noncovalent hydrogen bonds, hydrophobic, and electrostatic interactions (294). The final form of the protein assembly is sensitive to environmental factors such as pH, ionic strength, and nature of the substrate (295-297).

The self-assembly of proteins has been widely used for biotechnological applications, including sensors, biocatalysts, and in biomaterial synthesis (298, 299). Although substantial effort has been spent to develop spectroscopy and microscopy tools to characterize protein assemblies, including X-ray crystallography, Atomic Force microscopy (AFM), Fluorescence Microscopy and cryo- Electron Microscopy (300-305), the invasive character of these tools raises concerns about potential alteration of the native structure. Furthermore, these tools primarily offer mostly morphology or structural information, leaving chemical properties and their dynamics largely unexplored. Infrared (IR) spectroscopy on the other hand is a non-destructive probe that can reveal their molecular scale structure.

The S-layer protein SbpA of the insect bacterium *Lysinibacillus sphaericus* was used as a model system to study biomolecular assembly. SbpA and other S-layer proteins constitute the major external cell component of many bacteria and archaea, serving as exoskeleton and molecular sieve for nutrient uptake (299, 306, 307). The formation is triggered by Calcium ions that bind to SbpA forming two-dimensional square lattices of tetrameric unit cells 13 nm in size (303, 308). The assembly process on various substrates, including carbon-based materials such as carbon nanotubes, has been studied in the past using imaging techniques, especially TEM and AFM (301, 303, 309-312).

We demonstrate that the combination of nano-FTIR spectroscopic imaging with the tip outside the liquid cell, and AFM topographic imaging with the tip inside the liquid cell (Figure 4.4 a and b), provides structural and chemical information of the proteins with high temporal and spatial resolution (153). The Amide I and Amide II bands of the protein were recorded during the assembly process, under different conditions of buffer solution. Their intensities grow non-linearly vs time and follow the increase in the percentage area of ordered protein domains obtained from AFM images. The spatial distribution of the Amide band intensities reveals inhomogeneities of the assembly that are not visible in previously reported microscopy results.

Figure 4.4 a show a schematic view of the liquid cell closed by the graphene membrane, where the SbpA proteins adsorb forming 2D lattices, with the AFM tip located outside during acquisition of nano-FTIR spectra. Figure 1b shows a schematic view of the cell for AFM topographic measurements in the same protein-buffer solution, with the tip inside the liquid.

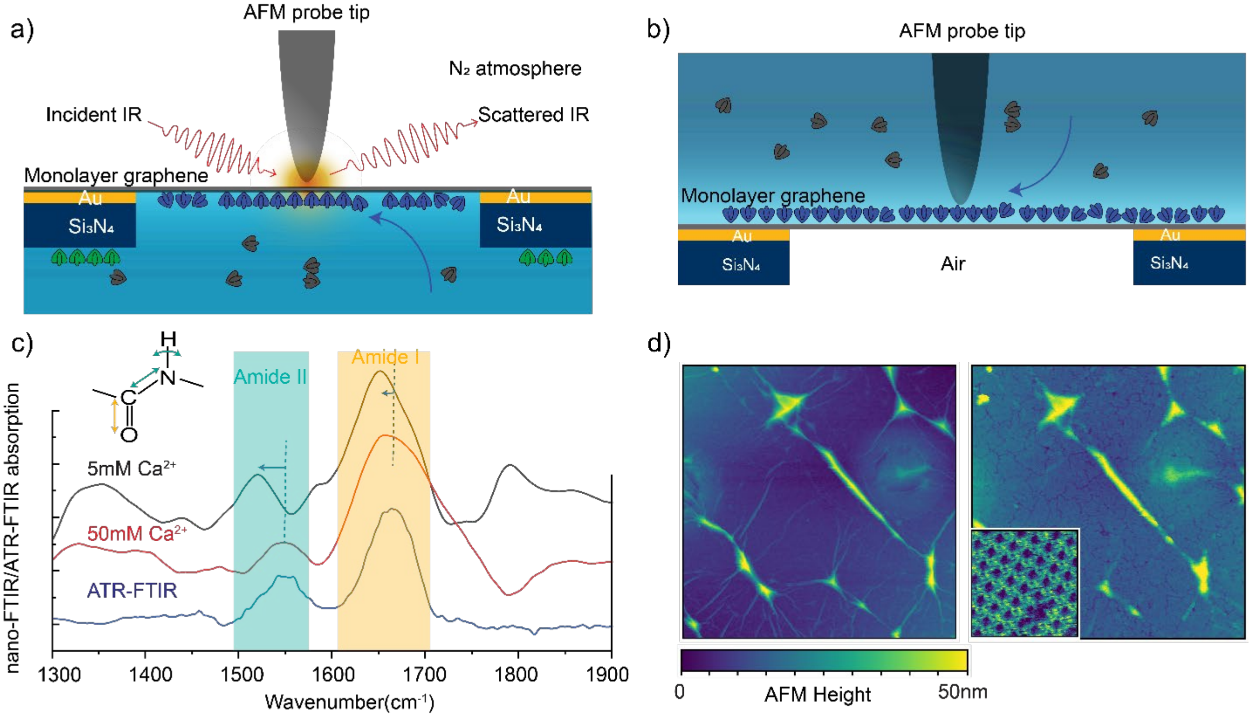

Figure 4.4 Schematic drawings of experiment, nano-FTIR spectra and AFM topographic images of SbpA proteins forming assembly layer. **(a)** Schematic drawing of the nano-FTIR experiment with the AFM tip situated over the monolayer graphene suspended across 1 µm diameter holes of a perforated Si_3N_4 membrane. **(b)** Schematic of the high-resolution AFM imaging with the probe immersed in the same protein-buffer solution as in a). **(c)** nano-FTIR spectra of an assembled film of SbpA proteins in a buffer solution of 5mM Ca^{2+}(black), and in 50mM Ca^{2+}(red), acquired 3 hours after filling the cell (top two graphs). The bottom graph (blue) is an ATR-FTIR spectrum of dried SbpA proteins assembled from a 50mM Ca^{2+} solution on a graphene-coated Au film on a Si wafer. **(d)** AFM topographic images of the graphene membrane prior (left) and after SbpA assembly (right) acquired 1h after filling the cell. The inset is an expanded image showing the square lattice structure of the assembled proteins. The scan size is 3µm for the large images and 90nm for the inset. Reprinted from ref (153). Copyright © 2022 the Author(s) under license CC-BY-NC-ND.

Nano-FTIR spectra of the SbpA protein assembly formed in buffer solutions with different Ca^{2+} concentrations are plotted in Figure 4.4 (c). The black trace corresponds to 5mM Ca^{2+}, the red to 50mM Ca^{2+}. The blue is an attenuated total reflection FTIR (ATR-FTIR) spectrum of dried assembled SbpA proteins on graphene-coated Au films that serves as reference. Details of data processing and assignment of the spectra can be found in the supporting material. Figure 4.4 (d) shows AFM topography images of the graphene membrane before (left), and after (right) being covered with SbpA. An expanded image is inserted to show the square structure of the self-assembled protein lattice. The bright features are due to wrinkles in the graphene. Protein domains form on both the suspended and supported regions in AFM imaging experiments where the tip scans over the suspended as well as the supported graphene. In the nano-FTIR experiments only proteins on the suspended graphene can be observed unless damage or detachment of the graphene accidentally occurs.

As shown in Figure 4.4 (c), the nano-FTIR spectra contains two main peaks, one around 1660 cm^{-1} and another around 1550 cm^{-1}. The first has a small contribution from the H_2O bending mode, and a larger contribution from the Amide-I (C=O stretching) mode. The second peak is due to the Amide-II (N-H bending coupled with C-N stretching) modes. Other peaks are observed below 1400 cm^{-1} which are attributed to the Amide III mode (313), while peaks around 1800 cm^{-1} (positive for 5mM and negative for 50mM) are of unclear origin. These spectra, while overall similar, show several important differences:

First, the center of the amide I and II bands show different red shifts, relative to the ATR reference spectra, as a function of Ca^{2+} concentration. In 5mM solution the shifts are 9cm^{-1} for amide I, and 20cm^{-1} for amide II. In 50mM buffer solution the shifts are 5cm^{-1} for amide I and almost no shift for amide II. This could arise from additional hydrogen bond formation with water molecules (314, 315).

Second, the intensity ratio of the amide I and II band is lower in 50mM Ca^{2+}. This change can be explained by the polarization of the IR near field, which is roughly oriented along the normal to the surface and thus more sensitive to vibration modes with transition dipole moments perpendicular to the surface (135, 316). The lower intensity of the Amide II band might indicate a preferential orientation of the N-H bonds vibration parallel to the surface, which correlates with a stronger ordering of SbpA monomers during self-assembly. Similar results have been reported for the purple membrane (PM) of *Halobacterium salinarum* on silicon substrates and Collagen Fibril on AuSi substrate by nano-FTIR (136, 317, 318). The change of peak intensity and shifts of the Amide bands provide critical information about the protein structural re-arrangement during lattice formation (301). We will focus on the Amide I and II band intensities and appearance in the following discussion.

Finally, a shoulder peak at higher frequency (near and above 1700cm^{-1}), is visible in the 50mM Ca^{2+} case, which could be due to IR absorption bands of the protein side chains (314). However, since the secondary structure of SbpA includes alpha helices, beta sheets, and beta turns (302, 313), it is difficult at present to assign these IR absorption peaks to different secondary structures.

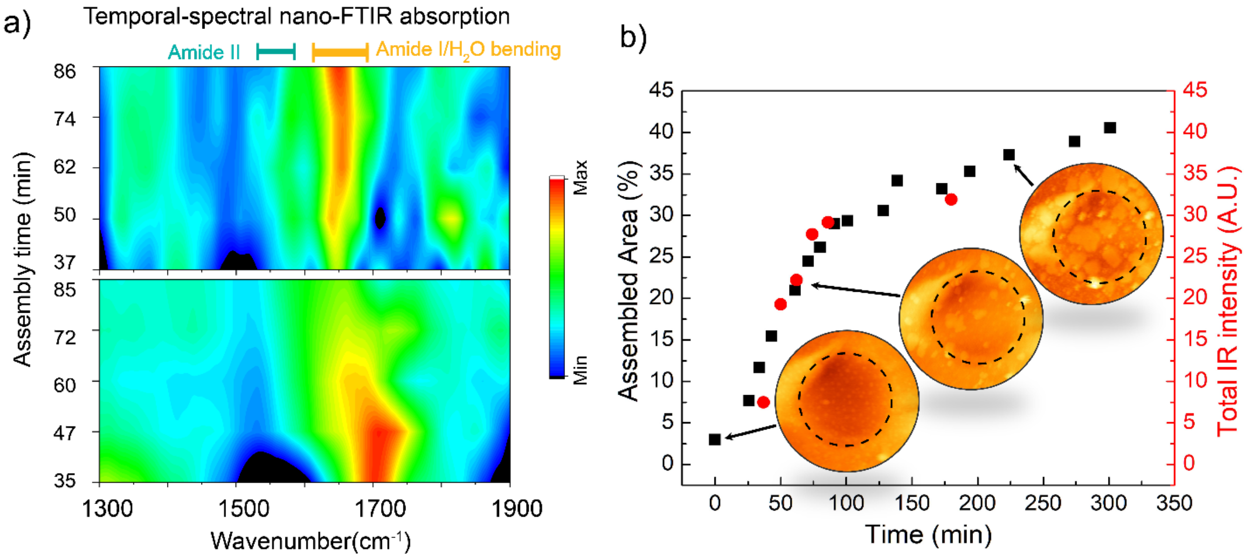

Figure 4.5 Temporally resolved assembly process of SbpA protein. **(a)** Color map representation of the time evolution of the nano-FTIR spectra during SbpA protein assembly on the graphene membrane in a buffer solution of 5mM Ca^{2+} (top), and without Ca^{2+} (bottom). **(b)** Percentage of area covered by assembled protein from AFM images in 5mM Ca^{2+} buffer solution (black squares, left Y-axis). Integrated intensity of Amide I and Amide II bands (red dots, right Y-axis) from the spectra shown in the top panel of a). (see Fig. 1). Reprinted from ref (153). Copyright © 2022 the Author(s) under license CC-BY-NC-ND.

The SbpA dynamical assembly process can be followed from the nano-FTIR spectra in the scale of minutes, the time required to collect one spectrum, while completion of the SbpA assembly takes hours. The top color map in Figure 4.5 (a) shows the nano-FTIR spectra of SbpA in 5mM Ca^{2+} buffer solution collected from 0.5h to 1.5h after filling the cell with the protein solution. The bottom color map shows nano-FTIR spectra acquired in a protein solution without Calcium ions. The three circular insets contain AFM images showing the growth of SbpA domains on the graphene membrane as a function of time. Time zero corresponds to the introduction of the protein/buffer solution into the cell. The suspended graphene boundary is marked by black dashed circles. In both cases the spectra were collected 3 hours after start of the assembly process, when the assembly process is nearly complete and the amount of SbpA monomers in the solution has been depleted.

As can be seen, the Calcium concentration strongly influences the SbpA assembly. In 5mM Ca^{2+}, after 1.5 h the intensity of the peak around 1660 cm^{-1} had increased by a factor of 4 compared to its value at 0.5h and remained nearly constant afterward. The same peak however, decreased and redshifted in the absence of Ca^{2+}, as shown in the bottom panel. The integrated intensity of the Amide I and II bands is plotted in Figure 4.5 (b) as a function of assembly time (red dots, right Y-axis). In parallel AFM images were used to follow the changes in the topography and protein domain size, which is shown in the same Figure 4.5 b) (black squares, left Y-axis). Three AFM images of the protein domains are shown insets, corresponding to the start, middle, and near end of the assembly process, respectively.

Several important factors deserve further discussion: First, although both the H_2O bending and Amide-I vibration modes contribute to the peak around 1660 cm^{-1}, the peak intensity increased more than four times during assembly. This increase is due exclusively to the ordering of proteins units, indicating that the bending mode of water contributes less than 25% of the overall peak intensity. The attenuation of the water bending mode will be discussed more thoroughly after the isotopic solvent exchange (H_2O by D_2O) experiments shown below. Second, there are two factors that potentially contribute to the increase of Amide I band over time: (i) more protein molecules adsorb on the graphene substrate, and (ii) gradual ordering of the adsorbed protein forming the crystalline phase, which orients its dynamic dipole more perpendicular to the surface. Since the adsorption (not the crystallization) took several minutes to complete, well before the nano-FTIR measurements, it is unlikely that increased adsorption is the major contribution (301, 303). Third, the area of assembled protein, obtained from the AFM topography images, shows a larger percentage of ordered domains at later times, indicating a good agreement between these two measurements.

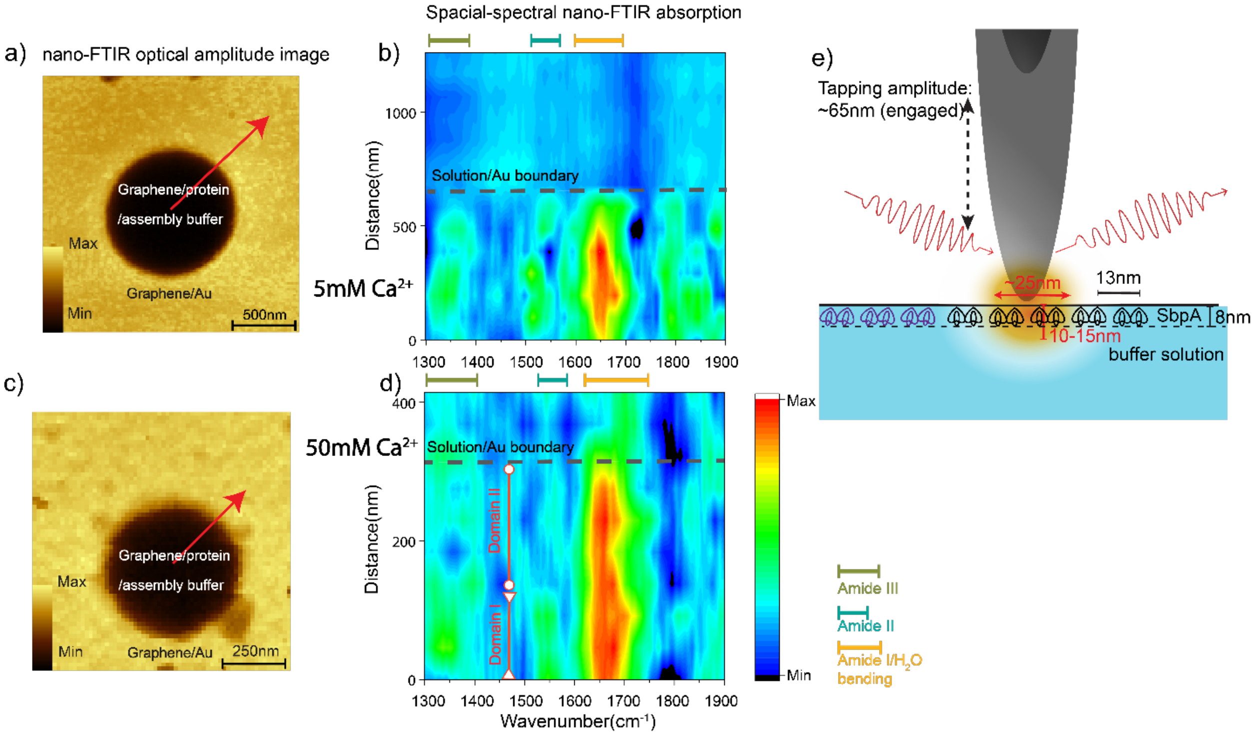

Figure 4.6 Spatially resolved chemical mapping of SbpA protein assemblies. **(a, c)** Images of the total scattered optical amplitude of suspended graphene and surrounding area in the cell filled with SbpA proteins, in 5mM Ca^{2+} buffer solution in (a) and 50mM Ca^{2+} solution in (c). **(b, d)** Corresponding color map representations of the nano-FTIR spectral intensities (arbitrary units in the color scale) of the Amide I and II mode regions of the SbpA proteins. (e) Schematic drawing of the tip-sample junction showing exponential decay of IR near field away from the tip apex. An SbpA lattice is drawn for comparison. Reprinted from ref (153). Copyright © 2022 the Author(s) under license CC-BY-NC-ND.

Calcium ions are essential for driving and stabilizing the crystallization of the monomers units(296, 302, 308). The evolution of the SbpA protein self-assembly process therefore depends on the Ca^{2+} concentration, as shown in Figure 4.6. Figure 4.6 (a) and (c) show images of the total near-field IR amplitude scattered by the tip as it scans over the graphene-covered holes and surrounding regions. The intensity increases when the probe is outside the suspended graphene window because of the strong scattering of all wavelengths by the underlaying gold. Nano-FTIR spectra acquired along the lines marked by the red arrows in (a) and (c) are presented as color maps in Figure 4.6 (b) and (d). The nano-FTIR profiles were acquired at positions along the red arrows in a) and c). The Amide I and II modes are only visible when the tip is located over the suspended graphene region in contact with the solution. The hole boundary is marked by the horizontal dashed lines. The position of two self-assembled domains in (d) are marked by the vertical red segments.

In both cases the spectra were collected 3 hours after start of the assembly process, when the assembly process is nearly complete and the amount of SbpA monomers in the solution has been depleted. In both 5mM Ca^{2+} and 50 mM Ca^{2+} solutions the intensity of the Amide I/II bands vary as the tip scans over domains formed at the graphene-solution interfaces. At least 3 different domains are visible in the 5mM case, and 2 in the 50 mM case, (marked by red segments). The size of these domains is a few 100 nm, close to the domain size measured in AFM topography images (Figure 4.5 b). The differences in spectra between different domains, especially in the Amide II band, suggest structural variation between domains. For example, the weakening of Amide II band in domain II in 50mM (Figure 4.6 b) is in line with the re-orientation of protein lattice units discussed above.

Hydrogen-Deuterium exchange experiments have been used widely in biological research to probe the folding pathways and conformational changes of proteins and their interactions(319-321). We therefore studied the effect of Deuterium substitution on the protein assembly by replacing the 5mM Ca^{2+} H_2O buffer solution in the liquid cell with 5mM Ca^{2+} D_2O buffer solution three hours after completion of the assembly process. Figure 4.7 (a) shows an AFM topographic image of a region showing a graphene-covered hole, after replacing the H_2O solution with a D_2O solution using a gentle slow flow of the solution to avoid turbulence or high shear flow. Figure 4.7 (c) corresponds to another experiment using an energetic rinse with a 5mM $Ca^{2+}D_2O$ solution. The corresponding nano-FTIR spectra along the red line arrows are shown as color maps in Figure 4.7 (b) and (d).

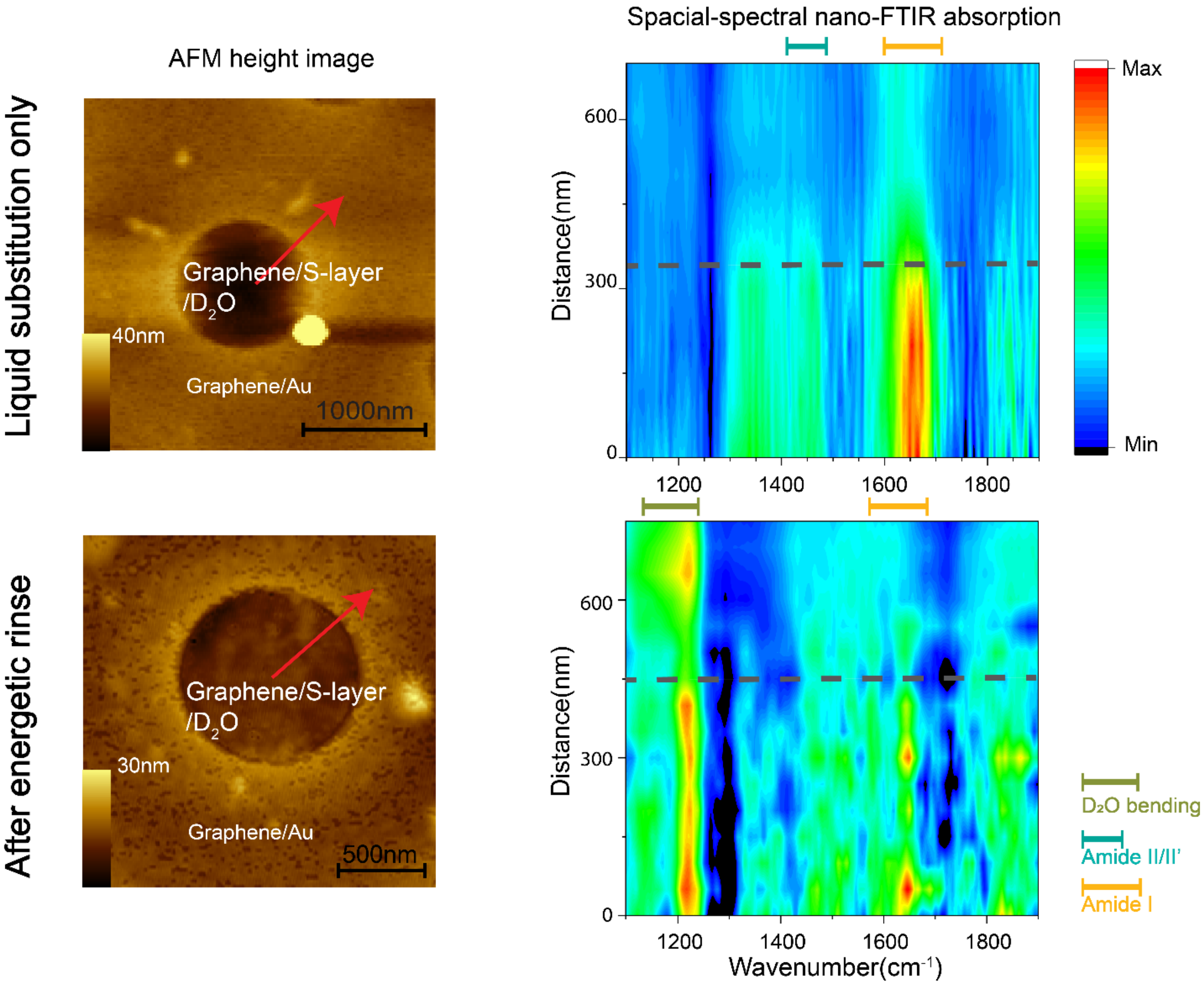

Figure 4.7 Effect of solvent replacement on SbpA proteins. **(a)** AFM topographic image of an area containing a graphene covered hole in the cell filled with SbpA proteins after gently substituting 5mM Ca^{2+} H_2O solution for 5mM Ca^{2+} D_2O solution. **(b)** Color map representation of the nano-FTIR spectra along the line marked by the red arrow in a). **(c)** AFM topographic image after a turbulent rinsing with D_2O that perturbed both the protein layers and the graphene membrane. **(d)** Color map representation along the direction of red arrow in c). The negative band around 1270 cm^{-1} (dark blue) in both cases is due to contamination of the AFM cantilever and tip with Polydimethylsiloxane (PDMS), which has a characteristic peak in that region. Reprinted from ref (153). Copyright © 2022 the Author(s) under license CC-BY-NC-ND.

After the gentle solution replacement, most of the self-assembled protein remained at the graphene-solution interfaces, although with a substantial change in the Amide II band in the nano-FTIR spectrum. The Amide II band is sensitive to H/D exchange because of the conversion of NH bonds to ND bonds, which have a lower frequency (314, 322, 323). As a result, the decoupled Amide-II' band shifted to 1450cm^{-1}, which is mostly due to the CN stretching mode, as seen in Figure 4.7 (b). The bending mode of D_2O (around 1220cm^{-1}, visible in Figure 4.7 d), however, is very weak or not observed in the nano-FTIR spectrum. This is because the nano-FTIR technique only probes vibrations within the decay length of the IR near field, which is usually 10-15 nm, i.e., roughly the tip radius of curvature or our tip. (136). Thus, the penetration of the IR near field through the protein assembly layer plus graphene, about 10nm, is very small, shading the underlying D_2O that did not intercalate between self-assembled protein domains and graphene.

However, the turbulent D_2O rinse altered the structure of the graphene window, first by detaching it from the surrounding gold support which allowed intercalation of water between the two (Figure 4.7 c). It also removed a large number of proteins, as shown in the nano-FTIR line profile (Figure 4.7 d), leaving only small protein domains on the surface, as evidenced by the intensity profile of the Amide-I band. These line scans further demonstrate the promising application of this platform to resolve biological nanostructures and their chemical changes down to tens of nm. The appearance of an intense D_2O bending mode at 1220cm^{-1}, along with the weaker Amide peaks in the graphene-covered hole region after the energetic rinsing, indicates that D_2O replaced H_2O and largely removed the initial protein layer covering the graphene. In addition, the D_2O peak is also visible even outside the suspended region due to intercalation between graphene and the surrounding Au film.

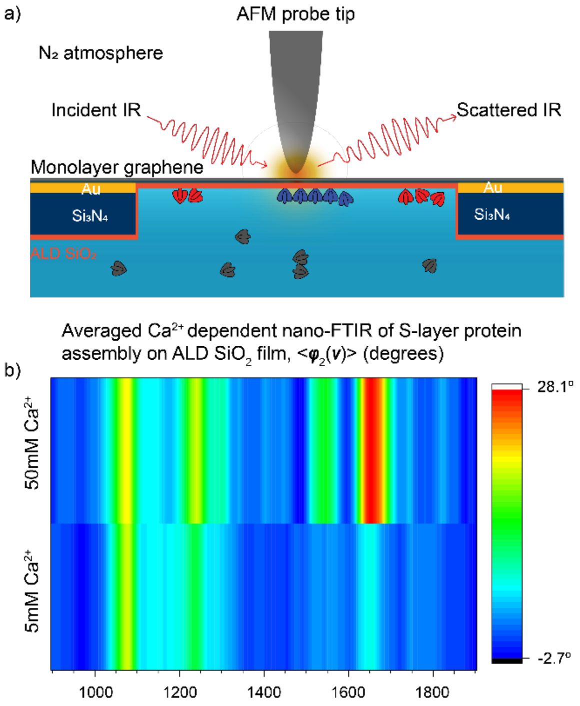

Figure 4.8 **(a)** Schematic of the nano-FTIR measurement of protein assembly on ALD thin oxide. **(b)** Ca^{2+} concentration dependent nano-FTIR displayed as a color map for 50mM Ca^{2+} (top) and 5mM Ca^{2+} (bottom).

Many natural processes and industrial applications also involved interfacing the protein assemblies and guest substrate. The protein-substrate interaction in these cases significantly affects the tertiary structure, the assembly behavior, and the biological function of protein (300). To demonstrate our capability to study protein-substrate interaction, we monitored SbpA protein assembly process onto an ALD grown 3.5nm thick SiO_2 film, as shown in Figure 4e. The details of the fabrication process have been reported in our previous work (181).

The resulting spectra are shown as colormaps in Figure 4.8. The top spectrum was collected in buffer solution with 50mM Ca^{2+}, while the bottom spectrum was collected in buffer solution with 5mM Ca^{2+}. Both spectra were collected 3 hours after the assembly start when the spectra were already near equilibrium. Two peaks at around 1080 cm^{-1} and 1220 cm^{-1} are attributed to the phonon mode of SiO_2 film (136). The amide region shows a large difference, with the amide mode intensity of SbpA protein in 50mM Ca^{2+} buffer solution is roughly 3.5 times higher than that in 5mM Ca^{2+} buffer solution. This difference has not been observed in AFM study before and might indicate a stronger ordering of SbpA protein in larger Ca^{2+} concentration. A more detailed investigation is needed here to understand the different assembly behavior in different Ca^{2+} buffer solutions on oxide film.

It is clear then that our graphene-based platform combined with AFM and nano-FTIR, makes possible *in vitro* studies of the structural and chemical evolution of biological material, exemplified here by the study of the self-assembly of SbpA proteins on graphene. The growth of amide I and II band intensities of SbpA protein follows a non-linear behavior vs time, in good agreement with the dynamical information obtained from AFM topographic images. After assembly, the amide band line profile unambiguously reveals the structural response of protein to environmental factors, including ionic strength and solvent, which is hard to access by AFM. We demonstrated that the dynamical evolution of protein substructure in different environment, the interaction between the protein and matrix, and the biological interfaces between protein-substrate, protein-water can be studied using our approach, providing missing knowledge for bioengineering. The nm spatially resolution, chemical sensitivity, negligible radiation damage, and environmental capabilities of our platform opens many opportunities to study other complex soft materials and nanostructures.

Case III: Catalyst for electrochemical reaction

Electrochemical catalysis can convert small molecules such as carbon dioxide and water into value added chemicals, which holds the promise of generating sustainable fuel for a carbon neutral economy. Inspired by highly efficient enzyme system in living organisms, rational design of electrocatalysts often involve tuning the electronic structure and controlling the nanoscale morphology of catalyst nanoparticles by introducing additional intermolecular interactions, such as attaching ligands near catalytic active sites. These strategies have been demonstrated to be effective in changing the structure and properties of catalytic microenvironments, facilitating electron, energy, and mass transfer at the interfaces, and even altering the reaction pathway.

Fundamental knowledge of catalytic microenvironment under reaction conditions is therefore a most critical part for catalyst engineering. However, this is hampered by several limiting factors. First, the microenvironment near electrochemical catalysts, especially nanoparticles, is highly heterogeneous, which necessitates nanometer scale mapping of the microenvironment. Second, various forms of intermolecular interactions are involved at the electrochemical interfaces, including hydrogen bonding, hydrophobic interaction, and specific adsorption and assembly of molecular species. Under reaction conditions, dynamical formation and breaking of chemical bonds takes place, which further complicates the microenvironment structure. Third, during electrocatalysis reaction, biasing the interface drives surface atom migration and nanoparticle coalescence while also stabilizing metastable species and configurations by changing the energy landscape, and this dynamical information is missing in ex-situ study (e.g., after bias).

Over the past decades substantial efforts have been spent to decipher the catalytic microenvironment, using either experimental or theoretical approach. X-ray and electron-based techniques focus on the elemental distribution and morphology of catalyst and being less sensitive to the light element (C, O, etc.) and intermolecular interaction. Besides, the energetic electrons and photons ionize molecular species, induce undesired side reactions, and drive the microenvironment out from equilibrium. On the other side, Infrared and Raman provide the molecular vibrational details, but the spatial resolution is limited to the order of micrometer due to the diffraction of the long wavelength beam.

Nanoscale infrared spectroscopy, or nano-FTIR, circumvents the diffraction limit by combining infrared spectroscopy with the high spatial resolution of atomic force microscopy (AFM). Nano-FTIR has been utilized to study the nanoscale structure and chemical information of many soft materials, including polymer, protein self-assembly layers and electrocatalyst (142, 143, 147, 148, 150, 153, 324).

Early efforts introducing nano-FTIR techniques to fluid environment faced various drawbacks, including viscous damping of the AFM tip, strong absorption of IR by water. In addition, ATR crystals are the only choice as substrate (151, 152). A novel approach was developed in our group in 2019 by Lu et al. who utilized a single layer graphene to separate the electrochemical environment from the AFM tip while serving as both substrate and working electrode for electrochemical measurement (155). Using this platform, the vibrational fingerprint of molecules at the interfaces could be resolved nondestructively with nanometer resolution under electrochemical conditions (153, 181).

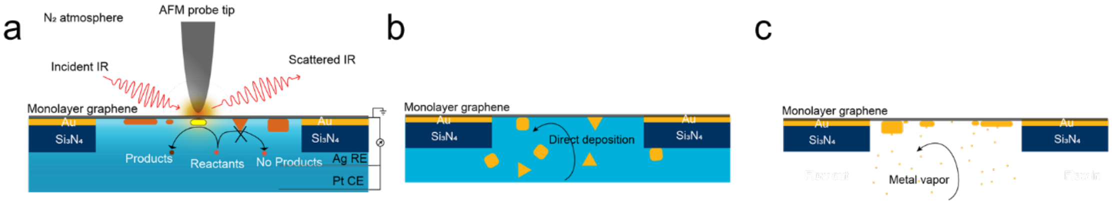

Figure 4.9 Illustration of the nano-FTIR with graphene liquid cell for the study of nanoparticle under electrochemical conditions. The nanoparticles can be prepared by either drop casting/spin coating (b) or evaporation (c).

This combination of nano-FTIR with the graphene liquid cell could be used to probe the interfacial microenvironment under electrochemical conditions, as shown in the illustration Figure 4.9. Nanoparticles could be deposited on the solution side of graphene membrane by either drop casting, spin coating (Figure 4.9 b) and thermal evaporation followed by annealing (Figure 4.9 c).

As a proof-of-concept experiment, 3nm Au was evaporated onto the graphene and annealed under vacuum up to 573K for 48h, and the resulting nano-FTIR results are shown in Figure 4.10. Figure 4.10 (a) and (b) show images of the total amplitude of the near-field IR scattered by the tip and AFM topographical images as it scans over the graphene-covered holes and surrounding regions, respectively. Four holes are included in images (a) and (b) which also show a few bright features in (b) (dark in a) caused by Au particles that migrated to the top side of the membrane and are not in contact with the liquid. Zoom-in images of total near-field IR amplitude scattered by the tip and topography of the area marked by the red dash square in (a) are shown in Figure 4.10 (c) and (d). As can be seen in (b) and (d), there are only a few Au nanoparticles in one hole. A few bright lines are due to wrinkles in the graphene that likely serve to anchor the Au nanoparticles. As shown in Figure 4.10 (e), the nano-FTIR spectra over the suspended region away from the Au (gray) shows only one peak around 1150 cm^{-1}, which corresponds to the bending mode of the D_2O molecules in the liquid cell. Spectra taken with the tip located over an Au particle (red) and at the edge between three Au particles (blue) are compared in (e) without further normalization. Clearly on top of suspended graphene the spectrum is very noisy, while the spectrum on the edge (grey) and at the junction of nanoparticles (blue) is smoother and much stronger. An enhancement factor between 3 and 10 can be concluded from the peak areas. The enhancement is likely due to the resonant plasmonic coupling between nanoparticles and the tip.

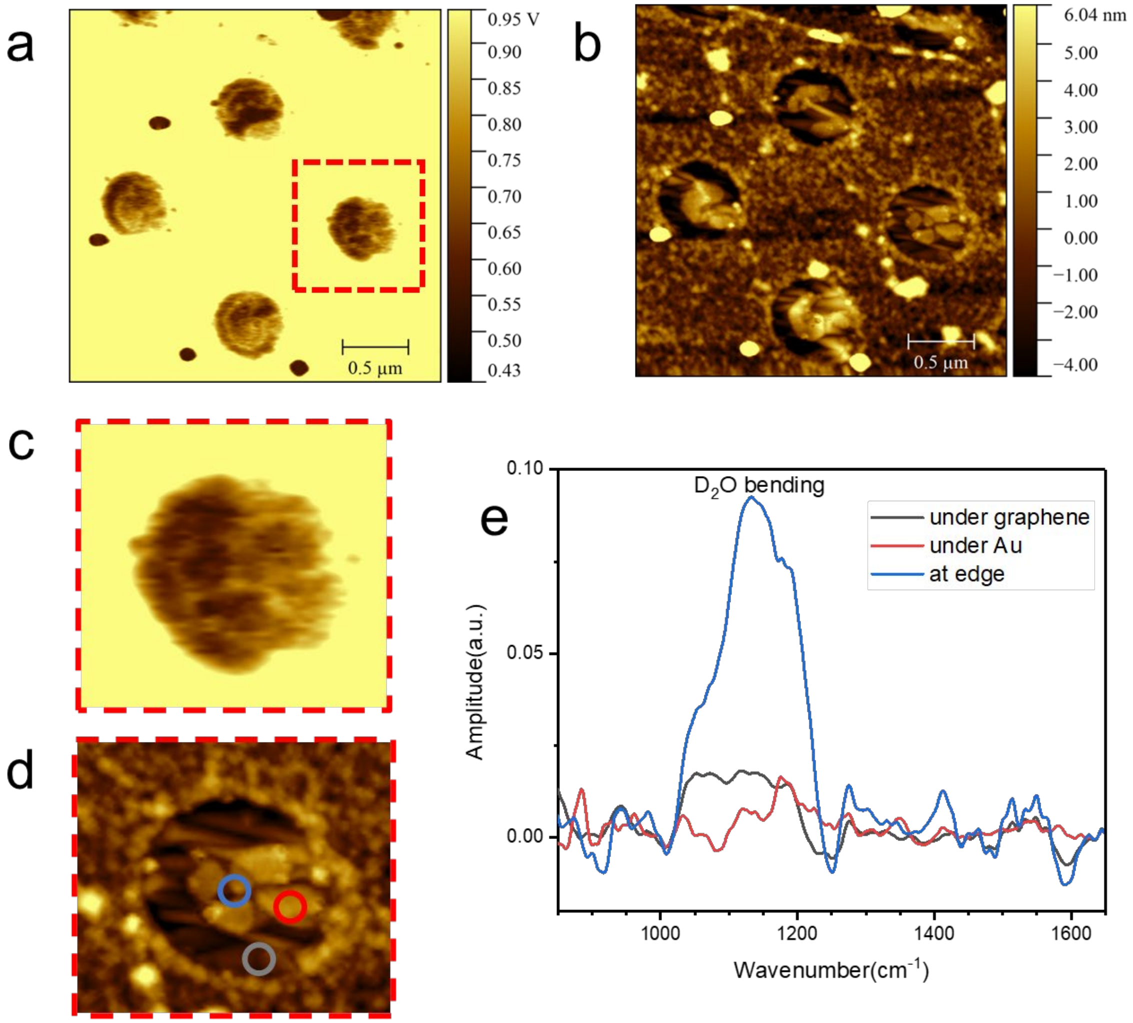

Figure 4.10 Nano-FTIR spectroscopic imaging of Au nanoparticle supported on single layer graphene in contact with D_2O. **(a)** nano-FTIR second harmonic optical amplitude image **(b)** AFM topographic image of an area containing four Au nanoparticles/graphene covered holes in the cell filled with D_2O. **(c)** nano-FTIR second harmonic optical amplitude image **(d)** AFM topographic image of the area marked by red dash square in (a). **(e)** nano-FTIR spectra (amplitude) taken at three different spots marked as blue, red and grey circles in (d).

The results in Figure 4.10 clearly demonstrate that the nano-FTIR with graphene liquid cell can be used to track and fingerprint molecules on and around nanoparticles.

The plasmonic enhancement of the signal can facilitate the detection of molecules, as in the example shown of CO on Pt, shown in (Figure 4.11).

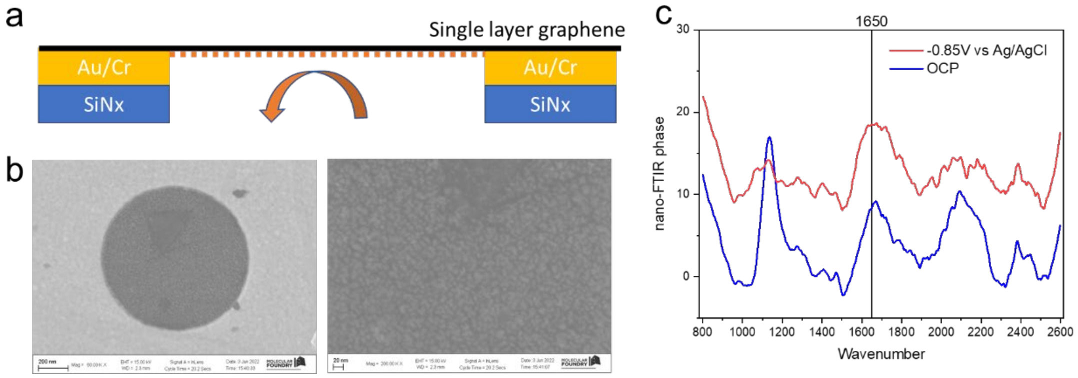

Figure 4.11 nano-FTIR spectra from CO on Pt clusters in contact with CO in CO_2 saturated 0.1M $NaHCO_3$ electrolyte. (a) a film of small Pt clusters deposited on graphene by ALD. (b) TEM images of a single graphene hole and a zoom-in image (right side) showing the small clusters covering the graphene. (c) nano-FTIR spectrum of Pt clusters in contact with CO, CO_2 saturated 0.1M $NaHCO_3$ electrolyte under bias.

Small Pt nanoclusters (2-5nm) were evaporated on graphene using PE-ALD (Figure 4.11 a and b) (325-329) and the liquid cell was filled with CO, CO_2 saturated 0.1M $NaHCO_3$ electrolyte. Figure 4.11 (c) shows the nano-FTIR spectra averaged over the whole suspended hole under different electrochemical bias. As shown in Figure 4.11 (c), the nano-FTIR spectra contains four main peaks, the peak around 1100 cm^{-1} could be due to unknown species containing C-O bonds adsorbed on Pt clusters during ALD deposition or others of unclear origin; the peak around 1650 cm^{-1} is due to the bending mode of H_2O molecules in the liquid cell; the peak around 2100 cm^{-1} can be assigned to the stretch mode of CO molecules adsorbed on the Pt. Finally, the peak around 2380 cm^{-1} ca be assigned to the stretch mode of CO_2 molecules dissolved in the electrolyte. Since the solubility of CO in the electrolyte is very low, the fact that it appears on the spectrum demonstrates that CO is concentrated as an adsorbate on the Pt particles, as expected from the known strong binding of CO to Pt.

Under negative bias (-0.86V vs. Ag/AgCl) two peaks decreased: the C-O containing species at 1100 cm^{-1}, and the CO molecular peak at 2100 cm^{-1}. The decrease of C-O species is likely due to electro-reduction of the that species on the Pt surface, maybe replaced by H^+ ions in the electrolyte under negative bias (211, 213). The conclusions regarding the unknown C-O containing species, however, need further confirmation and investigation, and are shown here to illustrate the capabilities and potential of the technique for studies of electrochemical reactions in operando conditions.

Conclusion

The three cases shown in this chapter demonstrate how the nano-FTIR with or without graphene liquid cell can be used to probe and obtain nanoscale chemical information of soft material at interfaces. These soft materials (photoresist and protein) are very sensitive to radiation damage that they cannot be studied spectroscopically with x-ray or electron probes techniques. Only techniques with low energy probes (both photon energy and photon flux) might be used for experiments. IR from synchrotron light is coherent and broadband, with a flux many orders of magnitude higher than normal white light, although lower than in a laser. No obvious beam damage has been observed in this experiment. The nano-FTIR only relies on the optical response between the tip and the sample, which is a long-range interaction that passes through single layer graphene/ultra-thin oxide. Other competing IR based techniques, AFM-IR or PiFM (Peak induced Force Microscopy, measuring the IR induced force change at tip-sample junction) might not be suitable for this liquid cell setup.

The graphene liquid cell combined with AFM and tip-enhanced IR platform has many advantages. First, it overcomes the strong IR absorption of aqueous film, which ensures good signal strength. Second, since the tip is separated from the liquid environment, there is no viscous damping of the tip oscillation. This prevents both the tip and the sample from damage/contamination, since in normal nano-FTIR setup the free amplitude is usually ~100nm, much larger than that in in-liquid AFM. Third, there is a variety choice as substrate, being graphene, ALD oxide, nanoparticles, plastic film, lipid, etc., and the region of interest is unlimited, which is much better than the nano-FTIR in ATR setup where the IR spot on the ATR crystal is fixed.

However, there are also some drawbacks. The graphene membrane almost blocks the mechanical interaction between the graphene and the tip, so in most cases the topography/amplitude/phase channels in nano-FTIR are not very useful, only providing some guidance on the suspended region. In some cases (such as nanoparticles) there are still some useful features in the topography images that reveal the position and shape of nanoparticles. This can be partially resolved by the state-of-art nano-FTIR with QCL laser, in which the incident light can be a fixed but variable value. The optical amplitude map/phase map at the given frequency could possibly substitute the mechanical channel.

With the advance of fabrication technology, the spatial resolution, which is correlated to the tip apex radius, can be further increased, and it is anticipated that dynamic IR spectroscopic study of a single protein or DNA molecule during the execution of its biological function will be possible in the future.

Chapter 5 Summary and Outlook

Abstract

This chapter includes a summary of the interfacial processes and properties that deserve further attention, as well as a prospective on the future development of surface-sensitive spectroscopy for solid liquid interfaces.

This chapter only reflects the author's thoughts and opinions.

Conclusion: Multimodal investigation of solid-liquid interfaces

In this dissertation a new methodology has been developed (Figure 5.1), which combines many surface-sensitive techniques with a home built liquid cell enclosed by an ultra-thin free-standing membrane (155, 181). This methodology has been demonstrated to be a promising strategy on many interfacial studies (86, 153, 155, 181) The electrical double layer structure (chapter 3) and soft material at interfaces (chapter4) have been investigated using this approach.

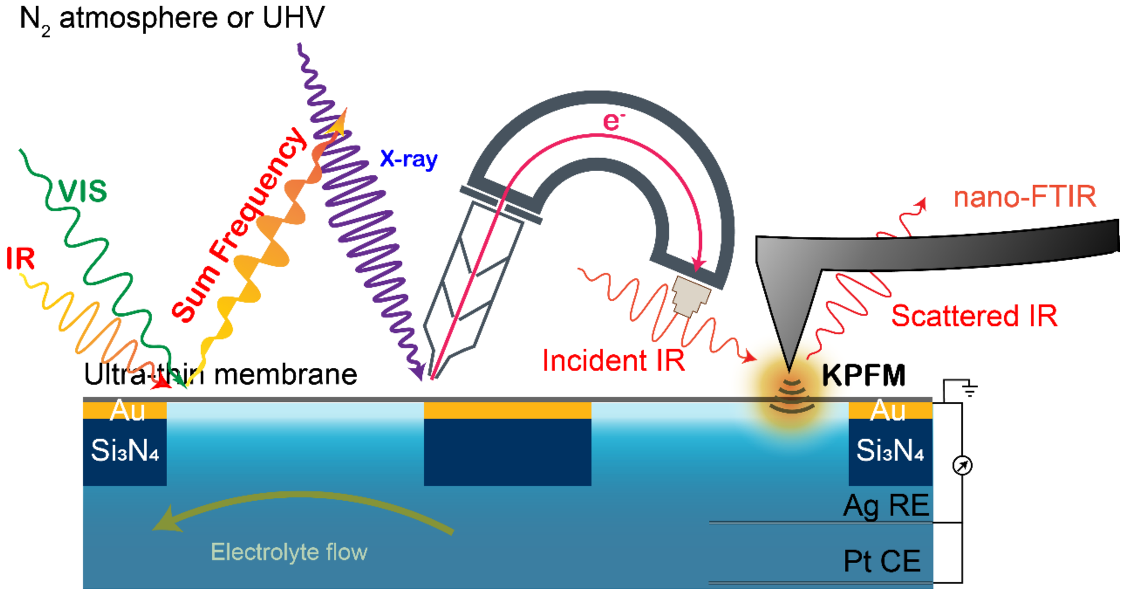

Figure 5.1 Schematic drawing of the liquid cell with ultra-thin membrane for surface-sensitive spectroscopy.

The membranes used here can be a single (multi) layer graphene, or graphene supported oxide/metal film, or sample film (plastic, protein, etc.) and nanoparticles supported on graphene membrane. These membranes are mechanically robust, chemically resistive, and thin enough to let low energy X-ray photoelectron go through. With that we extended the pressure limit of XPS from mbar regime to at least 1 bar. These membranes can be used as supports of metal particles for catalysis studies, as electrodes in electrocatalysis, in batteries, and in many other applications. By combining these membranes, together with home designed liquid (electrochemical) flow cell and surface-sensitive techniques, the chemical properties of solid-liquid interfaces could be accessed at atomic or molecular level.

As shown in the chapter3, the structure of the electrical double layer near graphene and anatase were probe using the combination of multi techniques, including SFG, nano-FTIR, KPFM, XANES and XPS. For the study on graphene-sulfate solution interfaces, the first water layer in contact with graphene has dangling O-H bond that points to the graphene and remains unchanged both with salt concentration and with increasing positive potentials but undergoes a chemical interaction with graphene at high negative values that decreases its peak intensity and redshifts its frequency. Sulfate was found to preferentially accumulate near the graphene, creating an electrical field that orients water molecules below the interfaces. The degree of orientation of the water molecules as well as the electrical double layer strength increases further when positive voltages are applied. For anatase-NaCl solution interfaces an ice-like water bilayer structure was found which reveals the strong interaction between anatase and water.

As shown in chapter4, nano-FTIR provides nanoscale chemical information of soft materials at interfaces nondestructively, which was hard to access in the past. For the application on photoresist, clear evidence of exposure-induced chemical modification was observed at a spatial resolution down to 40 nm, well below the diffraction limit of infrared light. The chemical gradient of C-H and Metal-O bond also agrees with the topographical height across the grating patterns. For the research on protein assembly, nanoscale dynamic evolution of the protein was recorded by following the amide I and II vibration bands. The amide band line profile of protein assemblies reveals the structural inhomogeneity, and the structural response of protein to the external environment, including ion and solvent have been studied. These observations revealed unprecedented details of protein assembly dynamics. The current projects focus on nanoparticle ligand and intermediates for CO_2RR and plastic decomposition and functionalization, and this offers complementary molecular information to the field.

It can be concluded that this methodology enables the study of many interfacial properties and processes, including the water orientation, ion segregation and solvation and dynamical assembly. Each technique provides partial information and the combination of them can be quite powerful for surface science studies.

In the following sections a short perspective will be given for each process at interfaces, and suggestions on how to tackle these problems. For in depth studies, many books and review papers are extremely helpful (1, 2, 48, 61, 62, 67, 85, 111, 114, 135, 145, 146, 177, 341-347).

Potential profile and potential drop

Almost all the solid-liquid interfaces are charged, and the charge can come from an applied potential, adsorption, insertion or leaking of some ions and hydrolysis of the surface groups. The distribution of electrical field in the liquid induced by the charge changes the energy landscape of many species, affects their segregation and de-solvation at interfaces and sometimes even the reaction pathway. The segregated counter ions (partially) screen the electrical field and prevent the electrical field from spanning into the bulk, while also creating a strong potential drop at Inner Helmholtz Plane and Outer Helmholtz Plane. The resulting potential profile along the interfaces normal can be expressed by equation:

$$E_{DC}(z) = \frac{\frac{4k_BT}{e}\kappa \tanh\left(\frac{e\phi_0}{4k_BT}\right)}{\tanh^2\left(\frac{e\phi_0}{4k_BT}\right)\exp(-2\kappa z) - 1}\exp(\kappa z)$$

Where $\kappa^{-1} = \lambda = \left(\frac{\varepsilon k_BT}{2ce^2}\right)^{\frac{1}{2}}$ is the Debye length, $\phi_0 = -\frac{2k_BT}{e}\sinh^{-1}\left(\frac{e\sigma}{(8k_BT\varepsilon c)^{\frac{1}{2}}}\right)$ is the surface potential. But in realistic cases, the potential profile is rather complicated. Up to now there are only a few experimental tools to probe the potential drop across the interfaces other than electrochemical methods. Some promising candidates includes Kelvin Probe Force Microscopy (in liquid or with liquid cell) (348, 349), XPS (with liquid film/jet or liquid cell) (41, 46, 56, 171,

173) and SHG/SFG (with the help from advanced fitting methods) (86, 87, 90, 95, 222). KPFM measures the surface electrical field (or local work functions/charge distribution) or electrical field gradient by sensing the electrostatic force between the sample and the biased tip, thus it can sense and measure the preferential segregation of ions to the interfaces. In XPS, ions at different potential relative to the electrode have different vacuum levels and therefore slightly different positions in the spectrum. In SFG the electrical field modulates the third order nonlinear term and the SF intensity. These techniques are either hard to operate, or expensive, or need some advanced fitting and simulation to interpret the results.

Concentration profile and speciation

The charge at the interfaces attracts counter ions to the interfaces, and to maintain charge neutrality, co-ions are also segregated towards the interfaces. This segregation of both cations and anions to the solid-liquid interfaces is very different from the case of air (vacuum)-liquid interfaces, where ions can be either segregated or repelled from the interfaces.

The enriched concentration of ions or small molecular species at solid-liquid interfaces modified the microenvironment for electrochemical and biological processes. For example, different alkali ions segregated to the interfaces have different effects to the electrical double layer field strength and this changes the reactivity of many electrochemical reactions. The enriched proton at different side of the membrane maintains acidic or basic environment in some organelles and optimizes the performance of enzymes.

There are many techniques that can possibly tackle the concentration distribution of ions across the interfaces and speciation at the surface. XPS (with liquid film/jet or liquid cell) is sensitive to the concentration and the chemical state of metal ions at interfaces, while nano-FTIR (with liquid cell) being more sensitive to the concentration and chemical state at the molecular level. The differential segregation of ions can also be inferred from the potential signal by KPFM and SFG/SHG, but some assumptions must be made.

Solvation and de-solvation

The solvation and de-solvation of ions plays a critical role in many electrochemical and biological processes. A typical case in the electrochemical reaction is the solvation and ion-pairing of lithium in nonaqueous electrolyte. As the lithium-ion concentrations increase (to around ~3M), fewer solvent molecules (such as EC) become mobile, and some solvation configurations that are less common become dominated, such as counterion to form contact ion pairs (CIPs), solvent-separated ion pairs (SSIPs), and aggregates. This solvation configurations occurs at most commercial systems and attracted much research efforts (350-353).

However, experimental investigation of the solvation structure and dynamics at the interfaces still lags. This could be partially resolved again by the nano-FTIR and XPS, but most of the time the knowledge of solvation structure is retrieved by controlling the ratio of ions to the electrolyte. Bulk solvation structure probed by Raman and IR could possibly yield some light on the solvation structure of ion at interfaces, but the exact interfacial solvation structure and the effect of bias still deserve further attention (351).

Water at interfaces

The water molecules have a strong dipole moment and typically orient in the presence of electrical field at solid-liquid interfaces. This preferential orientation depends on many factors including the electrical field strength, the solid-water interaction, and the temperature. The properties of the first few layers of water play a critical role on many macroscopic properties of materials, such as hydrophobicity and hydrophilicity of materials, water uptake of minerals from environments, protein folding and adhesion, as well as some electrochemical reactions such as water splitting in photosynthesis.

The structure of the first few layers of water can have distinct properties on many materials. For instance, on the surface of TiO_2 (anatase) the liquid water forms a layer or ice-like order structure at room temperature (23, 25, 26, 263), while on MgO it has been proposed that the surface is hydrophobic due to the existence of dangling OH (OH that do not form hydrogen bond with the neighboring water/oxide) (28).

Water adsorbed on metal and oxide surfaces have been extensively studied using various techniques in surface science including Scanning Probe Microscopy, Temperature Programmed Desorption and Infrared spectroscopy, but the case of aqueous solution in the presence of salt or electrical field is less understood. SFG has been used to probe the orientation and hydrogen bonding network of interfacial water in contact with minerals (e.g., mica), oxide and lipid (28, 86, 87, 94, 101, 263, 354, 355), and recently XANES with electrochemical flow cell has also been developed and utilized to probe the hydrogen network and ordering of the water molecules in contact with metal and oxide (23, 66-68, 176). Shell isolated nanoparticle-enhanced Raman spectroscopy (SHINERS) has also been demonstrated to probe the water structure at confined space between nanoparticles and substrate (132). Other spectroscopic techniques such as XPS are generally not so sensitive to the hydrogen bonding environment and orientation, so they couldn't offer much information.

Perspective: Surface-sensitive spectroscopy for solid-liquid interfaces

How much sensitivity is needed for the study of solid-liquid interfaces? Even for the most surface-sensitive spectroscopic technique-soft X-ray Photoelectron Spectroscopy, the probing volume is still >1nm, even higher than 3nm if the energy of photo-electron is higher. As the result simulation is often needed to interpret the results, which brings in extra uncertainty.

However, in many cases surface sensitivity can be achieved if the species of interest only appears at the interfaces. For instance, CO has very low solubility in aqueous solution and prefers to segregate to the Pt electrode, therefore all the peak intensity of CO in the IR spectrum comes from the interfaces, the same is true also for some intermediates during electrochemical reaction. This strategy works well for some cases, but for most of interfacial properties, such as the interfacial pH and solvation shell the surface sensitivity from the techniques themselves is still necessary.

Study of solid-liquid interfaces also benefits from other areas such as ultra-fast techniques and X-ray imaging techniques. The temporal and lateral resolution of these techniques can possibly bring other dimensions to interfacial studies in the future.

Perspective: Achieving depth resolution for solid-liquid interfaces

"In-situ/operando characterization of material at the nanoscale" is the goal of many material scientists. Unfortunately, most characterizations only offer nanoscale resolution on the x-y plane and overlook possible changes in z direction (depth).

XPS/SWXPS is one of the few techniques which offer quantitative chemical information in z direction. But the complexity of experimental setup only allows for study of material in gas phase/exposed of nm thin liquid film, preventing its general application under electrochemical conditions.

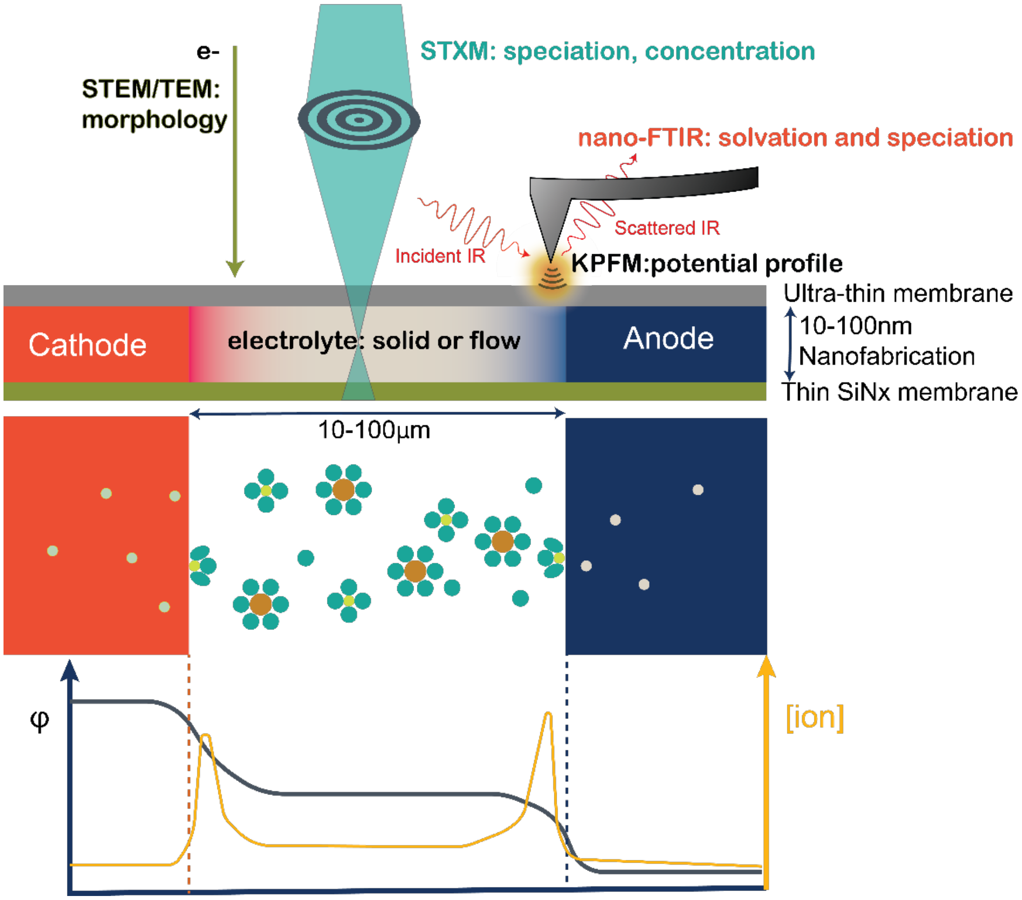

Figure 5.2 Illustration of the "cut a slice" approach of solid liquid/solid interfaces

Another possible solution is to "cut a slice" of solid liquid/solid interfaces and convert the depth resolution into spatial resolution, as shown in Figure 5.2. It requires fabrication and separation of electrodes at micrometer scale on x-y plan and electrolyte (liquid or solid) filing between them. An ultra-thin membrane could be fabricated on top to protect the electrolyte species from leaching into the chamber or being oxidized by atmosphere. With such devices many common nanoscale characterization techniques, including nano-FTIR, STXM, KPFM could be used, and the combination of these techniques will reveal the elemental, chemical and potential profile across the interfaces at tens of nm scale.

Significance

This backside approach developed here introduced many surface-sensitive techniques to liquid and offer many opportunities for fundamental study of solid-liquid interfaces, with less radiation damage, nanometer spatial resolution, surface, and chemical sensitivity. By bringing together vibrational spectroscopy, core-level X-ray based spectroscopy and microscopy together, the whole picture of interfaces, including the speciation (XPS, NEXAFS, nano-FTIR), concentration profile (XPS), potential profile (SFG, KPFM) and water orientation (SFG) could be drawn. Some preliminary work (interfacial ice-like water structure near anatase, hydrophobicity vs. hydrophily of single layer free standing graphene) have already filled the long missing knowledge of surface chemistry and attract wide attention in this field.

It is anticipated that this methodology will also open new avenues in the fields of material science and engineering including electrocatalysis, energy storage, biophysics and environmental science. Researchers in those fields now could understand many fundamental properties and processes taken place in their system, including catalysis microenvironment, solvation/de-solvation, ion intercalation and protein folding and assembly. This knowledge will bridge the gap between the idealized model (e.g., Stern model) with the processes taken place in the real system.

For electrocatalysis and energy storage, research is mostly focusing on the chemical and physical properties of the electrode, with little attention on the interfaces and electrolyte, where many critical processes like de-solvation, segregation and adsorption take place. This methodology takes advantage of surface sensitivity and fulfills the missing knowledge in their systems.

For biophysics, many critical questions remain unclear due to the shortage of appropriate nondestructive characterization tools. It has been demonstrated that the dynamical folding and evolution of protein substructure in different environment, the interaction between the protein and matrix, and the biological interfaces between protein-substrate, protein-water can be studied using this approach, providing missing knowledge for biophysics and bioengineering.

References

1. F. Zaera, Probing Liquid/Solid Interfaces at the Molecular Level. *Chem Rev* **112**, 2920-2986 (2012).

2. A. R. Head, S. Nemk, B. Eren, *Ambient Pressure Spectroscopy in Complex Chemical Environments* (The Weizmann Institute of Science, 2021).

3. G. Gonella *et al.*, Water at charged interfaces. *Nature Reviews Chemistry* **5**, 466-485 (2021).

4. G. E. Brown Jr, G. Calas, Mineral-aqueous solution interfaces and their impact on the environment. *Geochemical Perspectives* **1**, 483-484 (2012).

5. M. Kleber *et al.*, Dynamic interactions at the mineral–organic matter interfaces. *Nature Reviews Earth & Environment* **2**, 402-421 (2021).

6. C. L. Hurd, A. Lenton, B. Tilbrook, P. W. Boyd, Current understanding and challenges for oceans in a higher-CO2 world. *Nature Climate Change* **8**, 686-694 (2018).

7. A. Putnis, Why mineral interfaces matter. *Science* **343**, 1441-1442 (2014).

8. H. Jin *et al.*, Recent advances in emerging integrated antifouling and anticorrosion coatings. *Materials & Design* **213**, 110307 (2022).

9. A. J. Herrmann, J. Sorwat, J. M. Byrne, N. Frankenberg-Dinkel, M. M. Gehringer, Diurnal Fe(II)/Fe(III) cycling and enhanced O2 production in a simulated Archean marine oxygen oasis. *Nat Commun* **12** (2021).

10. S. Zhang *et al.*, Engineering Biomolecular Self‐Assembly at Solid–Liquid Interfaces. *Advanced Materials*, 1905784 (2020).

11. D. Coglitore, J.-M. Janot, S. Balme, Protein at liquid solid interfaces: Toward a new paradigm to change the approach to design hybrid protein/solid-state materials. *Advances in Colloid and Interfaces Science* **270**, 278-292 (2019).

12. D. Laage, T. Elsaesser, J. T. Hynes, Water Dynamics in the Hydration Shells of Biomolecules. *Chem Rev* **117**, 10694-10725 (2017).

13. J. Teissié, M. Prats, P. Soucaille, J. F. Tocanne, Evidence for conduction of protons along the interfaces between water and a polar lipid monolayer. *Proceedings of the National Academy of Sciences* **82**, 3217-3221 (1985).

14. Anonymous, Contents page + Editorial Board. *Trends in Pharmacological Sciences* **35**, i (2014).

15. J. P. Seymour, F. Wu, K. D. Wise, E. Yoon, State-of-the-art MEMS and microsystem tools for brain research. *Microsystems & Nanoengineering* **3**, 16066 (2017).

16. J. T. Mefford *et al.*, Correlative operando microscopy of oxygen evolution electrocatalysts. *Nature* **593**, 67-73 (2021).

17. A. Sood *et al.*, Electrochemical ion insertion from the atomic to the device scale. *Nature Reviews Materials* **6**, 847-867 (2021).

18. S. Maier, M. Salmeron, How Does Water Wet a Surface? *Accounts Chem Res* **48**, 2783-2790 (2015).

19. Y. Liu *et al.*, A highly efficient metal-free electrocatalyst of F-doped porous carbon toward N2 electroreduction. *Advanced Materials* **32**, 1907690 (2020).

20. M. Weiss *et al.*, From Liquid- to Solid-State Batteries: Ion Transfer Kinetics of Heteroionic Interfaces. *Electrochemical Energy Reviews* **3**, 221-238 (2020).

21. H. Liang, B. B. Laird, M. Asta, Y. Yang, In-plane characterization of structural and thermodynamic properties for steps at faceted chemically heterogeneous solid/liquid interfaces. *Acta Materialia* **143**, 329-337 (2018).

22. T. K. Shimizu, S. Maier, A. Verdaguer, J. J. Velasco-Velez, M. Salmeron, Water at surfaces and interfaces: From molecules to ice and bulk liquid. *Prog Surf Sci* **93**, 87-107 (2018).

23. M. A. van Spronsen *et al.*, Interfaces Sensitivity in Electron/Ion Yield X-ray Absorption Spectroscopy: The TiO2–H2O Interfaces. *The Journal of Physical Chemistry Letters* 10.1021/acs.jpclett.1c02115, 10212-10217 (2021).

24. B. Wen, A. Selloni, Hydrogen Bonds and H3O+ Formation at the Water Interfaces with Formic Acid Covered Anatase TiO2. *The Journal of Physical Chemistry Letters* **12**, 6840-6846 (2021).

25. I. M. Nadeem *et al.*, Water Dissociates at the Aqueous Interfaces with Reduced Anatase TiO2 (101). *The Journal of Physical Chemistry Letters* **9**, 3131-3136 (2018).

26. S. Hosseinpour *et al.*, Chemisorbed and physisorbed water at the TiO2/water interfaces. *The journal of physical chemistry letters* **8**, 2195-2199 (2017).

27. M. A. Henderson, A surface science perspective on TiO2 photocatalysis. *Surf Sci Rep* **66**, 185-297 (2011).

28. N. M. Adhikari, A. Tuladhar, Z. Wang, J. J. De Yoreo, K. M. Rosso, No Hydrogen Bonding between Water and Hydrophilic Single Crystal MgO Surfaces? *The Journal of Physical Chemistry C* **125**, 26132-26138 (2021).

29. B. A. Legg *et al.*, Visualization of Aluminum Ions at the Mica Water Interfaces Links Hydrolysis State-to-Surface Potential and Particle Adhesion. *J Am Chem Soc* **142**, 6093-6102 (2020).

30. S.-J. Shin *et al.*, A unifying mechanism for cation effect modulating C1 and C2 productions from CO2 electroreduction. *Nat Commun* **13** (2022).

31. S. Ringe *et al.*, Understanding cation effects in electrochemical CO₂ reduction. *Energy & Environmental Science* **12**, 3001-3014 (2019).

32. J. Resasco *et al.*, Promoter Effects of Alkali Metal Cations on the Electrochemical Reduction of Carbon Dioxide. *J Am Chem Soc* **139**, 11277-11287 (2017).

33. G. A. Kamat *et al.*, Acid anion electrolyte effects on platinum for oxygen and hydrogen electrocatalysis. *Communications Chemistry* **5** (2022).

34. J. Huang, M. Li, M. J. Eslamibidgoli, M. Eikerling, A. Groß, Cation Overcrowding Effect on the Oxygen Evolution Reaction. *JACS Au* **1**, 1752-1765 (2021).

35. B. Huang *et al.*, Cation- and pH-Dependent Hydrogen Evolution and Oxidation Reaction Kinetics. *JACS Au* **1**, 1674-1687 (2021).

36. L. D. Chen, Cations play an essential role in CO2 reduction. *Nat Catal* **4**, 641-642 (2021).

37. O. Karslıoğlu *et al.*, Prospects for the expansion of standing wave ambient pressure photoemission spectroscopy to reactions at elevated temperatures. *Journal of Vacuum Science & Technology A* **40**, 013207 (2022).

38. D. E. Starr, Z. Liu, M. Hävecker, A. Knop-Gericke, H. Bluhm, Investigation of solid/vapor interfaces using ambient pressure X-ray photoelectron spectroscopy. *Chemical Society Reviews* **42**, 5833 (2013).

39. D. Frank Ogletree, H. Bluhm, E. D. Hebenstreit, M. Salmeron, Photoelectron spectroscopy under ambient pressure and temperature conditions. *Nuclear Instruments and Methods in Physics Research Section A: Accelerators, Spectrometers, Detectors and Associated Equipment* **601**, 151-160 (2009).

40. H. Siegbahn, Electron spectroscopy for chemical analysis of liquids and solutions. *The Journal of Physical Chemistry* **89**, 897-909 (1985).

41. Z. Novotny *et al.*, Probing the solid–liquid interfaces with tender x rays: A new ambient-pressure x-ray photoelectron spectroscopy endstation at the Swiss Light Source. *Rev Sci Instrum* **91**, 023103 (2020).

42. M. Favaro *et al.*, Interfaces Science Using Ambient Pressure Hard X-ray Photoelectron Spectroscopy. *Surfaces* **2**, 78-99 (2019).

43. Y. Han *et al.*, Observing the electrochemical oxidation of Co metal at the solid/liquid interfaces using ambient pressure X-ray photoelectron spectroscopy. *The Journal of Physical Chemistry B* **122**, 666-671 (2018).

44. M. Favaro *et al.*, Understanding the oxygen evolution reaction mechanism on CoO x using operando ambient-pressure X-ray photoelectron spectroscopy. *J Am Chem Soc* **139**, 8960-8970 (2017).

45. S. G. Booth, A. M. Tripathi, I. Strashnov, R. A. W. Dryfe, A. S. Walton, The offset droplet: a new methodology for studying the solid/water interfaces using x-ray photoelectron spectroscopy. *Journal of Physics: Condensed Matter* **29**, 454001 (2017).

46. M. Favaro *et al.*, Unravelling the electrochemical double layer by direct probing of the solid/liquid interfaces. *Nat Commun* **7**, 1-8 (2016).

47. S. Axnanda *et al.*, Using “Tender” X-ray Ambient Pressure X-Ray Photoelectron Spectroscopy as A Direct Probe of Solid-Liquid Interfaces. *Sci Rep-Uk* **5**, 9788 (2015).

48. J.-J. Velasco-Vélez *et al.*, A comparative study of electrochemical cells for in situ x-ray spectroscopies in the soft and tender x-ray range. *Journal of Physics D: Applied Physics* **54**, 124003 (2021).

49. L. J. Falling *et al.*, Graphene-Capped Liquid Thin Films for Electrochemical Operando X-ray Spectroscopy and Scanning Electron Microscopy. *ACS Applied Materials & Interfaces* **12**, 37680-37692 (2020).

50. M. F. Tesch *et al.*, Evolution of Oxygen–Metal Electron Transfer and Metal Electronic States During Manganese Oxide Catalyzed Water Oxidation Revealed with In Situ Soft X-Ray Spectroscopy. *Angewandte Chemie International Edition* **58**, 3426-3432 (2019).

51. R. Mom *et al.*, The Oxidation of Platinum under Wet Conditions Observed by Electrochemical X-ray Photoelectron Spectroscopy. *J Am Chem Soc* **141**, 6537-6544 (2019).

52. L. J. Frevel *et al.*, In Situ X-ray Spectroscopy of the Electrochemical Development of Iridium Nanoparticles in Confined Electrolyte. *The Journal of Physical Chemistry C* **123**, 9146-9152 (2019).

53. R. S. Weatherup, B. Eren, Y. Hao, H. Bluhm, M. B. Salmeron, Graphene Membranes for Atmospheric Pressure Photoelectron Spectroscopy. *The Journal of Physical Chemistry Letters* **7**, 1622-1627 (2016).

54. J. J. Velasco-Vélez *et al.*, Atmospheric pressure X-ray photoelectron spectroscopy apparatus: Bridging the pressure gap. *Rev Sci Instrum* **87**, 053121 (2016).

55. J. J. Velasco-Velez *et al.*, Photoelectron Spectroscopy at the Graphene–Liquid Interfaces Reveals the Electronic Structure of an Electrodeposited Cobalt/Graphene Electrocatalyst. *Angewandte Chemie International Edition* **54**, 14554-14558 (2015).

56. O. Karslıoğlu *et al.*, Aqueous solution/metal interfaces investigated in operando by photoelectron spectroscopy. *Faraday Discuss* **180**, 35-53 (2015).

57. C. Baeumer *et al.*, Tuning electrochemically driven surface transformation in atomically flat LaNiO3 thin films for enhanced water electrolysis. *Nat Mater* **20**, 674-682 (2021).

58. J. Zegenhagen, "Applications of the X-Ray Standing Wave Technique in Physical Science Research". (Springer International Publishing, 2018), 10.1007/978-3-319-04507-8_66-1, pp. 1-31.

59. S. Nemšák *et al.*, Concentration and chemical-state profiles at heterogeneous interfaces with sub-nm accuracy from standing-wave ambient-pressure photoemission. *Nat Commun* **5**, 5441 (2014).

60. A. X. Gray, Future directions in standing-wave photoemission. *J Electron Spectrosc* **195**, 399-408 (2014).

61. F. Frati, M. O. Hunault, F. M. de Groot, Oxygen K-edge X-ray Absorption Spectra. *Chem Rev* **120**, 4056-4110 (2020).

62. J. W. Smith, R. J. Saykally, Soft x-ray absorption spectroscopy of liquids and solutions. *Chem Rev* **117**, 13909-13934 (2017).

63. R. Laskowski, P. Blaha, Understanding the L 2, 3 x-ray absorption spectra of early 3 d transition elements. *Phys Rev B* **82**, 205104 (2010).

64. M. Abbate *et al.*, Probing depth of soft x-ray absorption spectroscopy measured in total-electron-yield mode. *Surface and Interfaces Analysis* **18**, 65-69 (1992).

65. L. C. Kao *et al.*, In-situ/operando X-ray absorption spectroscopic investigation of the electrode/electrolyte interfaces on the molecular scale. *Surf Sci* **702**, 121720 (2020).

66. C. H. Wu *et al.*, Molecular-Scale Structure of Electrode-Electrolyte Interfaces: The Case of Platinum in Aqueous Sulfuric Acid. *J Am Chem Soc* **140**, 16237-16244 (2018).

67. C. H. Wu, R. S. Weatherup, M. B. Salmeron, Probing electrode/electrolyte interfaces in situ by X-ray spectroscopies: old methods, new tricks. *Phys Chem Chem Phys* **17**, 30229-30239 (2015).

68. J. J. Velasco-Velez *et al.*, The structure of interfacial water on gold electrodes studied by x-ray absorption spectroscopy. *Science* **346**, 831-834 (2014).

69. D. Schön *et al.*, Introducing Ionic-Current Detection for X-ray Absorption Spectroscopy in Liquid Cells. *The Journal of Physical Chemistry Letters* **8**, 2087-2092 (2017).

70. D. Schön *et al.*, Bulk-Sensitive Detection of the Total Ion Yield for X-ray Absorption Spectroscopy in Liquid Cells. *The Journal of Physical Chemistry Letters* **8**, 5136-5140 (2017).

71. C. S. Fadley, Hard X-ray photoemission with angular resolution and standing-wave excitation. *J Electron Spectrosc* **190**, 165-179 (2013).

72. P. Fenter *et al.*, Electrical double-layer structure at the rutile–water interfaces as observed in situ with small-period X-ray standing waves. *J Colloid Interf Sci* **225**, 154-165 (2000).

73. R. Signorell, Electron scattering in liquid water and amorphous ice: a striking resemblance. *Phys Rev Lett* **124**, 205501 (2020).

74. M. A. Flores-Mancera, J. S. Villarrubia, G. Massillon-JL, Electron Inelastic Mean Free Paths for LiF, CaF2, Al2O3, and Liquid Water from 433 keV down to the Energy Gap. *ACS omega* **5**, 4139-4147 (2020).

75. H. Shinotsuka *et al.*, Calculations of electron inelastic mean free paths. XI. Data for liquid water for energies from 50 eV to 30 keV. *Surface and Interfaces Analysis* **49**, 238-252 (2017).

76. Y.-I. Suzuki, K. Nishizawa, N. Kurahashi, T. Suzuki, Effective attenuation length of an electron in liquid water between 10 and 600 eV. *Phys Rev E* **90**, 010302 (2014).

77. M. Moradzaman, G. Mul, Infrared Analysis of Interfacial Phenomena during Electrochemical Reduction of CO2 over Polycrystalline Copper Electrodes. *Acs Catal* **10**, 8049-8057 (2020).

78. T. Yajima, H. Uchida, M. Watanabe, In-Situ ATR-FTIR Spectroscopic Study of Electro-oxidation of Methanol and Adsorbed CO at Pt−Ru Alloy. *The Journal of Physical Chemistry B* **108**, 2654-2659 (2004).

79. M. Milosevic, Internal reflection and ATR spectroscopy. *Applied Spectroscopy Reviews* **39**, 365-384 (2004).

80. N. Harrick, K. Beckmann, "Internal reflection spectroscopy" in Characterization of solid surfaces. (Springer, 1974), pp. 215-245.

81. A. Götz, R. Nikzad-Langerodi, Y. Staedler, A. Bellaire, J. Saukel, Apparent penetration depth in attenuated total reflection Fourier-transform infrared (ATR-FTIR) spectroscopy of Allium cepa L. epidermis and cuticle. *Spectrochimica Acta Part A: Molecular and Biomolecular Spectroscopy* **224**, 117460 (2020).

82. B. Yang *et al.*, Accelerating CO₂ Electroreduction to Multicarbon Products via Synergistic Electric–Thermal Field on Copper Nanoneedles. *J Am Chem Soc* **144**, 3039-3049 (2022).

83. G. Zhang *et al.*, Efficient CO2 electroreduction on facet-selective copper films with high conversion rate. *Nat Commun* **12** (2021).

84. J.-E. Lee *et al.*, In situ FTIR study of CO2 reduction on inorganic analogues of carbon monoxide dehydrogenase. *Chem Commun* **57**, 3267-3270 (2021).

85. A. Bieberle-Hütter, A. Bronneberg, K. George, M. van de Sanden, Operando attenuated total reflection Fourier-transform infrared (ATR-FTIR) spectroscopy for water splitting. *Journal of Physics D: Applied Physics* **54**, 133001 (2021).

86. S. Yang *et al.*, Nature of the Electrical Double Layer on Suspended Graphene Electrodes. *J Am Chem Soc* **144**, 13327-13333 (2022).

87. A. Montenegro *et al.*, Asymmetric response of interfacial water to applied electric fields. *Nature* **594**, 62-65 (2021).

88. Y. Zhang, H. B. De Aguiar, J. T. Hynes, D. Laage, Water Structure, Dynamics, and Sum-Frequency Generation Spectra at Electrified Graphene Interfaces. *The Journal of Physical Chemistry Letters* **11**, 624-631 (2020).

89. T. Ohto, H. Tada, Y. Nagata, Structure and dynamics of water at water–graphene and water–hexagonal boron-nitride sheet interfaces revealed by ab initio sum-frequency generation spectroscopy. *Phys Chem Chem Phys* **20**, 12979-12985 (2018).

90. J. Schaefer, G. Gonella, M. Bonn, E. H. G. Backus, Surface-specific vibrational spectroscopy of the water/silica interfaces: screening and interference. *Phys Chem Chem Phys* **19**, 16875-16880 (2017).

91. P. E. Ohno, H.-F. Wang, F. M. Geiger, Second-order spectral lineshapes from charged interfaces. *Nat Commun* **8** (2017).

92. Y.-C. Wen *et al.*, Unveiling Microscopic Structures of Charged Water Interfaces by Surface-Specific Vibrational Spectroscopy. *Phys Rev Lett* **116** (2016).

93. G. Gonella, C. Lütgebaucks, A. G. F. De Beer, S. Roke, Second Harmonic and Sum-Frequency Generation from Aqueous Interfaces Is Modulated by Interference. *The Journal of Physical Chemistry C* **120**, 9165-9173 (2016).

94. I. V. Stiopkin *et al.*, Hydrogen bonding at the water surface revealed by isotopic dilution spectroscopy. *Nature* **474**, 192-195 (2011).

95. H. J. Bakker, J. L. Skinner, Vibrational Spectroscopy as a Probe of Structure and Dynamics in Liquid Water. *Chem Rev* **110**, 1498-1517 (2010).

96. S. Nihonyanagi, S. Yamaguchi, T. Tahara, Direct evidence for orientational flip-flop of water molecules at charged interfaces: A heterodyne-detected vibrational sum frequency generation study. *The Journal of Chemical Physics* **130**, 204704 (2009).

97. Q. Du, E. Freysz, Y. R. Shen, Vibrational spectra of water molecules at quartz/water interfaces. *Phys Rev Lett* **72**, 238-241 (1994).

98. S. Ong, X. Zhao, K. B. Eisenthal, Polarization of water molecules at a charged interfaces: second harmonic studies of the silica/water interfaces. *Chem Phys Lett* **191**, 327-335 (1992).

99. Y. R. Shen, Surface properties probed by second-harmonic and sum-frequency generation. *Nature* **337**, 519-525 (1989).

100. O. Mermut *et al.*, Directions in peptide interfacial science. *Biointerphases* **1**, P5-P11 (2006).

101. K. C. Jena, P. A. Covert, D. K. Hore, The Effect of Salt on the Water Structure at a Charged Solid Surface: Differentiating Second- and Third-order Nonlinear Contributions. *The Journal of Physical Chemistry Letters* **2**, 1056-1061 (2011).

102. C. S. Tian, Y. R. Shen, Structure and charging of hydrophobic material/water interfaces studied by phase-sensitive sum-frequency vibrational spectroscopy. *Proceedings of the National Academy of Sciences* **106**, 15148-15153 (2009).

103. A. Eftekhari-Bafrooei, E. Borguet, Effect of Surface Charge on the Vibrational Dynamics of Interfacial Water. *J Am Chem Soc* **131**, 12034-12035 (2009).

104. M. S. Yeganeh, S. M. Dougal, H. S. Pink, Vibrational Spectroscopy of Water at Liquid/Solid Interfaces: Crossing the Isoelectric Point of a Solid Surface. *Phys Rev Lett* **83**, 1179-1182 (1999).

105. D. E. Gragson, G. L. Richmond, Potential Dependent Alignment and Hydrogen Bonding of Water Molecules at Charged Air/Water and CCl₄/Water Interfaces. *J Am Chem Soc* **120**, 366-375 (1998).

106. C. P. Schwartz *et al.*, Angstrom-Resolved Interfacial Structure in Buried Organic-Inorganic Junctions. *Phys Rev Lett* **127** (2021).

107. E. Berger *et al.*, Extreme Ultraviolet Second Harmonic Generation Spectroscopy in a Polar Metal. *Nano Lett* **21**, 6095-6101 (2021).

108. A. Nilsson, X-Ray Probe Targets Interfaces. *Physics* **11**, 2 (2018).

109. R. K. Lam *et al.*, Soft X-Ray Second Harmonic Generation as an Interfacial Probe. *Phys Rev Lett* **120** (2018).

110. H.-L. Wang, E.-M. You, R. Panneerselvam, S.-Y. Ding, Z.-Q. Tian, Advances of surface-enhanced Raman and IR spectroscopies: from nano/microstructures to macro-optical design. *Light: Science & Applications* **10** (2021).

111. Y. Wang, D. Chen, Application of Advanced Vibrational Spectroscopy in Revealing Critical Chemical Processes and Phenomena of Electrochemical Energy Storage and Conversion. *ACS Applied Materials & Interfaces* **14**, 23033-23055 (2022).

112. T. J. Blackburn, S. M. Tyler, J. E. Pemberton, Optical Spectroscopy of Surfaces, Interfaces, and Thin Films. *Analytical Chemistry* 10.1021/acs.analchem.1c05323 (2022).

113. B.-Y. Wen *et al.*, In Situ Surface-Enhanced Raman Spectroscopy Characterization of Electrocatalysis with Different Nanostructures. *Annual Review of Physical Chemistry* **72**, 331-351 (2021).

114. K. E. Watts, T. J. Blackburn, J. E. Pemberton, Optical Spectroscopy of Surfaces, Interfaces, and Thin Films: A Status Report. *Analytical Chemistry* **91**, 4235-4265 (2019).

115. B. Knoll, F. Keilmann, Near-field probing of vibrational absorption for chemical microscopy. *Nature* **399**, 134-137 (1999).

116. G. A. Massey, J. A. Davis, S. Katnik, E. Omon, Subwavelength resolution far-infrared microscopy. *Applied optics* **24**, 1498-1501 (1985).

117. A. Hartstein, J. R. Kirtley, J. C. Tsang, Enhancement of the Infrared Absorption from Molecular Monolayers with Thin Metal Overlayers. *Phys Rev Lett* **45**, 201-204 (1980).

118. M. Moskovits, Surface roughness and the enhanced intensity of Raman scattering by molecules adsorbed on metals. *The Journal of Chemical Physics* **69**, 4159-4161 (1978).

119. D. L. Jeanmaire, R. P. Van Duyne, Surface Raman spectroelectrochemistry: Part I. Heterocyclic, aromatic, and aliphatic amines adsorbed on the anodized silver electrode. *Journal of electroanalytical chemistry and interfacial electrochemistry* **84**, 1-20 (1977).

120. M. Fleischmann, P. J. Hendra, A. J. McQuillan, Raman spectra of pyridine adsorbed at a silver electrode. *Chem Phys Lett* **26**, 163-166 (1974).

121. K. A. Willets, R. P. Van Duyne, Localized Surface Plasmon Resonance Spectroscopy and Sensing. *Annual Review of Physical Chemistry* **58**, 267-297 (2007).

122. R. Rojas, F. Claro, Theory of surface enhanced Raman scattering in colloids. *The Journal of Chemical Physics* **98**, 998-1006 (1993).

123. D. Wang, M. Kerker, H. Chew, Surface enhanced Raman scattering (SERS) by molecules adsorbed at spherical particles: errata. *Appl. Opt* **19**, 4159 (1980).

124. Z.-C. Zeng *et al.*, Electrochemical Tip-Enhanced Raman Spectroscopy. *J Am Chem Soc* **137**, 11928-11931 (2015).

125. S. Nie, S. R. Emory, Probing single molecules and single nanoparticles by surface-enhanced Raman scattering. *Science* **275**, 1102-1106 (1997).

126. F. Shao *et al.*, In situ spectroelectrochemical probing of CO redox landscape on copper single-crystal surfaces. *Proceedings of the National Academy of Sciences* **119** (2022).

127. A. Wagner *et al.*, Host–Guest Chemistry Meets Electrocatalysis: Cucurbit[6]uril on a Au Surface as a Hybrid System in CO2 Reduction. *Acs Catal* **10**, 751-761 (2020).

128. K. Yang, R. Kas, W. A. Smith, In Situ Infrared Spectroscopy Reveals Persistent Alkalinity near Electrode Surfaces during CO2 Electroreduction. *J Am Chem Soc* **141**, 15891-15900 (2019).

129. S. Zhu, B. Jiang, W.-B. Cai, M. Shao, Direct Observation on Reaction Intermediates and the Role of Bicarbonate Anions in CO₂ Electrochemical Reduction Reaction on Cu Surfaces. *J Am Chem Soc* **139**, 15664-15667 (2017).

130. M. Dunwell *et al.*, The Central Role of Bicarbonate in the Electrochemical Reduction of Carbon Dioxide on Gold. *J Am Chem Soc* **139**, 3774-3783 (2017).

131. J. F. Li *et al.*, Shell-isolated nanoparticle-enhanced Raman spectroscopy. *Nature* **464**, 392-395 (2010).

132. C.-Y. Li *et al.*, In situ probing electrified interfacial water structures at atomically flat surfaces. *Nat Mater* **18**, 697-701 (2019).

133. J.-C. Dong *et al.*, Direct <i>In Situ</i> Raman Spectroscopic Evidence of Oxygen Reduction Reaction Intermediates at High-Index Pt(<i>hkl</i>) Surfaces. *J Am Chem Soc* **142**, 715-719 (2020).

134. H. A. Bechtel, S. C. Johnson, O. Khatib, E. A. Muller, M. B. Raschke, Synchrotron infrared nano-spectroscopy and-imaging. *Surf Sci Rep*, 100493 (2020).

135. A. V. Zayats, D. Richards, *Nano-optics and near-field optical microscopy* (Artech House, 2009).

136. H. A. Bechtel, E. A. Muller, R. L. Olmon, M. C. Martin, M. B. Raschke, Ultrabroadband infrared nanospectroscopic imaging. *Proceedings of the National Academy of Sciences* **111**, 7191-7196 (2014).

137. S. Berweger *et al.*, Nano-Chemical Infrared Imaging of Membrane Proteins in Lipid Bilayers. *J Am Chem Soc* **135**, 18292-18295 (2013).

138. I. Amenabar *et al.*, Structural analysis and mapping of individual protein complexes by infrared nanospectroscopy. *Nat Commun* **4**, 2890 (2013).

139. F. Huth *et al.*, Nano-FTIR Absorption Spectroscopy of Molecular Fingerprints at 20 nm Spatial Resolution. *Nano Lett* **12**, 3973-3978 (2012).

140. F. Mooshammer *et al.*, Quantifying Nanoscale Electromagnetic Fields in Near-Field Microscopy by Fourier Demodulation Analysis. *ACS Photonics* **7**, 344-351 (2020).

141. A. Cvitkovic, N. Ocelic, R. Hillenbrand, Analytical model for quantitative prediction of material contrasts in scattering-type near-field optical microscopy. *Opt Express* **15**, 8550-8565 (2007).

142. X. He, J. M. Larson, H. A. Bechtel, R. Kostecki, In situ infrared nanospectroscopy of the local processes at the Li/polymer electrolyte interfaces. *Nat Commun* **13**, 1398 (2022).

143. F. S. Ruggeri, B. Mannini, R. Schmid, M. Vendruscolo, T. P. Knowles, Single molecule secondary structure determination of proteins through infrared absorption nanospectroscopy. *Nat Commun* **11**, 1-9 (2020).

144. L. Mester, A. A. Govyadinov, S. Chen, M. Goikoetxea, R. Hillenbrand, Subsurface chemical nanoidentification by nano-FTIR spectroscopy. *Nat Commun* **11**, 1-10 (2020).

145. C. W. Machan, Spectroelectrochemistry: Tools for Electrochemical Mechanisms and Electrocatalysis. (2021).

146. J. J. A. Lozeman, P. Führer, W. Olthuis, M. Odijk, Spectroelectrochemistry, the future of visualizing electrode processes by hyphenating electrochemistry with spectroscopic techniques. *The Analyst* **145**, 2482-2509 (2020).

147. A. C. VD dos Santos *et al.*, Nanoscale Infrared Spectroscopy and Chemometrics Enable Detection of Intracellular Protein Distribution. *Analytical chemistry* **92**, 15719-15725 (2020).

148. G. X. Ni *et al.*, Nanoscale Infrared Spectroscopy and Imaging of Catalytic Reactions in Cu₂O Crystals. *ACS Photonics* **7**, 576-580 (2020).

149. F. Sterl *et al.*, Nanoscale Hydrogenography on Single Magnesium Nanoparticles. *Nano Lett* **18**, 4293-4302 (2018).

150. C.-Y. Wu *et al.*, High-spatial-resolution mapping of catalytic reactions on single particles. *Nature* **541**, 511-515 (2017).

151. E. Pfitzner, J. Heberle, Infrared Scattering-Type Scanning Near-Field Optical Microscopy of Biomembranes in Water. *The Journal of Physical Chemistry Letters* **11**, 8183-8188 (2020).

152. B. T. O'Callahan *et al.*, In liquid infrared scattering scanning near-field optical microscopy for chemical and biological nanoimaging. *Nano Lett* **20**, 4497-4504 (2020).

153. X. Zhao *et al.*, In vitro investigation of protein assembly by combined microscopy and infrared spectroscopy at the nanometer scale. *Proceedings of the National Academy of Sciences* **119** (2022).

154. L. Meireles *et al.*, Synchrotron infrared nanospectroscopy on a graphene chip. *Lab on a Chip* (2019).

155. Y.-H. Lu *et al.*, Infrared Nanospectroscopy at the Graphene-Electrolyte Interfaces. *Nano Lett* (2019).

156. O. Khatib *et al.*, Graphene-Based Platform for Infrared Near-Field Nanospectroscopy of Water and Biological Materials in an Aqueous Environment. *Acs Nano* **9**, 7968-7975 (2015).

157. D. Krotkov *et al.*, <i>Operando</i> Terahertz Spectroscopy of Solid Electrolyte Interphase Evolution on Silicon Anodes. *Batteries & Supercaps* **5** (2022).

158. S. R. Alfarano *et al.*, Stripping away ion hydration shells in electrical double-layer formation: Water networks matter. *Proceedings of the National Academy of Sciences* **118** (2021).

159. C. T. Nemes, J. R. Swierk, C. A. Schmuttenmaer, A Terahertz-Transparent Electrochemical Cell for In Situ Terahertz Spectroelectrochemistry. *Analytical Chemistry* **90**, 4389-4396 (2018).

160. J. Hasted, S. Husain, F. Frescura, J. Birch, Far-infrared absorption in liquid water. *Chem Phys Lett* **118**, 622-625 (1985).

161. A. Beer, R. Damari, Y. Chen, S. Fleischer, Molecular Orientation-Induced Second-Harmonic Generation: Deciphering Different Contributions Apart. *The Journal of Physical Chemistry A* **126**, 3732-3738 (2022).

162. S. B. Bodrov *et al.*, Terahertz-field-induced second harmonic generation for nonlinear optical detection of interfaces buried in transparent materials. *Appl Phys Lett* **119**, 221109 (2021).

163. D. Cook, J. Chen, E. Morlino, R. Hochstrasser, Terahertz-field-induced second-harmonic generation measurements of liquid dynamics. *Chem Phys Lett* **309**, 221-228 (1999).

164. G. Schwaab, F. Sebastiani, M. Havenith, Ion Hydration and Ion Pairing as Probed by THz Spectroscopy. *Angewandte Chemie International Edition* **58**, 3000-3013 (2019).

165. S. Zhu, T. Li, W.-B. Cai, M. Shao, CO2 Electrochemical Reduction As Probed through Infrared Spectroscopy. *ACS Energy Letters* **4**, 682-689 (2019).

166. L. Bouffier, D. Zigah, N. Sojic, A. Kuhn, *Encyclopedia of electrochemistry* (Wiley, 2007).

167. E. R. Corson *et al.*, In Situ ATR–SEIRAS of Carbon Dioxide Reduction at a Plasmonic Silver Cathode. *J Am Chem Soc* **142**, 11750-11762 (2020).

168. D. Moss, E. Nabedryk, J. Breton, W. Mantele, Redox-linked conformational changes in proteins detected by a combination of infrared spectroscopy and protein electrochemistry: Evaluation of the technique with cytochrome c. *European Journal of Biochemistry* **187**, 565-572 (1990).

169. D. J. Chen, Y. Y. J. Tong, In situ Raman spectroscopic measurement of near-surface proton concentration changes during electrochemical reactions. *Chem Commun* **51**, 5683-5686 (2015).

170. S. Yang *et al.*, Chloride-Assisted Corrosion of Copper and Protection by Benzotriazole. *Acs Appl Mater Inter* 10.1021/acsami.1c15808 (2022).

171. M. A. Brown *et al.*, Determination of Surface Potential and Electrical Double-Layer Structure at the Aqueous Electrolyte-Nanoparticle Interfaces. *Physical Review X* **6** (2016).

172. C. H. Wu *et al.*, Molecular-Scale Structure of Electrode-Electrolyte Interfaces: The Case of Platinum in Aqueous Sulfuric Acid. *J Am Chem Soc* **140**, 16237-16244 (2018).

173. T. Masuda *et al.*, <i>In situ</i> x-ray photoelectron spectroscopy for electrochemical reactions in ordinary solvents. *Appl Phys Lett* **103**, 111605 (2013).

174. J. M. Yuk *et al.*, High-resolution EM of colloidal nanocrystal growth using graphene liquid cells. *Science* **336**, 61-64 (2012).

175. A. Kolmakov *et al.*, Graphene oxide windows for in situ environmental cell photoelectron spectroscopy. *Nature Nanotechnology* **6**, 651-657 (2011).

176. R. S. Weatherup, C. H. Wu, C. Escudero, V. Perez-Dieste, M. B. Salmeron, Environment-Dependent Radiation Damage in Atmospheric Pressure X-ray Spectroscopy. *J Phys Chem B* **122**, 737-744 (2018).

177. J. Qian, A. Baskin, Z. Liu, D. Prendergast, E. J. Crumlin, Addressing the sensitivity of signals from solid/liquid ambient pressure XPS (APXPS) measurement. *The Journal of Chemical Physics* **153**, 044709 (2020).

178. B.-O. Shalom, M. A. Andrés, Y. Yu, A. R. Head, B. Eren, Electrochemically controlled solid liquid interfaces probed with lab-based X-ray photoelectron spectroscopy. *Electrochem Commun* **142**, 107375 (2022).

179. S. Nemšák *et al.*, Interfacial Electrochemistry in Liquids Probed with Photoemission Electron Microscopy. *J Am Chem Soc* **139**, 18138-18141 (2017).

180. P. Paengnakorn *et al.*, Infrared spectroscopy of the nitrogenase MoFe protein under electrochemical control: potential-triggered CO binding. *Chemical Science* **8**, 1500-1505 (2017).

181. Y.-H. Lu *et al.*, Ultra-thin Free-Standing Oxide Membranes for Electron and Photon Spectroscopy Studies of Solid-gas and Solid-liquid Interfaces. *Nano Lett* 10.1021/acs.nanolett.0c01801 (2020).

182. L. D. Wang *et al.*, Ultrathin Oxide Films by Atomic Layer Deposition on Graphene. *Nano Lett* **12**, 3706-3710 (2012).

183. C. H. Cao *et al.*, Role of graphene in enhancing the mechanical properties of TiO2/graphene heterostructures. *Nanoscale* **9**, 11678-11684 (2017).

184. M. Munther *et al.*, Probing the mechanical properties of vertically-stacked ultrathin graphene/Al2O3 heterostructures. *Nanotechnology* **30** (2019).

185. S. M. George, Atomic Layer Deposition: An Overview. *Chem Rev* **110**, 111-131 (2010).

186. S. Singh, H. Mahalingam, P. K. Singh, Polymer-supported titanium dioxide photocatalysts for environmental remediation: A review. *Appl Catal a-Gen* **462**, 178-195 (2013).

187. H. B. Profijt, S. E. Potts, M. C. M. van de Sanden, W. M. M. Kessels, Plasma-Assisted Atomic Layer Deposition: Basics, Opportunities, and Challenges. *J Vac Sci Technol A* **29** (2011).

188. L. G. Gosset *et al.*, Interfaces and material characterization of thin Al2O3 layers deposited by ALD using TMA/H2O. *J Non-Cryst Solids* **303**, 17-23 (2002).

189. J. Haeberle *et al.*, Ellipsometry and XPS comparative studies of thermal and plasma enhanced atomic layer deposited Al2O3-films. *Beilstein J Nanotech* **4**, 732-742 (2013).

190. R. Simpson, R. G. White, J. F. Watts, M. A. Baker, XPS investigation of monatomic and cluster argon ion sputtering of tantalum pentoxide. *Appl Surf Sci* **405**, 79-87 (2017).

191. C. Lee, X. D. Wei, J. W. Kysar, J. Hone, Measurement of the elastic properties and intrinsic strength of monolayer graphene. *Science* **321**, 385-388 (2008).

192. N. de Jonge, F. M. Ross, Electron microscopy of specimens in liquid. *Nat Nanotechnol* **6**, 695-704 (2011).

193. E. A. Ring, D. B. Peckys, M. J. Dukes, J. P. Baudoin, N. de Jonge, Silicon nitride windows for electron microscopy of whole cells. *Journal of Microscopy* **243**, 273-283 (2011).

194. J. H. Guo *et al.*, X-ray emission spectroscopy of hydrogen bonding and electronic structure of liquid water. *Phys Rev Lett* **89** (2002).

195. O. Fuchs *et al.*, A liquid flow cell to study the electronic structure of liquids with soft X-rays. *Nucl Instrum Meth A* **585**, 172-177 (2008).

196. R. S. Weatherup, B. Eren, Y. B. Hao, H. Bluhm, M. B. Salmeron, Graphene Membranes for Atmospheric Pressure Photoelectron Spectroscopy. *J Phys Chem Lett* **7**, 1622-1627 (2016).

197. J. Hedman, P. F. Heden, C. Nordling, K. Siegbahn, Energy Splitting of Core Electron Levels in Paramagnetic Molecules. *Phys Lett A* **A 29**, 178-& (1969).

198. T. G. Avval *et al.*, Oxygen gas, O-2(g), by near-ambient pressure XPS. *Surf Sci Spectra* **26** (2019).

199. Y. Horowitz, H.-L. Han, P. N. Ross, G. A. Somorjai, In Situ Potentiodynamic Analysis of the Electrolyte/Silicon Electrodes Interfaces Reactions - A Sum Frequency Generation Vibrational Spectroscopy Study. *J. Am. Chem. Soc.* **138**, 726-729 (2016).

200. A. Abrashkin, D. Andelman, H. Orland, Dipolar Poisson-Boltzmann Equation: Ions and Dipoles Close to Charge Interfaces. *Phys. Rev. Lett.* **99**, 077801 (2007).

201. I. Borukhov, D. Andelman, H. Orland, Steric Effects in Electrolytes: A Modified Poisson-Boltzmann Equation. *Phys. Rev. Lett.* **79**, 435-438 (1997).

202. B. E. Conway, J. O. M. Bockris, I. A. Ammar, The dielectric constant of the solution in the diffuse and Helmholtz double layers at a charged interfaces in aqueous solution. *Transactions of the Faraday Society* **47**, 756 (1951).

203. D. C. Grahame, The Electrical Double Layer and the Theory of Electrocapillarity. *Chem Rev* **41**, 441-501 (1947).

204. O. Stern, Zur theorie der elektrolytischen doppelschicht. *Zeitschrift für Elektrochemie und angewandte physikalische Chemie* **30**, 508-516 (1924).

205. P. Debye, E. Hückel, De la theorie des electrolytes. I. abaissement du point de congelation et phenomenes associes. *Physikalische Zeitschrift* **24**, 185-206 (1923).

206. D. L. Chapman, LI. <i>A contribution to the theory of electrocapillarity</i>. *The London, Edinburgh, and Dublin Philosophical Magazine and Journal of Science* **25**, 475-481 (1913).

207. M. Gouy, Sur la constitution de la charge électrique à la surface d'un électrolyte. *Journal de Physique Théorique et Appliquée* **9**, 457-468 (1910).

208. H. Helmholtz, Studien über electrische Grenzschichten. *Annalen der Physik und Chemie* **243**, 337-382 (1879).

209. H. Helmholtz, Ueber einige Gesetze der Vertheilung elektrischer Ströme in körperlichen Leitern mit Anwendung auf die thierisch-elektrischen Versuche. *Annalen der Physik und Chemie* **165**, 211-233 (1853).

210. J. Wu, Understanding the Electric Double-Layer Structure, Capacitance, and Charging Dynamics. *Chem Rev* **122**, 10821-10859 (2022).

211. K. Ojha, K. Doblhoff-Dier, M. T. Koper, Double-layer structure of the Pt (111)–aqueous electrolyte interfaces. *Proceedings of the National Academy of Sciences* **119** (2022).

212. M. J. Lisanne Knijff, Chao Zhang, Electric Double Layer at the Metal-Oxide/Electrolyte Interfaces. *arXiv* 10.48550/arxiv.2203.05486 (2022).

213. P. Li, Y. Liu, S. Chen, Microscopic EDL structures and charge–potential relation on stepped platinum surface: Insights from the <i>ab initio</i> molecular dynamics simulations. *The Journal of Chemical Physics* **156**, 104701 (2022).

214. O. Björneholm *et al.*, Water at interfaces. *Chemical reviews* **116**, 7698-7726 (2016).

215. G. A. Attard, A. Brew, K. Hunter, J. Sharman, E. Wright, Specific adsorption of perchlorate anions on Pt{hkl} single crystal electrodes. *Phys. Chem. Chem. Phys.* **16**, 13689-13698 (2014).

216. P. Li *et al.*, Hydrogen bond network connectivity in the electric double layer dominates the kinetic pH effect in hydrogen electrocatalysis on Pt. *Nat Catal* **5**, 900-911 (2022).

217. A. Gupta, H. A. Stone, Electrical Double Layers: Effects of Asymmetry in Electrolyte Valence on Steric Effects, Dielectric Decrement, and Ion–Ion Correlations. *Langmuir* **34**, 11971-11985 (2018).

218. S. Das, S. Chakraborty, Steric-effect-induced enhancement of electrical-double-layer overlapping phenomena. *Phys Rev E* **84** (2011).

219. A. Sugahara *et al.*, Negative dielectric constant of water confined in nanosheets. *Nat Commun* **10**, 1-7 (2019).

220. M. D. Boamah, P. E. Ohno, F. M. Geiger, K. B. Eisenthal, Relative permittivity in the electrical double layer from nonlinear optics. *The Journal of Chemical Physics* **148**, 222808 (2018).

221. Y. Uematsu, R. R. Netz, D. J. Bonthuis, Analytical Interfacial Layer Model for the Capacitance and Electrokinetics of Charged Aqueous Interfaces. *Langmuir* **34**, 9097-9113 (2018).

222. B. Rehl *et al.*, Water Structure in the Electrical Double Layer and the Contributions to the Total Interfacial Potential at Different Surface Charge Densities. *J Am Chem Soc* **144**, 16338-16349 (2022).

223. J.-B. Le, Q.-Y. Fan, J.-Q. Li, J. Cheng, Molecular origin of negative component of Helmholtz capacitance at electrified Pt (111)/water interfaces. *Science advances* **6**, eabb1219 (2020).

224. J. Huang, A. Malek, J. Zhang, M. H. Eikerling, Non-monotonic Surface Charging Behavior of Platinum: A Paradigm Change. *The Journal of Physical Chemistry C* **120**, 13587-13595 (2016).

225. M. M. Melander, Grand canonical ensemble approach to electrochemical thermodynamics, kinetics, and model Hamiltonians. *Current Opinion in Electrochemistry* **29**, 100749 (2021).

226. B. Mi, Scaling up nanoporous graphene membranes. *Science* **364**, 1033 (2019).

227. L. A. Belyaeva, G. F. Schneider, Wettability of graphene. *Surf. Sci. Rep.* **75**, 100482 (2020).

228. J. Yin *et al.*, Generating electricity by moving a droplet of ionic liquid along graphene. *Nat. Nanotechnol.* **9**, 378-383 (2014).

229. J. Yin *et al.*, Waving potential in graphene. *Nat. Commun.* **5**, 3582 (2014).

230. S. Yang *et al.*, Mechanism of Electric Power Generation from Ionic Droplet Motion on Polymer Supported Graphene. *J. Am. Chem. Soc.* **140**, 13746-13752 (2018).

231. Z. Zhang *et al.*, Emerging hydrovoltaic technology. *Nat. Nanotechnol.* **13**, 1109-1119 (2018).

232. S. Garaj *et al.*, Graphene as a subnanometre trans-electrode membrane. *Nature* **467**, 190-193 (2010).

233. I. Heller *et al.*, Influence of Electrolyte Composition on Liquid-Gated Carbon Nanotube and Graphene Transistors. *J. Am. Chem. Soc.* **132**, 17149-17156 (2010).

234. P. K. Ang, W. Chen, A. T. S. Wee, K. P. Loh, Solution-Gated Epitaxial Graphene as pH Sensor. *J. Am. Chem. Soc.* **130**, 14392-14393 (2008).

235. Y. Ohno, K. Maehashi, Y. Yamashiro, K. Matsumoto, Electrolyte-Gated Graphene Field-Effect Transistors for Detecting pH and Protein Adsorption. *Nano Lett.* **9**, 3318-3322 (2009).

236. F. Traversi *et al.*, Detecting the translocation of DNA through a nanopore using graphene nanoribbons. *Nat. Nanotechnol.* **8**, 939-945 (2013).

237. S. J. Heerema, C. Dekker, Graphene nanodevices for DNA sequencing. *Nat. Nanotechnol.* **11**, 127-136 (2016).

238. W. Fu *et al.*, Biosensing near the neutrality point of graphene. *Science Advances* **3**, e1701247 (2017).

239. W. Fu, L. Jiang, E. P. van Geest, L. M. C. Lima, G. F. Schneider, Sensing at the Surface of Graphene Field-Effect Transistors. *Adv. Mater.* **29**, 1603610 (2017).

240. R. Garcia-Cortadella *et al.*, Graphene active sensor arrays for long-term and wireless mapping of wide frequency band epicortical brain activity. *Nat. Commun.* **12**, 211 (2021).

241. M. Pykal, M. Langer, B. Blahová Prudilová, P. Banáš, M. Otyepka, Ion Interactions across Graphene in Electrolyte Aqueous Solutions. *J. Phys. Chem. C* **123**, 9799-9806 (2019).

242. C. D. Williams, J. Dix, A. Troisi, P. Carbone, Effective Polarization in Pairwise Potentials at the Graphene–Electrolyte Interfaces. *J. Phys. Chem. Lett.* **8**, 703-708 (2017).

243. X. Jia *et al.*, Kinetic Ionic Permeation and Interfacial Doping of Supported Graphene. *Nano Lett.* **19**, 9029-9036 (2019).

244. Y.-H. Lu *et al.*, Infrared nanospectroscopy at the graphene–electrolyte interfaces. *Nano Lett.* **19**, 5388-5393 (2019).

245. M. A. Brown, M. S. Crosser, A. C. Ulibarri, C. V. Fengel, E. D. Minot, Hall Effect Measurements of the Double-Layer Capacitance of the Graphene–Electrolyte Interfaces. *J. Phys. Chem. C* **123**, 22706-22710 (2019).

246. D. J. Cole, P. K. Ang, K. P. Loh, Ion Adsorption at the Graphene/Electrolyte Interfaces. *J. Phys. Chem. Lett.* **2**, 1799-1803 (2011).

247. T. A. Pascal, W. A. Goddard, Entropic Stabilization of Water at Graphitic Interfaces. *J. Phys. Chem. Lett.* **12**, 9162-9168 (2021).

248. M. D. Baer, I. F. W. Kuo, D. J. Tobias, C. J. Mundy, Toward a Unified Picture of the Water Self-Ions at the Air–Water Interfaces: A Density Functional Theory Perspective. *J. Phys. Chem. B* **118**, 8364-8372 (2014).

249. S. Gopalakrishnan, P. Jungwirth, D. J. Tobias, H. C. Allen, Air−Liquid Interfaces of Aqueous Solutions Containing Ammonium and Sulfate: Spectroscopic and Molecular Dynamics Studies. *J. Phys. Chem. B* **109**, 8861-8872 (2005).

250. Y.-C. Wen *et al.*, Unveiling Microscopic Structures of Charged Water Interfaces by Surface-Specific Vibrational Spectroscopy. *Phys. Rev. Lett.* **116**, 016101 (2016).

251. F. Thaunay, C. Clavaguéra, G. Ohanessian, Hydration of the sulfate dianion in cold nanodroplets: SO42−(H2O)12 and SO42−(H2O)13. *Phys. Chem. Chem. Phys.* **17**, 25935-25945 (2015).

252. T. I. Yacovitch *et al.*, Infrared Spectroscopy of Hydrated Bisulfate Anion Clusters: HSO4¯(H2O)1–16. *J. Phys. Chem. Lett.* **2**, 2135-2140 (2011).

253. J. Zhou *et al.*, Infrared spectroscopy of hydrated sulfate dianions. *J. Chem. Phys.* **125**, 111102 (2006).

254. N. Ji, V. Ostroverkhov, C. S. Tian, Y. R. Shen, Characterization of Vibrational Resonances of Water-Vapor Interfaces by Phase-Sensitive Sum-Frequency Spectroscopy. *Phys. Rev. Lett.* **100**, 096102 (2008).

255. T. Ohto, H. Tada, Y. Nagata, Structure and dynamics of water at water–graphene and water–hexagonal boron-nitride sheet interfaces revealed by ab initio sum-frequency generation spectroscopy. *Phys. Chem. Chem. Phys.* **20**, 12979-12985 (2018).

256. Y.-H. Lu *et al.*, Ultrathin Free-Standing Oxide Membranes for Electron and Photon Spectroscopy Studies of Solid–Gas and Solid–Liquid Interfaces. *Nano Lett.* **20**, 6364-6371 (2020).

257. K. Ojha, K. Doblhoff-Dier, M. T. M. Koper, Double-layer structure of the Pt(111)–aqueous electrolyte interfaces. *Proc. Natl. Acad. Sci. U.S.A.* **119**, e2116016119 (2022).

258. M. Z. Bazant, B. D. Storey, A. A. Kornyshev, Double Layer in Ionic Liquids: Overscreening versus Crowding. *Phys. Rev. Lett.* **106**, 046102 (2011).

259. A. Baskin, D. Prendergast, Exploring chemical speciation at electrified interfaces using detailed continuum models. *J. Chem. Phys.* **150**, 041725 (2019).

260. J. Schneider *et al.*, Understanding TiO2 Photocatalysis: Mechanisms and Materials. *Chem Rev* **114**, 9919-9986 (2014).

261. W. Yuan *et al.*, Visualizing H2O molecules reacting at TiO2 active sites with transmission electron microscopy. *Science* **367**, 428-430 (2020).

262. J. Balajka *et al.*, High-affinity adsorption leads to molecularly ordered interfaces on TiO2 in air and solution. *Science* **361**, 786-789 (2018).

263. M. F. Calegari Andrade, H.-Y. Ko, R. Car, A. Selloni, Structure, Polarization, and Sum Frequency Generation Spectrum of Interfacial Water on Anatase TiO2. *The Journal of Physical Chemistry Letters* **9**, 6716-6721 (2018).

264. S. J. Schlegel *et al.*, How water flips at charged titanium dioxide: an SFG-study on the water–TiO2 interfaces. *Physical Chemistry Chemical Physics* **21**, 8956-8964 (2019).

265. F. Orlando *et al.*, Disordered Adsorbed Water Layers on TiO2 Nanoparticles under Subsaturated Humidity Conditions at 235 K. *The journal of physical chemistry letters* **10**, 7433-7438 (2019).

266. D. O'Carroll, N. J. English, Self-ordering water molecules at TiO2 interfaces: Advances in structural classification. *The Journal of Chemical Physics* **153**, 064502 (2020).

267. D. K. Bora *et al.*, An ultra-high vacuum electrochemical flow cell for in situ/operando soft X-ray spectroscopy study. *Rev Sci Instrum* **85**, 043106 (2014).

268. L. Xi *et al.*, Ionic Current Mn K-Edge X-ray Absorption Spectra Obtained in a Flow Cell. *The Journal of Physical Chemistry C* **122**, 15588-15594 (2018).

269. J. Ren *et al.*, Uncovering the Charge Transfer between Carbon Dots and Water by In Situ Soft X-ray Absorption Spectroscopy. *The Journal of Physical Chemistry Letters* **10**, 3843-3848 (2019).

270. G. Van der Laan, I. Kirkman, The 2p absorption spectra of 3d transition metal compounds in tetrahedral and octahedral symmetry. *Journal of Physics: Condensed Matter* **4**, 4189 (1992).

271. R. Ruus *et al.*, Ti 2p and O 1s X-ray absorption of TiO2 polymorphs. *Solid State Commun* **104**, 199-203 (1997).

272. G. Fronzoni, R. De Francesco, M. Stener, M. Causà, X-ray Absorption Spectroscopy of Titanium Oxide by Time Dependent Density Functional Calculations. *The Journal of Physical Chemistry B* **110**, 9899-9907 (2006).

273. J. Crocombette, F. Jollet, Ti 2p X-ray absorption in titanium dioxides (TiO2): the influence of the cation site environment. *Journal of Physics: Condensed Matter* **6**, 10811 (1994).

274. B. L. Henke, E. M. Gullikson, J. C. Davis, X-Ray Interactions: Photoabsorption, Scattering, Transmission, and Reflection at E = 50-30,000 eV, Z = 1-92. *Atomic Data and Nuclear Data Tables* **54**, 181-342 (1993).

275. I. Plante, A Monte–Carlo step-by-step simulation code of the non-homogeneous chemistry of the radiolysis of water and aqueous solutions. Part I: theoretical framework and implementation. *Radiation and environmental biophysics* **50**, 389-403 (2011).

276. B. H. Frazer, B. Gilbert, B. R. Sonderegger, G. De Stasio, The probing depth of total electron yield in the sub-keV range: TEY-XAS and X-PEEM. *Surf Sci* **537**, 161-167 (2003).

277. J. Meesungnoen, J.-P. Jay-Gerin, A. Filali-Mouhim, S. Mankhetkorn, Low-energy electron penetration range in liquid water. *Radiation research* **158**, 657-660 (2002).

278. K. R. Wilson *et al.*, X-ray Spectroscopy of Liquid Water Microjets. *The Journal of Physical Chemistry B* **105**, 3346-3349 (2001).

279. K. R. Wilson, J. G. Tobin, A. L. Ankudinov, J. J. Rehr, R. J. Saykally, Extended X-Ray Absorption Fine Structure from Hydrogen Atoms in Water. *Phys Rev Lett* **85**, 4289-4292 (2000).

280. Y. Tamenori, Electron yield soft X-ray photoabsorption spectroscopy under normal ambient-pressure conditions. *J Synchrotron Radiat* **20**, 419-425 (2013).

281. G. Ketteler *et al.*, In situ photoelectron spectroscopy study of water adsorption on model biomaterial surfaces. *J Phys-Condens Mat* **20** (2008).

282. V. Lusvardi *et al.*, An NEXAFS investigation of the reduction and reoxidation of TiO2 (001). *Surf Sci* **397**, 237-250 (1998).

283. D. W. Fischer, X-Ray Band Spectra and Molecular-Orbital Structure of Rutile TiO2. *Phys Rev B* **5**, 4219-4226 (1972).

284. A. Nilsson *et al.*, X-ray absorption spectroscopy and X-ray Raman scattering of water and ice; an experimental view. *J Electron Spectrosc* **177**, 99-129 (2010).

285. H. Bluhm, D. F. Ogletree, C. S. Fadley, Z. Hussain, M. Salmeron, The premelting of ice studied with photoelectron spectroscopy. *Journal of Physics: Condensed Matter* **14**, L227 (2002).

286. J. Qian, E. Crumlin (2021) Digital Twin: A Theorist's Playground for APXPS and Surface Science. in *APS March Meeting Abstracts*, p P61. 004.

287. R. S. Wise (2021) Breaking stochastic tradeoffs with a dry deposited and dry developed EUV photoresist system. in *Advances in Patterning Materials and Processes XXXVIII* (International Society for Optics and Photonics), p 1161203.

288. X. Zhao, C. H. W. Wu, H. A. Bechtel, T. Weidman, M. B. Salmeron, Infrared nanospectroscopy characterization of metal oxide photoresists. *Journal of Micro/Nanopatterning, Materials, and Metrology* **21**, 041408 (2022).

289. T. G. Oyama, A. Oshima, S. Tagawa, Estimation of resist sensitivity for extreme ultraviolet lithography using an electron beam. *AIP Advances* **6**, 085210 (2016).

290. N. Thakur, L.-T. Tseng, M. Vockenhuber, Y. Ekinci, S. Castellanos, Stability studies on a sensitive EUV photoresist based on zinc metal oxoclusters. *Journal of Micro/Nanolithography, MEMS, and MOEMS* **18**, 043504 (2019).

291. D. E. Gray, American institute of physics (aip). handbook. *American Institute of Physics handbook* (1963).

292. Q. Luo, C. Hou, Y. Bai, R. Wang, J. Liu, Protein assembly: versatile approaches to construct highly ordered nanostructures. *Chemical reviews* **116**, 13571-13632 (2016).

293. Y. Bai, Q. Luo, J. Liu, Protein self-assembly via supramolecular strategies. *Chemical Society Reviews* **45**, 2756-2767 (2016).

294. J. J. McManus, P. Charbonneau, E. Zaccarelli, N. Asherie, The physics of protein self-assembly. *Current opinion in colloid & interfaces science* **22**, 73-79 (2016).

295. X. Y. Wang *et al.*, AS-Layer Protein of Bacillus anthracis as a Building Block for Functional Protein Arrays by In Vitro Self-Assembly. *Small* **11**, 5826-5832 (2015).

296. U. B. Sleytr, B. Schuster, E.-M. Egelseer, D. Pum, S-layers: principles and applications. *FEMS Microbiology Reviews* **38**, 823-864 (2014).

297. B. Schuster, U. B. Sleytr, Biomimetic interfaces based on S-layer proteins, lipid membranes and functional biomolecules. *J R Soc Interfaces* **11**, 20140232 (2014).

298. R. P. Fagan, N. F. Fairweather, Biogenesis and functions of bacterial S-layers. *Nature Reviews Microbiology* **12**, 211-222 (2014).

299. U. B. Sleytr, P. Messner, D. Pum, M. Sara, *Crystalline bacterial cell surface proteins* (Elsevier, 1996).

300. J. Herrmann *et al.*, A bacterial surface layer protein exploits multistep crystallization for rapid self-assembly. *Proceedings of the National Academy of Sciences* **117**, 388-394 (2020).

301. S.-H. Shin *et al.*, Direct observation of kinetic traps associated with structural transformations leading to multiple pathways of S-layer assembly. *Proceedings of the National Academy of Sciences* **109**, 12968-12973 (2012).

302. E. Baranova *et al.*, SbsB structure and lattice reconstruction unveil Ca 2+ triggered S-layer assembly. *Nature* **487**, 119 (2012).

303. S. Chung, S.-H. Shin, C. R. Bertozzi, J. J. De Yoreo, Self-catalyzed growth of S layers via an amorphous-to-crystalline transition limited by folding kinetics. *Proceedings of the National Academy of Sciences* **107**, 16536 (2010).

304. A. M. Vrabioiu, T. J. Mitchison, Structural insights into yeast septin organization from polarized fluorescence microscopy. *Nature* **443**, 466-469 (2006).

305. G. Obal *et al.*, Conformational plasticity of a native retroviral capsid revealed by x-ray crystallography. *Science* **349**, 95-98 (2015).

306. N. Ilk, E. M. Egelseer, U. B. Sleytr, S-layer fusion proteins--construction principles and applications. *Curr Opin Biotechnol* **22**, 824-831 (2011).

307. M. Sara, U. B. Sleytr, S-Layer proteins. *J Bacteriol* **182**, 859-868 (2000).

308. B. Rad *et al.*, Ion-specific control of the self-assembly dynamics of a nanostructured protein lattice. *Acs Nano* **9**, 180-190 (2015).

309. A. Breitwieser, P. Siedlaczek, H. Lichtenegger, U. B. Sleytr, D. Pum, S-Layer Protein Coated Carbon Nanotubes. *Coatings* **9**, 492 (2019).

310. M. Charrier *et al.*, Engineering the S-layer of Caulobacter crescentus as a foundation for stable, high-density, 2D living materials. *ACS synthetic biology* **8**, 181-190 (2018).

311. B. Stel, F. Cometto, B. Rad, J. J. De Yoreo, M. Lingenfelder, Dynamically resolved self-assembly of S-layer proteins on solid surfaces. *Chem Commun (Camb)* **54**, 10264-10267 (2018).

312. B. Stel *et al.*, Contrasting chemistry of block copolymer films controls the dynamics of protein self-assembly at the nanoscale. *Acs Nano* **13**, 4018-4027 (2019).

313. P. Mobili *et al.*, Characterization of S-layer proteins of Lactobacillus by FTIR spectroscopy and differential scanning calorimetry. *Vibrational Spectroscopy* **50**, 68-77 (2009).

314. A. Barth, Infrared spectroscopy of proteins. *Biochimica et Biophysica Acta (BBA)-Bioenergetics* **1767**, 1073-1101 (2007).

315. D. Paschek *et al.*, The Solvent-Dependent Shift of the Amide I Band of a Fully Solvated Peptide as a Local Probe for the Solvent Composition in the Peptide/Solvent Interfaces. *Chemphyschem* **9**, 2742-2750 (2008).

316. E. A. Muller, B. Pollard, H. A. Bechtel, P. van Blerkom, M. B. Raschke, Infrared vibrational nanocrystallography and nanoimaging. *Science advances* **2**, e1601006 (2016).

317. I. Amenabar *et al.*, Structural analysis and mapping of individual protein complexes by infrared nanospectroscopy. *Nat Commun* **4**, 2890 (2013).

318. G. Bakir *et al.*, Orientation matters: Polarization dependent IR spectroscopy of collagen from intact tendon down to the single fibril level. *Molecules* **25**, 4295 (2020).

319. S. W. Englander, L. Mayne, Z.-Y. Kan, W. Hu, Protein folding—how and why: by hydrogen exchange, fragment separation, and mass spectrometry. *Annual review of biophysics* **45**, 135-152 (2016).

320. M. Guttman *et al.*, Antibody potency relates to the ability to recognize the closed, pre-fusion form of HIV Env. *Nat Commun* **6**, 1-11 (2015).

321. J. G. Mandell, A. Baerga-Ortiz, A. M. Falick, E. A. Komives, "Measurement of solvent accessibility at protein-protein interfaces" in Protein-Ligand Interactions. (Springer, 2005), pp. 65-79.

322. S. Krimm, J. Bandekar, Vibrational spectroscopy and conformation of peptides, polypeptides, and proteins. *Advances in protein chemistry* **38**, 181-364 (1986).

323. K. A. Oberg, J. M. Ruysschaert, E. Goormaghtigh, The optimization of protein secondary structure determination with infrared and circular dichroism spectra. *European journal of biochemistry* **271**, 2937-2948 (2004).

324. K. J. Kaltenecker, T. Gölz, E. Bau, F. Keilmann, Infrared-spectroscopic, dynamic near-field microscopy of living cells and nanoparticles in water. *Sci Rep-Uk* **11**, 1-12 (2021).

325. M. J. Elowson *et al.*, Fabrication of ultrathin suspended membranes from atomic layer deposition films. *Journal of Vacuum Science & Technology B, Nanotechnology and Microelectronics: Materials, Processing, Measurement, and Phenomena* **40**, 023001 (2022).

326. D. Roccella, M. Amati, H. Sezen, R. Brescia, L. Gregoratti, Size contrast of Pt nanoparticles formed on neighboring domains within suspended and supported graphene. *Nano Research* **11**, 1589-1598 (2018).

327. C.-T. Hsieh, W.-Y. Chen, D.-Y. Tzou, A. K. Roy, H.-T. Hsiao, Atomic layer deposition of Pt nanocatalysts on graphene oxide nanosheets for electro-oxidation of formic acid. *International journal of hydrogen energy* **37**, 17837-17843 (2012).

328. H. Knoops *et al.*, Remote plasma ALD of platinum and platinum oxide films. *Electrochemical and Solid State Letters* **12**, G34 (2009).

329. T. Aaltonen, M. Ritala, T. Sajavaara, J. Keinonen, M. Leskelä, Atomic layer deposition of platinum thin films. *Chemistry of materials* **15**, 1924-1928 (2003).

330. Q. Zhu, C. J. Murphy, L. R. Baker, Opportunities for Electrocatalytic CO₂ Reduction Enabled by Surface Ligands. *J Am Chem Soc* **144**, 2829-2840 (2022).

331. S. Yu, S. Louisia, P. Yang, The Interactive Dynamics of Nanocatalyst Structure and Microenvironment during Electrochemical CO2 Conversion. *JACS Au* 10.1021/jacsau.1c00562 (2022).

332. S. Yu *et al.*, Nanoparticle Assembly Induced Ligand Interactions for Enhanced Electrocatalytic CO2 Conversion. *J Am Chem Soc* **143**, 19919-19927 (2021).

333. Y. Li *et al.*, Electrochemically scrambled nanocrystals are catalytically active for CO2-to-multicarbons. *Proceedings of the National Academy of Sciences* **117**, 9194-9201 (2020).

334. D. Kim *et al.*, Selective CO2 electrocatalysis at the pseudocapacitive nanoparticle/ordered-ligand interlayer. *Nature Energy* **5**, 1032-1042 (2020).

335. C. Chen *et al.*, Cu-Ag Tandem Catalysts for High-Rate CO2 Electrolysis toward Multicarbons. *Joule* **4**, 1688-1699 (2020).

336. Y. Zheng *et al.*, Understanding the Roadmap for Electrochemical Reduction of CO₂ to Multi-Carbon Oxygenates and Hydrocarbons on Copper-Based Catalysts. *J Am Chem Soc* **141**, 7646-7659 (2019).

337. A. A. Ahmed, S. Gypser, P. Leinweber, D. Freese, O. Kühn, Infrared spectroscopic characterization of phosphate binding at the goethite–water interfaces. *Phys Chem Chem Phys* **21**, 4421-4434 (2019).

338. A. Cernescu *et al.*, Label-Free Infrared Spectroscopy and Imaging of Single Phospholipid Bilayers with Nanoscale Resolution. *Analytical Chemistry* **90**, 10179-10186 (2018).

339. J. M. Arias, M. E. Tuttolomondo, S. B. Díaz, A. Ben Altabef, Reorganization of Hydration Water of DPPC Multilamellar Vesicles Induced by l-Cysteine Interaction. *The Journal of Physical Chemistry B* **122**, 5193-5204 (2018).

340. D. Kim, C. S. Kley, Y. Li, P. Yang, Copper nanoparticle ensembles for selective electroreduction of CO2 to C2–C3 products. *Proceedings of the National Academy of Sciences* **114**, 10560-10565 (2017).

341. J. M. Yoo, H. Shin, S. Park, Y.-E. Sung, Recent progress in in situ/operando analysis tools for oxygen electrocatalysis. *Journal of Physics D: Applied Physics* **54**, 173001 (2021).

342. Y. Uematsu, Electrification of water interfaces. *Journal of Physics: Condensed Matter* **33**, 423001 (2021).

343. Y. R. Shen, V. Ostroverkhov, Sum-Frequency Vibrational Spectroscopy on Water Interfaces: Polar Orientation of Water Molecules at Interfaces. *Chem Rev* **106**, 1140-1154 (2006).

344. I. Brand, *Application of polarization modulation infrared reflection absorption spectroscopy in electrochemistry* (Springer Nature, 2020).

345. C. S. Kumar, *Surface Science Tools for Nanomaterials Characterization* (Springer, 2015).

346. H. Wiedemann, "Synchrotron radiation" in Particle Accelerator Physics. (Springer, 2003), pp. 647-686.

347. A. J. Bard, L. R. Faulkner, J. Leddy, C. G. Zoski, *Electrochemical methods: fundamentals and applications* (wiley New York, 1980), vol. 2.

348. E. Strelcov *et al.*, Nanoscale Mapping of the Double Layer Potential at the Graphene–Electrolyte Interfaces. *Nano Lett* **20**, 1336-1344 (2020).

349. N. Kobayashi, H. Asakawa, T. Fukuma, Nanoscale potential measurements in liquid by frequency modulation atomic force microscopy. *Rev Sci Instrum* **81**, 123705 (2010).

350. Z. Wang *et al.*, Structural regulation chemistry of lithium ion solvation for lithium batteries. *EcoMat* **4** (2022).

351. E. A. Cave, J. Z. Olson, C. W. Schlenker, Ion-Pairing Dynamics Revealed by Kinetically Resolved In Situ FTIR Spectroelectrochemistry during Lithium-Ion Storage. *ACS Applied Materials & Interfaces* **13**, 48546-48554 (2021).

352. D. M. Seo *et al.*, Role of Mixed Solvation and Ion Pairing in the Solution Structure of Lithium Ion Battery Electrolytes. *The Journal of Physical Chemistry C* **119**, 14038-14046 (2015).

353. Y. Marcus, G. Hefter, Ion Pairing. *Chem Rev* **106**, 4585-4621 (2006).

354. J. A. Mondal, S. Nihonyanagi, S. Yamaguchi, T. Tahara, Structure and Orientation of Water at Charged Lipid Monolayer/Water Interfaces Probed by Heterodyne-Detected Vibrational Sum Frequency Generation Spectroscopy. *J Am Chem Soc* **132**, 10656-10657 (2010).

355. X. Chen, W. Hua, Z. Huang, H. C. Allen, Interfacial Water Structure Associated with Phospholipid Membranes Studied by Phase-Sensitive Vibrational Sum Frequency Generation Spectroscopy. *J Am Chem Soc* **132**, 11336-11342 (2010).

Bibliography

Mr. Xiao Zhao received his B.S. degree in Chemical Physics (Special Class for the Gifted Young) from University of Science and Technology of China (USTC) and is currently a Ph.D. candidate under the supervision of Prof. Miquel Salmeron in the Department of Materials Science and Engineering at University of California, Berkeley, and Lawrence Berkeley National Laboratory. His research focuses on operando investigation of the electrical double layer and soft material at interfaces.

Appendix-graphene transfer

Space, tools and short introduction

Graphene transfer is a dedicated process, which is very sensitive to the environment, operation or even the history of tools. For example, it seems that the transfer is bad when the PM2.5 or PM10 is high during wildfire season (air quality), or even when there is heavy rain outside (humidity). Even the same person transferring graphene twice in one week can observe quite different results.

Our criterion of "good transfer" are: 1. The coverage is high (>95%, which means <11 open holes/cracks for 15X15 membrane, or even >98%) 2. Not many nor tall wrinkles 3. Not much dust 4. Graphene can survive some bias before intercalation or break. Molecular Foundry 1201 is an ideal place for graphene transfer, as the picture below shows most tools needed for transfer. It would be best to keep these tools for graphene transfer only, or at least cleaned by IPA/methanol and dried in N_2.

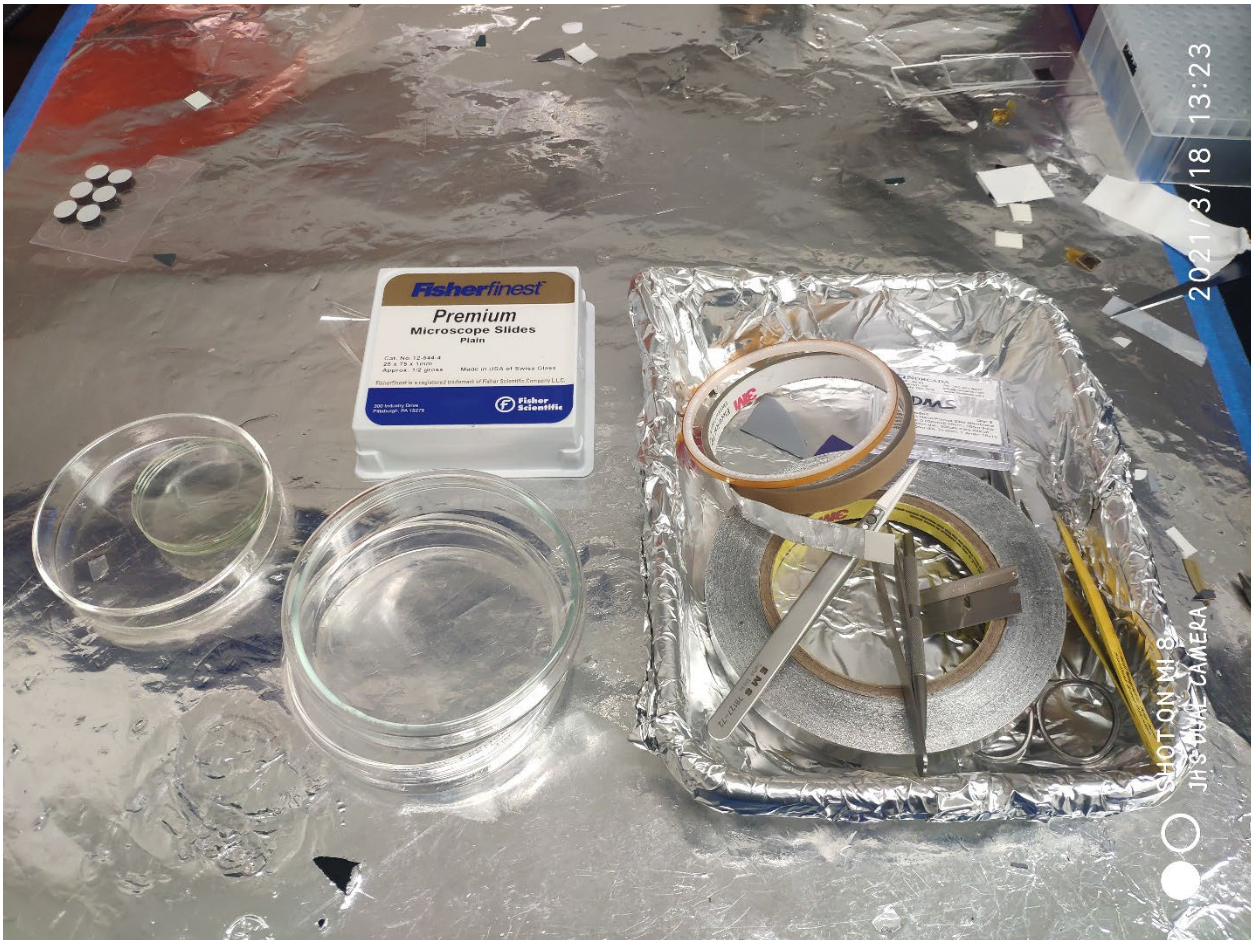

Tools for graphene transfer: dishes, glass slides, Kapton tape, aluminum foil tape, at least two tweezers, scissors, blade, PDMS box, Si wafer pieces

This manual is for polymer-free graphene transfer. According to our experience, although polymer assisted transfer could increase the coverage (even up to 100%), it also brings severe polymer contamination, especially in the suspended region, which contaminate the tip and interfere with our nano-FTIR and KPFM experiments. In certain cases, such as for XPS, the main goal is to achieve high coverage, polymer assisted transfer could be used.

General timeline for transfer:

Day0: evaporate 2nm Cr, then 25nm Au on the front side of holy SiN membrane

Day1: transfer graphene onto SiN membrane and let it dry in N2 overnight

Day2: check coverage

Day3: anneal this membrane to 250-300C in vacuum for at least 6 hours (usually overnight)

Day4: these samples are ready for use, or do SEM/XPS/Raman tests

Make etching solution

The etching solution is ~0.2M $Na_2S_2O_8$ solution. $Na_2S_2O_8$ is not very stable in aqueous solution, so it is necessary always make fresh solution every time before transfer. $Na_2S_2O_8$ solution is acid and oxidative, and trace amount of organic residue on dish will react with $Na_2S_2O_8$ and quench the etching reaction. The dishes for graphene transfer should be free of any organic molecules and be used for graphene transfer only. [Important]

For the dishes shown below, the volume is roughly 90 ml, so **3.8g** $Na_2S_2O_8$ is usually used to make the solution. (**4.2g** has also been tried and the etching time will be reduced from ~2h to ~1h40min, and the graphene quality are fine. Sometimes if the dishes haven't been used for some time, there might be some contamination and 4.2g is suggested)

1. Clean the dish and the lid three time using MilliQ water [Important]

2. Fill the dish with MilliQ water until it is full

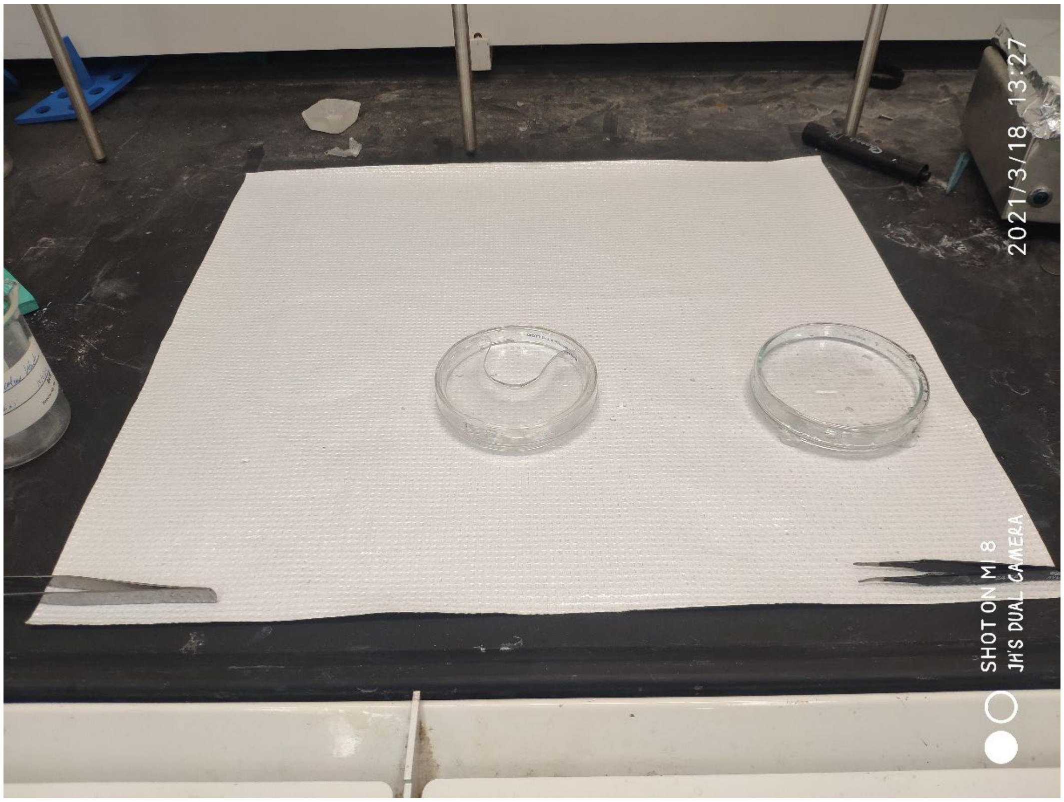

3. Close the lid and remove extra water (The top surface of water should not touch the dish lid, but should be as high as possible[suggested])

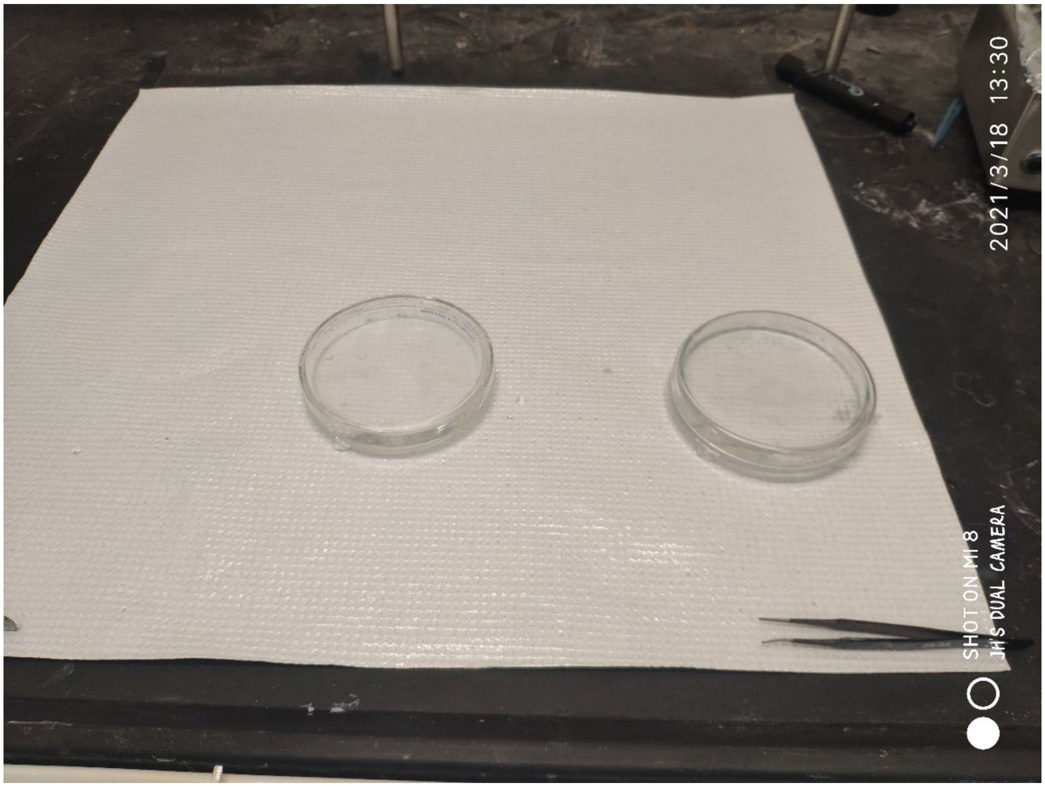

4. Weight 3.8g(4.2g) $Na_2S_2O_8$ salt on a weighting boat and pour it into the dish, no stir needed

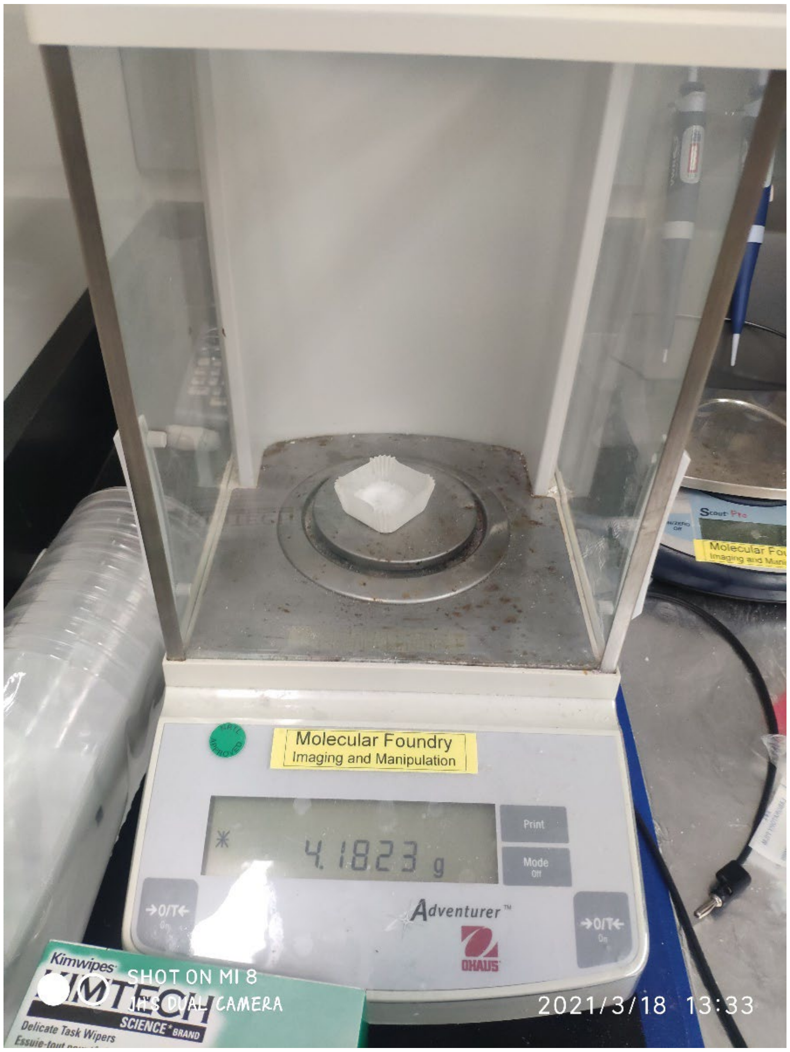

Clean graphene

The CVD graphene on Cu foil is actually grown on both sides. The quality is better on the front side than the back side. The purpose of this step is to remove back side graphene. Otherwise, the etching time will be longer, and the back-side graphene flakes might stick on the suspended graphene.

1. Cut a piece of graphene off from CVD graphene and put it up-side down on a glass slide

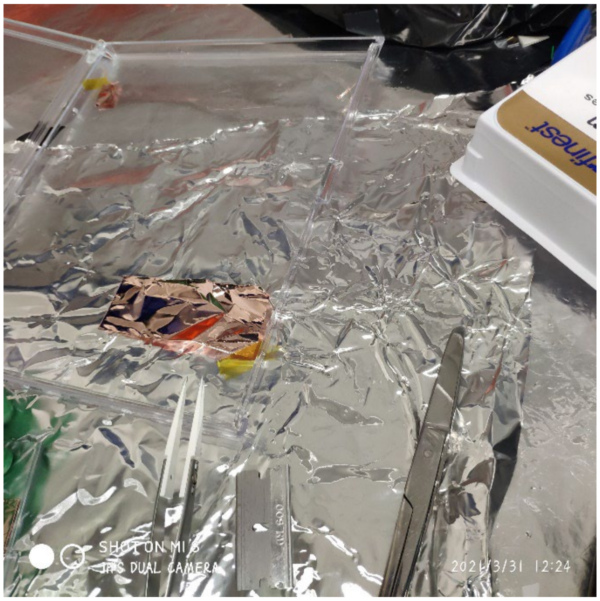

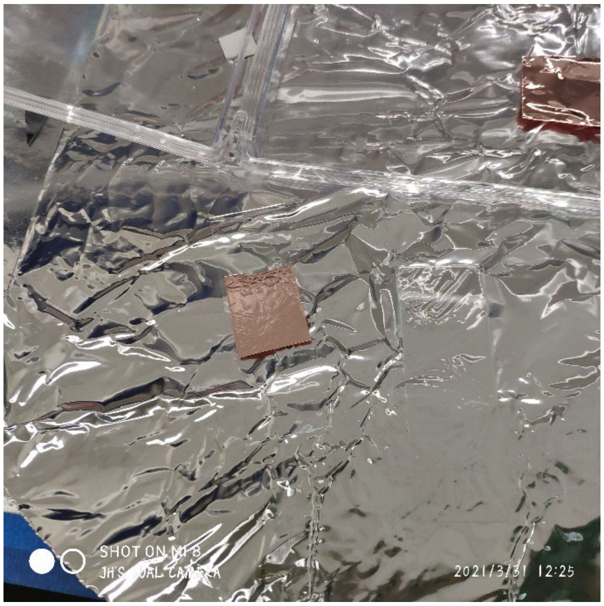

2. Use Kapton tape to seal the edge of graphene, put another slide on top and apply some pressure to make it as flat as possible

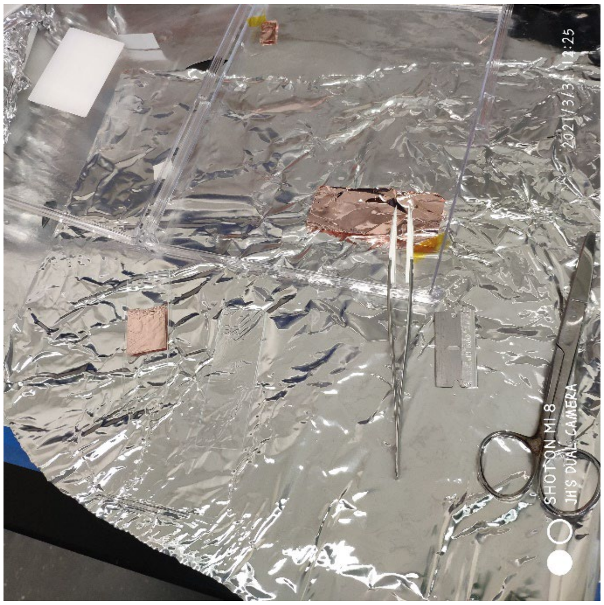

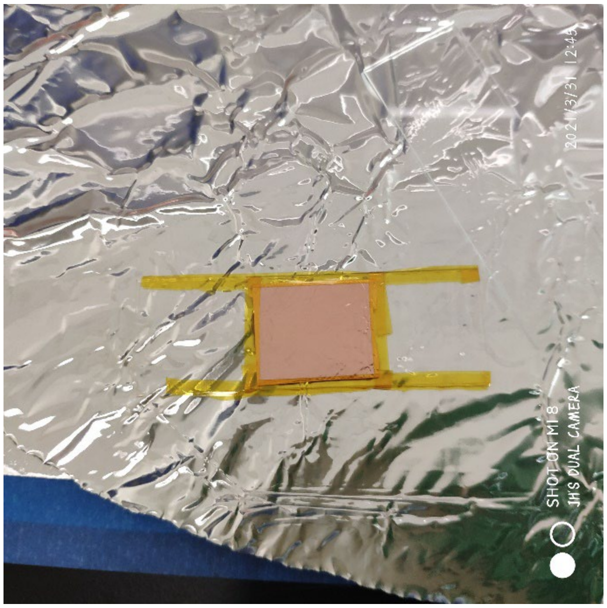

3. O2 plasma:
    a. Gas: 25% Oxygen, 75%Argon, plasma should be purple
    b. Time: 8min

    c. Pressure: ~200-400mTorr

4. Take the graphene out from plasma (make sure the tweezer is clean, free of contamination)

Make mask

Why do we need a mask? The most obvious reason is that we need to locate the graphene. Good quality sing-layer graphene is totally transparent, so once the Cu under graphene is etched away, there is nothing visible left on surface. An Al mask help to indicate the position of graphene. There might be some other benefits: the mask helps the single layer graphene to expand on solution-air interfaces, otherwise the graphene might shrink into a particle.

1. Cut the graphene after Oxygen plasma into small pieces (~2cm by 2cm) and place them between 2 glass slides, apply some pressure to make it flat (ALWAYS KEEP IN MIND WHICH SIDE IS THE FRONT SIDE[IMPRONT])

2. Use blade to make a mask and stick it onto the front side of graphene

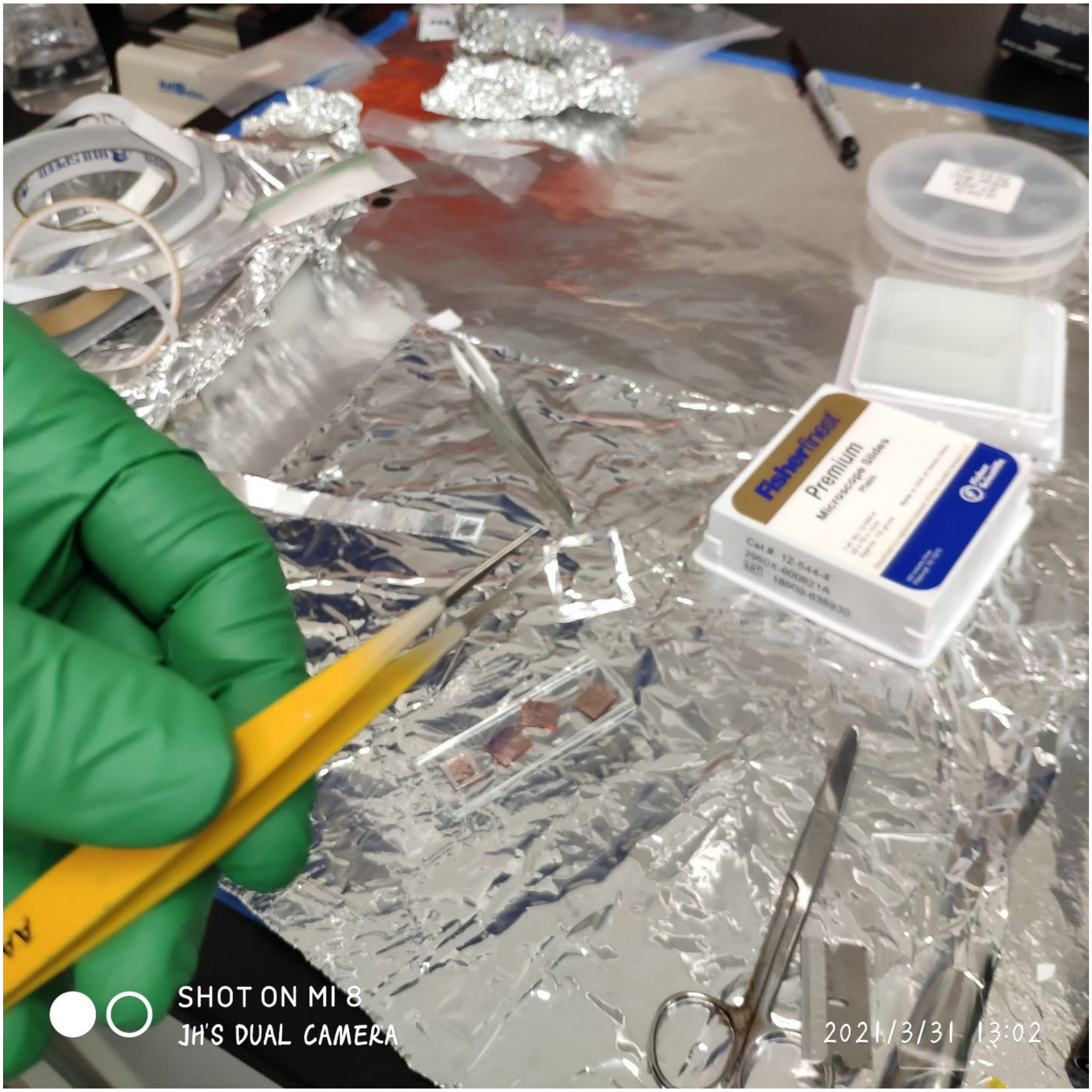

3. Place them between 2 glass slides, apply some pressure to make it flat [suggested]

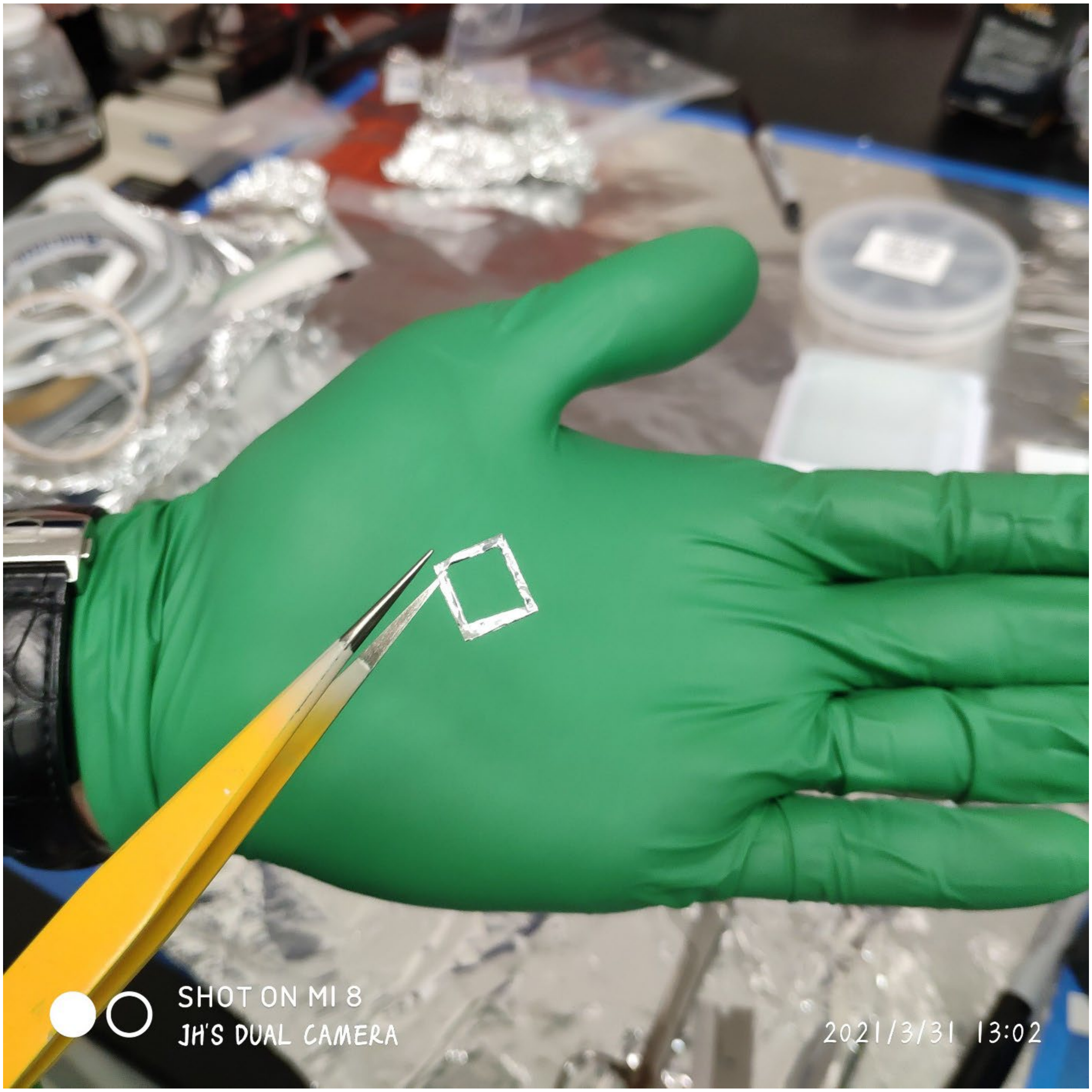

4. Put these films in the etching solution with ceramic tweezer

Etching

Typically for 3.8g salt the etching time is around 2 hours, at ~1h20min, Cu film begin depleted at some point, and at ~1h40min, Cu film is etched away completely, and the solution becomes blue ($CuSO_4$ solution). In practical, the graphene film will be kept in the etching solution for 20 more mins after Cu completely dissolved.

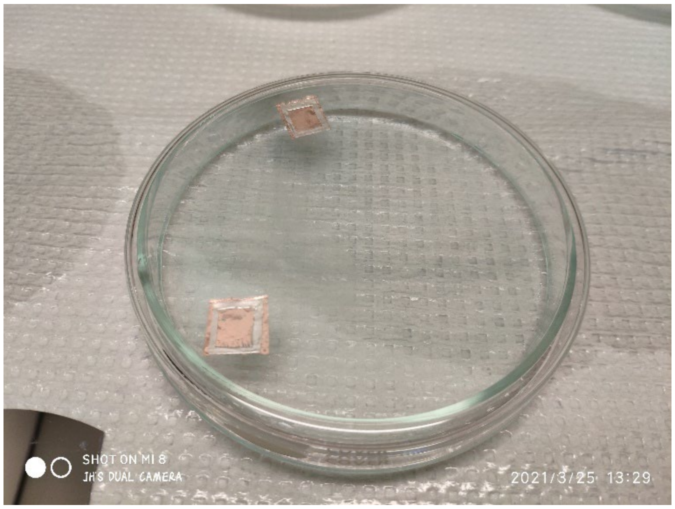

Wash suspended graphene

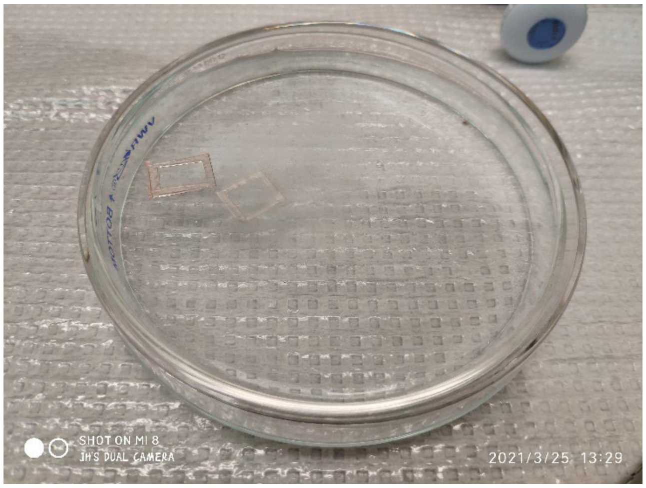

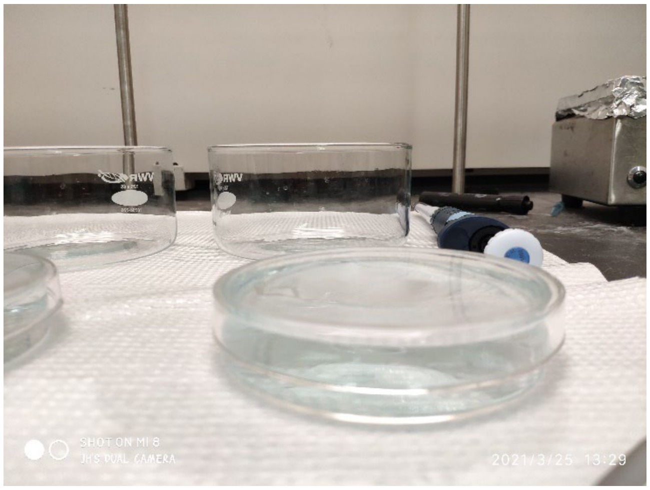

This is the most difficult step in the graphene transfer process.

1. Wash and fill some large dishes with MilliQ water, the water should be as much as possible

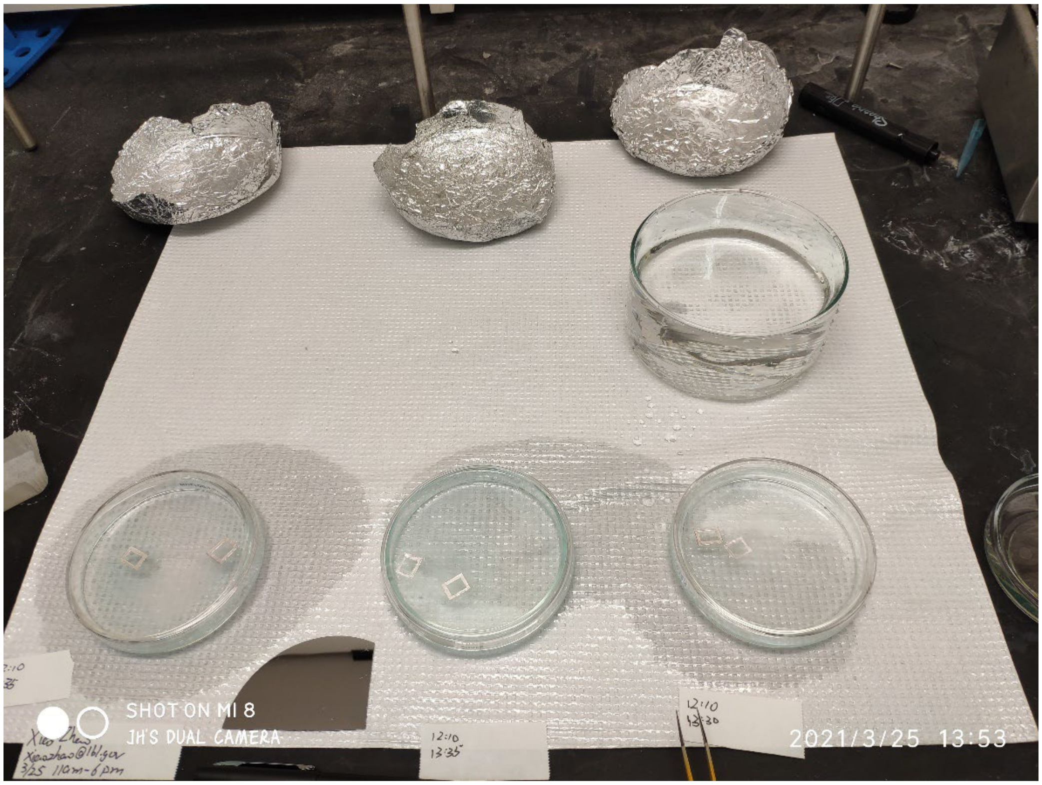

2. Treat the round glass slides with air plasma
    a. Gas: air, plasma should be orange
    b. Time: 1-3min
    c. Pressure: ~200-400mTorr
3. Use the round glass slides to transfer the graphene film to large dish and wait for 1-1.5h, in the first dish, the glass should be as flat as you can to make sure that the graphene will not move when taken out; in the second dish it would be better to have glass inclined for some degrees, to let water fill the gap between graphene and glass.

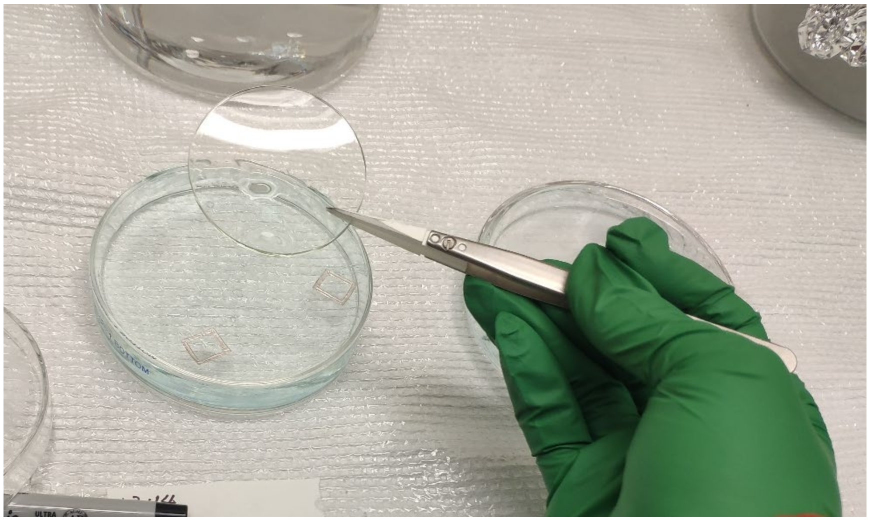

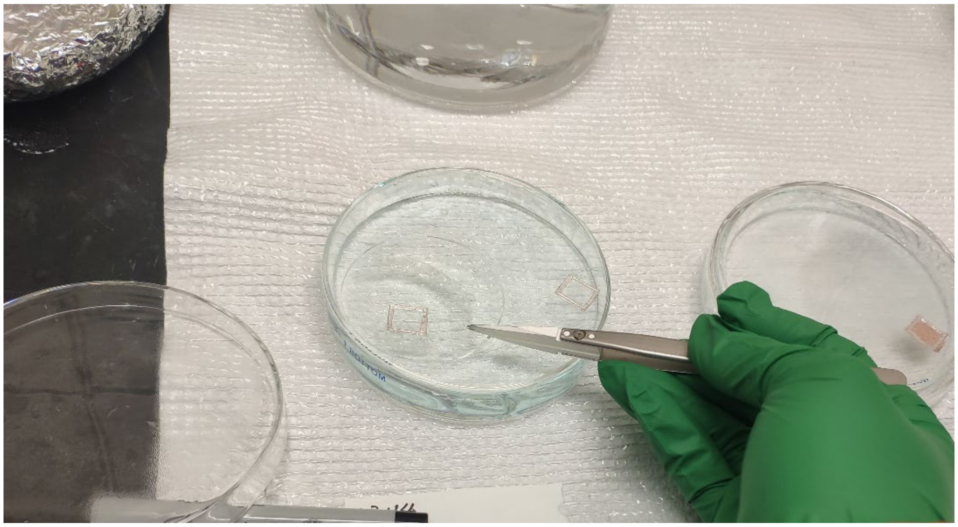

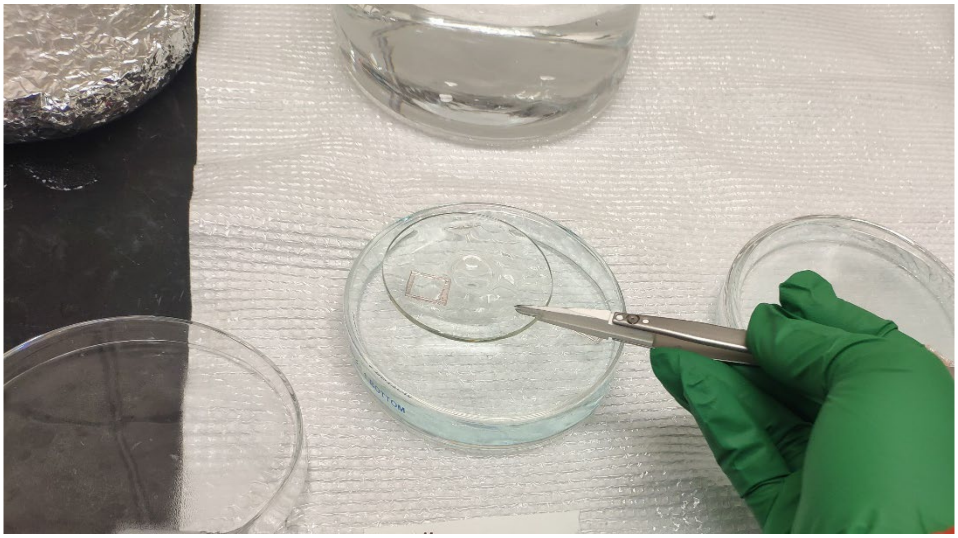

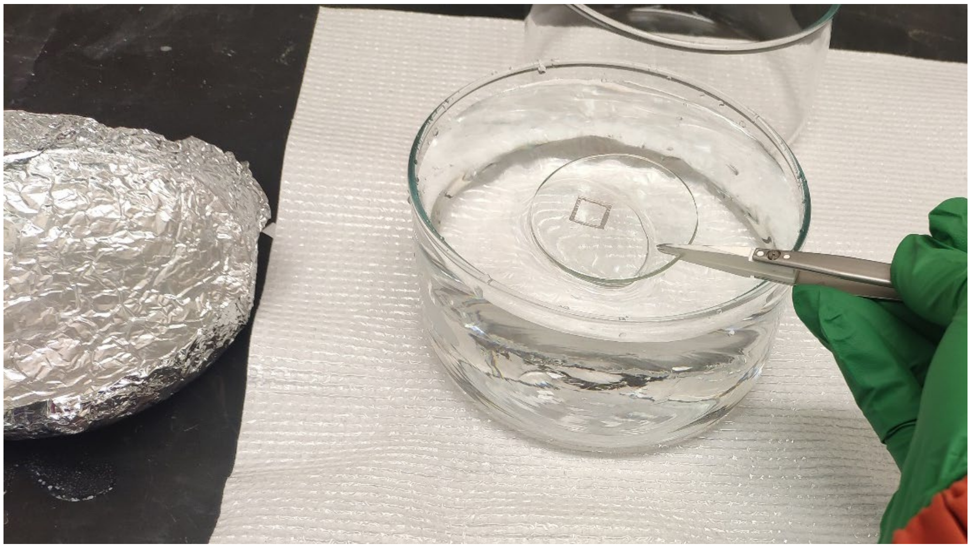

4. Repeat the above process once more and wait for at least 30 min

Transfer and dry

1. Cut some pieces of PDMS and stick them on one side of Si wafer pieces (the Si wafer should be rectangular and PDMS is at one end of the Si [suggested])
2. Put the SiN membranes carefully on PDMS, make sure they are close enough, use tweezer to push a little bit
3. Treat the SiN membranes with air plasma
    a. Gas: air, plasma should be orange
    b. Time: 1-3min
    c. Pressure: ~200-400mTorr
4. Transfer the graphene on SiN membrane and dry them in N2 box, use a second tweezer or something else to guide the graphene (pushing graphene by placing it near graphene) After taking the SiN membranes out, there will be liquid film remaining between graphene and SiN membrane, and it can lead to lateral movement of graphene relative to SiN membrane. <u>It is important to remove this water by gently touching the back side of Si substrate by Wipe paper to remove water drop.</u> [IMPORTANT]

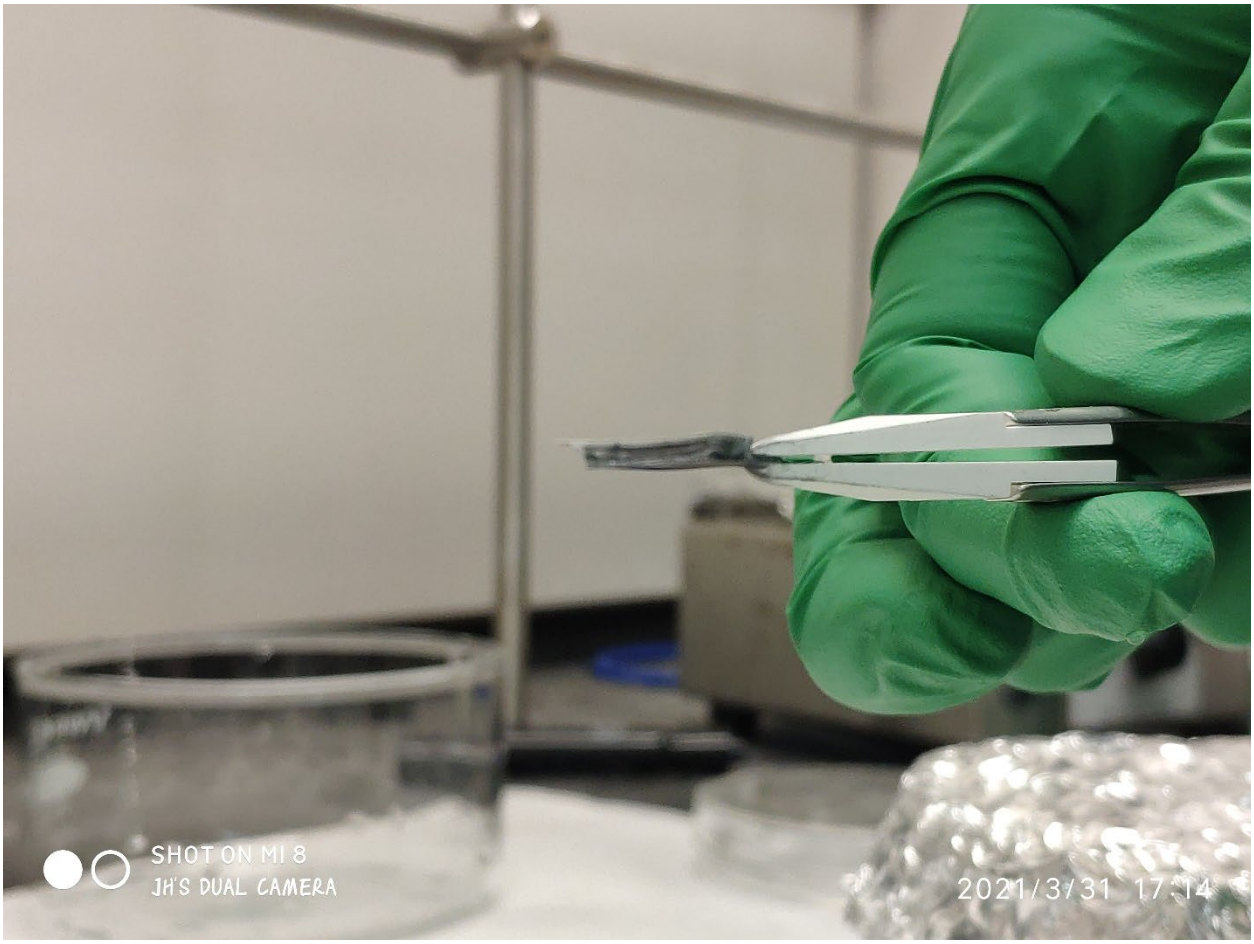
SHOT ON MI 8
JH'S DUAL CAMERA
2021/3/31 17:14

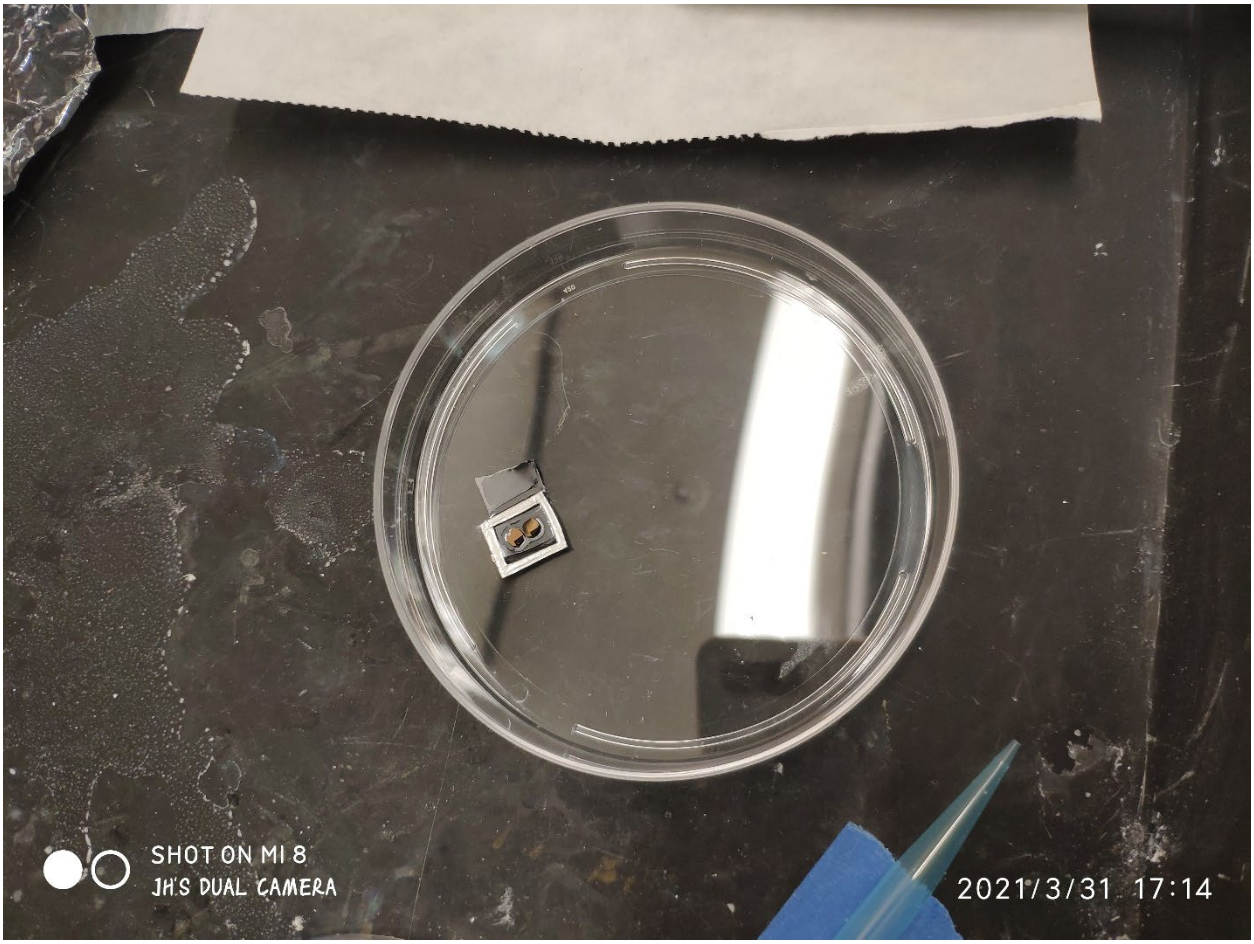
SHOT ON MI 8
JH'S DUAL CAMERA
2021/3/31 17:14

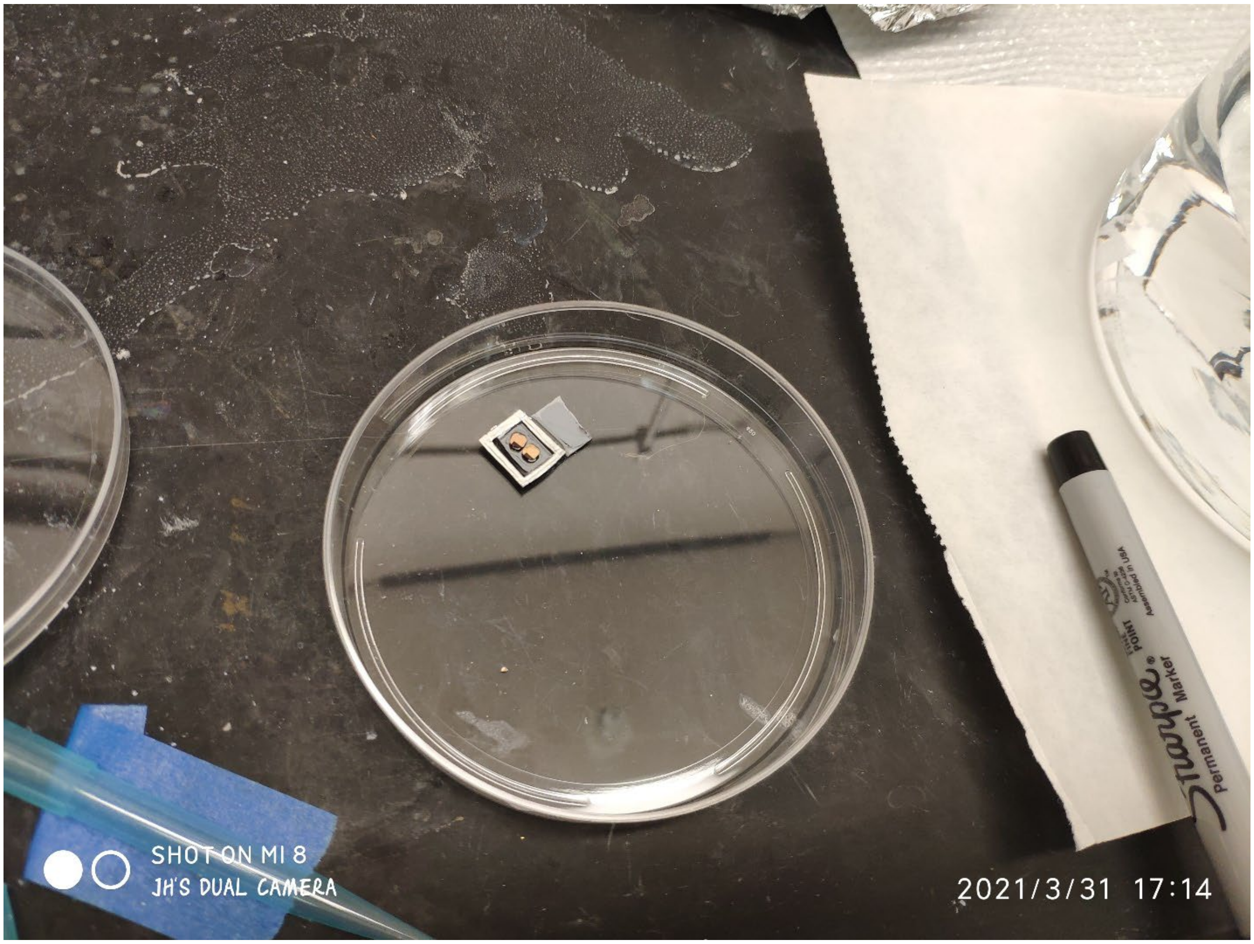

Post transfer treatment

After the SiN membrane died in N2, the coverage is usually checked by Multimode AFM or MFP-3D AFM, and the good samples will be annealed to 250C(300C) in vacuum.

1. The pressure inside the chamber will reach typically 10^-7 mbarr (or at least 10^-6 mbarr) overnight
2. The temperature needs to be increased by 5-10 degC step to ensure it is not heated drastically